

(NASA-TM-X-370) THE EFFECTS OF NOSE
BLUNTNESS ON THE FLOW SEPARATION AND
LONGITUDINAL CHARACTERISTICS OF
ELLIPSOIDAL-NOSED CYLINDER-FLARE MODELS AT
J.W. Cleary (NASA) Aug. 1960 108 p

N72-71308

Unclas
00/99 21340

T.D. 72-136 3-12-72

TECHNICAL MEMORANDUM X-370

THE EFFECTS OF NOSE BLUNTNESS ON THE FLOW SEPARATION
AND LONGITUDINAL CHARACTERISTICS OF ELLIPSOIDAL-
NOSED CYLINDER-FLARE MODELS AT

TRANSONIC SPEEDS

By Joseph W. Cleary

Ames Research Center
Moffett Field, Calif.

FACILITY FORM 602

(ACCESSION NUMBER)

108

(PAGES)

(NASA CR OR TMX OR AD NUMBER)

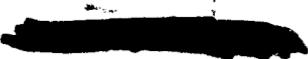
(THRU)

None
(CODE)

(CATEGORY)

NATIONAL AERONAUTICS AND SPACE ADMINISTRATION
WASHINGTON

August 1960


NATIONAL AERONAUTICS AND SPACE ADMINISTRATION

TECHNICAL MEMORANDUM X-370

THE EFFECTS OF NOSE BLUNTNESS ON THE FLOW SEPARATION
AND LONGITUDINAL CHARACTERISTICS OF ELLIPSOIDAL-
NOSED CYLINDER-FLARE MODELS AT



TRANSONIC SPEEDS*

By Joseph W. Cleary

SUMMARY

An investigation in a transonic wind tunnel has been conducted to establish the approximate degree of nose bluntness permissible before transonic flow separation occurred on cylinder-flare models. Three ellipsoidal nose shapes were considered. Flow separation was avoided for angles of attack of this investigation by use of a prolate ellipsoidal nose with a ratio of semimajor-to-semiminor axis of 2. This nose shape not only provided a satisfactory neutral point but another investigation has shown it was dynamically stable at transonic Mach numbers. The tests indicate that on the blunter models the flare contributed a secondary but perhaps an important effect on transonic flow separation.

Pressure-distribution measurements showed the transonic flow separation was associated with high peak negative pressure coefficients at or near the nose-body juncture that promoted adverse pressure gradients for which there would be extreme shear in the boundary layer. At supercritical Mach numbers, the formation of local shocks may have steepened the pressure gradients and thus contributed to the occurrence of flow separation even at 0° angle of attack. Reattachment of the flow at 0° angle of attack at higher Mach numbers was a result of a change from a basically subsonic type of pressure distribution to a supersonic type with more favorable pressure gradients. This change in the type of pressure distribution was predicted by an extension of the Mach number freeze concept that, in general, applied to the experimental pressure distributions for Mach numbers between about 0.90 and 1.10.

INTRODUCTION

A solution to the heating problem of vehicles entering the earth's atmosphere along a ballistic path has been achieved with blunt nose shapes of high pressure drag. While the exact shape of such blunt-nosed vehicles may vary widely depending on the mission of the vehicle and the method of controlling the heating load, a configuration of considerable interest is the flare-stabilized circular cylinder. This interest stems from available data (e.g., refs. 1 and 2) which indicate that the flare-stabilized cylinder has no unusual static or dynamic stability problems throughout the higher supersonic and hypersonic Mach number ranges. Within these Mach number ranges the main problem is one of maintaining an adequate static margin as the static stability slowly decreases with increasing Mach number.

At subsonic and transonic Mach numbers, a peculiar three-dimensional flow-separation phenomenon has been observed for blunt-nosed flare-stabilized cylinders and is discussed in reference 1. This separation phenomenon assumes importance because blunt ballistic vehicles are likely to decelerate to subsonic Mach numbers during descent through the atmosphere. Furthermore, the investigation of reference 1 convincingly demonstrates that the phenomenon has adverse effects on both the static and dynamic stability of this configuration at transonic Mach numbers. The problem is perhaps more forcibly demonstrated by the free-flight results of reference 3 wherein the model performed essentially six-degree-of-freedom gyrations while decelerating to subsonic Mach numbers.

The small radius of curvature of a blunt nose at or near the point where the nose fairs into a cylindrical body induces a local flow region of high velocity. As with two-dimensional flows over curved surfaces, these induced velocities may exceed local sonic velocity and terminate in a shock. Pressure-distribution studies are particularly useful in explaining the salient features of such supercritical flows. For Mach numbers greater than unity, the theoretical nonviscous flow solution of the blunt-body problem of reference 4 may prove useful for those nose shapes for which separation does not occur. It should be noted, however, that reference 4 treats primarily subsonic regions of supersonic flow where the pressure gradient is favorable.

Because of the absence of a suitable viscous compressible flow theory to account for the separation phenomenon even for simple axisymmetric flows, the present experimental tests were undertaken to obtain further details of the separation phenomenon and to extend the results of reference 1 to a wider range of nose shapes. Wind-tunnel force and pressure-distribution tests were made at transonic Mach numbers of cylinder-flare models, with prolate, spherical, and oblate ellipsoidal

noses. Also presented is a limited discussion of the dynamic stability characteristics of cylinder-flare models based on previously published test results.

COEFFICIENTS AND NOTATION

C_{A_b}	base axial-force coefficient, $\frac{\text{base axial force}}{qS}$
C_D	total-drag coefficient, $\frac{\text{total drag}}{qS}$
C_{D_b}	base-drag coefficient, $\frac{\text{base drag}}{qS}$
C_L	lift coefficient, $\frac{\text{lift}}{qS}$
C_m	pitching-moment coefficient, $\frac{\text{pitching moment}}{qSd}$
$C_{m_{q_0}} + C_{m_{\dot{\alpha}}}$	damping-in-pitch coefficient, $\frac{\partial C_m}{\partial (q_0 d/V)} + \frac{\partial C_m}{\partial (\dot{\alpha} d/V)}$, per radian
C_N	normal-force coefficient, $\frac{\text{normal force}}{qS}$
C_p	pressure coefficient, $\frac{p_l - p}{q}$
$C_{p_{cr}}$	critical pressure coefficient
$C_{p_{max}}$	maximum pressure coefficient
d	cylindrical body diameter
d_1	flare base diameter
l	model length
M	free-stream Mach number
p_l	local static pressure
p	free-stream static pressure
q_0	pitching velocity
q	free-stream dynamic pressure
r_s	radius of curvature at stagnation point
R	free-stream Reynolds number based on d

S	body cross-sectional area
V	free-stream velocity
x	distance after nose
α	angle of attack
λ	nose length
λ_1	cylindrical body length
λ_2	flare length
τ	nose thickness ratio, $\frac{d/2}{\lambda}$
θ	peripheral angle of model
ξ, η	Cartesian coordinates of noses
ϕ	flare angle
γ	ratio of specific heats
$\frac{dC_L}{d\alpha}$	lift-curve slope at 0° angle of attack, per deg
$\frac{dC_N}{d\alpha}$	normal-force-curve slope at 0° angle of attack, per deg

MODELS, TESTS, AND PRECISION

The models consisted of smooth Fiberglas bodies of revolution with the nose and flare components shown in figure 1. Dimensional details of the models are presented in figure 2. The three nose shapes were affinely related ellipsoids of fineness ratios 2, 1, and 1/2 and, for purposes of this investigation, have been designated prolate, spherical, and oblate, respectively. Two conical flares were employed and were designated the standard flare and the extended flare as illustrated in figure 2. Tests with the extended flare were of limited scope and were intended to evaluate the characteristics of the prolate-nosed model with a flare of smaller angle but of larger size. The 0° flare was merely an extension of the cylindrical body of the same length as the standard flare. Although minor unavoidable abrasion occurred on the noses of the models during the tests, frequent stops were made to refinish the nose surfaces. The effects of abrasion on the results presented herein are believed unimportant.

Pressure orifices were installed in longitudinal rows at counter-clockwise peripheral angles of 0° , 45° , 90° , 180° , 225° , and 270° as shown in figure 2. The 270° row of orifices was used only to confirm that the model was properly aligned laterally in the wind tunnel. Data of the 225° row have been presented as a reflection in the vertical plane and correspondingly labeled 135° . The longitudinal positions of the orifices are given in table I. Pressures were measured by multiple-tube mercury-in-glass manometers and the data were photographically recorded. Pressure coefficients are believed precise to within ± 0.020 .

The models were mounted on a strain-gage balance and were supported by a 4-inch-diameter sting as shown in figure 3. The sting-support system maintains the model close to the tunnel center line with a negligible horizontal translation as angle of attack increases or decreases. This arrangement was modified to obtain the shadowgraph data; the model was translated to a vertical off-center position to facilitate photographing the model.

The investigation was conducted in the Ames 14-Foot Transonic Wind Tunnel at Mach numbers from 0.40 to 1.18. Details of the nozzle and test section of this facility are shown in figure 4. The tunnel is operated at a constant stagnation pressure, approximately atmospheric, but at variable stagnation temperature. The temperature variations are solely to avoid moisture condensation in the test section.

The Reynolds numbers based on the cylindrical-body diameter were within the shaded region of figure 5 for all models of this investigation. The angle of attack of the model was varied from about -4° to $+20^\circ$. Angle-of-attack precision is within $\pm 0.10^\circ$. Flow angularity and curvature of the flow in the 14-foot tunnel are negligible. The Mach number in the test section of the tunnel is uniform within ± 0.005 Mach number. The comparative turbulence level of the flow relative to a number of supersonic facilities has been established from boundary-layer transition tests of a right circular cone; the level of turbulence is believed low enough to be ignored for this series of tests.

No corrections have been applied to the data to account for tunnel wall effects. The model blockage of about 0.6 percent, based on the base area of the standard flare, is believed sufficiently small that no corrections are necessary.

Normal and axial forces of the model were measured by the strain-gage balance. These forces were resolved into lift, drag, and pitching-moment coefficients about a moment center at 50 percent of the model length. Base axial-force coefficients were determined from static-pressure measurements at the model base. The precision of the lift, drag, and pitching-moment coefficients is believed to be within ± 0.025 , ± 0.025 , and ± 0.030 , respectively.

RESULTS AND DISCUSSION

Static Force and Moment Characteristics

Effect of nose shape.- The pitching-moment, lift, and drag characteristics of the cylinder-flare¹ models showing the effect of degree of nose bluntness are presented in figure 6. For the oblate-nosed model, the nonlinear variation of pitching-moment coefficient with angle of attack at the lower subsonic Mach numbers and the hysteresis loops² in the pitching-moment and lift curves at transonic Mach numbers were, in essence, the same phenomena observed in reference 1 for similar models of approximately the same degree of bluntness. As originally discussed in reference 1, both of these static moment characteristics were a result of flow separation. At the lower subsonic Mach numbers, the flow separated symmetrically at 0° angle of attack near the nose-body juncture. Under these conditions, there was a nonlinearity in the moment curve because the flow became attached on the lower surface and more separated on the upper surface with increasing angle of attack. The effect of increasing Mach number was to eliminate the nonlinearity at zero angle of attack at about 0.98 Mach number and thus presumably attach the flow for the oblate-nosed flared model (see fig. 6(a)). Reference 1 shows hysteresis loops occurred only if the flow was initially attached at 0° angle of attack. Increasing the angle of attack separated the flow at an angle of attack mainly dependent on nose shape and Mach number. The hysteresis loops developed if, after the flow was separated, the angle of attack was decreased since reattachment occurred at a lower angle of attack than separation. Such a loop represented two stable flows, one attached, the other separated. For models freely oscillating at amplitude sufficient to enclose the loop, it is apparent the traverse of the loop creates an energy exchange by virtue of a nonconservative restoring force that can amplify the motion. Moreover, for free flight, the possible coupling of the pitching and plunging modes due to loops in both the pitching-moment and lift curves should not be overlooked.

It is apparent from figure 6 that the model with the prolate nose was essentially free of both subsonic nonlinearities and hysteresis loops in the static moment and lift characteristics. Thus if a prolate nose is used, the undesirable nonlinearities and hysteresis loops that characterize the restoring functions of extremely blunt-nosed shapes can be avoided while some measure of bluntness is retained. A more detailed discussion of favorable nose shape substantiated by pressure-distribution data will be given later.

¹Unless otherwise stated the flare is the standard 16.5° flare.

²The end points of the loops were obtained by observing the angle of attack at which abrupt changes occurred in the force and moment data.

The spherical nose was about the dividing point in degree of nose bluntness as to whether hysteresis loops did or did not occur. In this regard, it can be observed from figure 6(a) that a discontinuous break in the pitching-moment curve occurred but without a noticeable hysteresis loop; the data for an up and down traverse of angle of attack indicate that separation and reattachment occurred at a unique angle.

Figure 6(b) shows that when a loop or discontinuity due to separation occurred in the lift curves, the effect of flow separation was to increase the lift. This is contrasted to a decrease in lift shown in reference 5 for separation of blunt shapes without a cylindrical body and flare. Of interest is the approximate independence of pitching moment and lift on nose shape at a Mach number of 0.60 and at the higher Mach numbers before flow separation occurred. The flow at a Mach number of 0.60 for the oblate-nosed model is believed only partially separated and it appears that if the flow remained attached, the pitching-moment and lift characteristics would be closely similar for all three nose shapes.

Effect of flare.- The static characteristics of the prolate- and oblate-nosed models without the flare are compared in figure 7. Shadow-graph pictures to be presented later show the flow separation on the oblate model without the flare was similar to that on the model with the flare. The effect on the flow separation phenomenon of removing the flare was mainly to allow the flow to attach at a slightly lower subsonic Mach number at 0° angle of attack and to require a higher angle of attack to separate the flow. Also the hysteresis loops were observed to extend over a generally greater range of angles of attack than was the case with the flare.

In contrast to the nonlinear pitching-moment curves of the oblate model with the flare at subsonic Mach numbers, the pitching-moment curves of the model without the flare are nearly linear. From this it is concluded that when the flow was separated, the flare made a nonlinear contribution to the pitching moment. Similarly from the data presented for the prolate-nosed model with and without the flare, it is concluded that when the flow was attached, the flare made a linear contribution to the pitching moment. In either case the pitching-moment contribution of the flare was highly stabilizing.

Effects of increased flare size.- Figure 8 presents data showing the static longitudinal characteristics of the model with the extended flare. As previously illustrated in figure 2, extending the flare represented an increase in flare length and base diameter but a decrease in flare angle. Such changes did not significantly influence the advantageous characteristics of the prolate nose. In fact extending the flare increased the static margin slightly. From a different point of view,

it appears that for this cylindrical body length, increasing the ratio of flare to body length provided a more rearward center of pressure without creating unfavorable flow separation.

General comparisons.- Parameters useful for an evaluation of the static stability characteristics of the various configurations are presented in figures 9 to 12. These comparisons have been made for an angle of attack of 0° since, because of symmetry, it was assumed that 0° represented the trim angle.

The center-of-pressure position of the various configurations presented in figure 9 shows that the oblate-nosed cylinder-flare model had the most rearward center-of-pressure position and the widest variation with increasing Mach number. These effects were due primarily to the flare being immersed in separated flow at subsonic Mach numbers, as previously discussed, and were confined to low angles of attack. While such rearward positions of the center of pressure may be advantageous for missiles restricted to subsonic Mach numbers, the data of reference 6 indicate that dynamic instability may be a problem. The effect of increasing nose fineness ratio was to produce a more nearly constant center-of-pressure position for the transonic Mach number range. Although the prolate-nosed cylinder-flare model had a more forward center-of-pressure position, it is believed sufficiently far aft (generally behind the 45- and 50-percent body length with the standard and extended flare, respectively) to place the restriction on center of gravity of a ballistic-type missile outside the transonic Mach number range.

The lift and normal-force curve slopes presented in figures 10 and 11, respectively, are substantially greater at subsonic Mach numbers for the oblate-nosed model with the flare than for those models having increased nose fineness ratio. This was a characteristic of flare interaction with flow separation but once the flow attached, the lift and normal-force curve slopes were only weakly dependent on nose shape.

Figure 12 presents a comparison of the zero-lift total- and base-drag coefficients of the various models. A level of drag coefficient based on the Newtonian flow concept is shown for interest since this concept makes an acceptable estimate of the hypersonic drag. Clearly from these results the prolate-nosed model had significantly lower drag throughout the Mach number range. At transonic Mach numbers, a large part of the total drag resulted from base drag as shown in figure 12. In contrast, the Newtonian estimate of the hypersonic drag that is presented here neglected base drag completely.

Dynamic Stability Characteristics

Stability at 0° angle of attack.- Data from references 1, 2, and 6 have been compiled in figure 13 to show the dynamic stability characteristics of several cylinder-flare models for a wide range of Mach numbers at 0° angle of attack. The forced oscillation technique at an amplitude of $\pm 1^\circ$ was utilized to obtain the data of references 1 and 6 whereas free oscillation was employed for the data of reference 2. No attempt was made to reduce the data about a common pitching axis; the data span a range of pitching axes from 39.6 to 56.3 percent of model length. The data of reference 6 were obtained from tests of the same models as the present investigation and are correspondingly labeled prolate, spherical, and oblate. Except for a slight difference in nose contour, the model of reference 1 was similar to the oblate model of this investigation.

The data presented in figure 13 show, although perhaps not rigorously, that for a wide range of diverse nose shapes, cylinder-flare models are dynamically stable, provided the flow is not separated. Of the various nose shapes considered, only the prolate-nosed model was completely free of transonic dynamic instability at 0° angle of attack. The results further show for Mach numbers from about 0.98 to 1.15 and at a Mach number of 6.83 that dynamic stability of cylinder-flare models was not unduly dependent on nose shape. Unpublished data from Ames free-flight facilities have indicated dynamic stability for several other cylinder-flare configurations at hypersonic Mach numbers. On this basis and because stability of the oblate model of reference 1 was only mildly influenced by increasing Mach number from 1.0 to 2.2, it would seem reasonable to expect that the prolate-nosed model would also be dynamically stable at supersonic and hypersonic Mach numbers.

The marginal stability of the prolate-nosed model at a Mach number of 0.60 is of questionable practical significance for ballistic-type missiles since terminal Mach numbers would likely be greater than 0.6. This marginal stability may be due to the data being taken about a pitching axis at 56.3 percent of model length; this is considerably aft of a statically stable and more realistic moment-center position. In this regard, the experimental data of reference 7 show that dynamic stability of blunt shapes generally increases with forward movement of the pitching axis at supersonic Mach numbers.

Effect of angle of attack.- Data presented in references 1 and 6 for cylinder-flare models show that the one-degree-of-freedom damping parameter ($C_{m_{\dot{\alpha}}} + C_{m_{\dot{\alpha}_0}}$) is, in general, a nonlinear function of angle of attack. Results of the nonlinear damping presented in reference 6 have been summarized in figure 14 to show the angle-of-attack ranges of the various nose shapes for which energy input to the system (positive damping) will occur. Also shown is the range of angles of attack for which

energy input through hysteresis loops in the pitching-moment curves will occur for the oblate-nosed model. The type of functional relationship with angle of attack providing energy input through nonlinear damping or static pitching-moment loops is illustrated by the inset curves of figure 14. The extent to which any of these data are dependent on frequency is not known.

Depending on the magnitude of energy exchange and on the initial conditions, any of the types of damping functions shown in figure 14 are capable of self-sustained oscillations with a limit amplitude if one-degree-of-freedom oscillation is considered. Under the reasonable conditions of small initial pitch displacement and pitch velocity, limit amplitude motion would ensue only for the oblate-nosed model at Mach numbers from about 0.60 to 0.95 and at a Mach number near 0.90 for the spherical-nosed model. Oscillations would not occur for the prolate-nosed model within the transonic Mach number range unless unrealistic initial conditions of high angle of attack and velocity or combinations thereof were prescribed. In a practical sense, figure 14 demonstrates that for a one-degree-of-freedom analysis, the prolate-nosed model is the only one of the three nose shapes that is dynamically stable for a pitching range of about $\pm 9^\circ$.

Flow Visualization and Pressure Distribution

Static-pressure distribution and shadowgraph pictures of the flow over the various models are presented in figures 15 to 20. Table II is presented to facilitate locating the data. All data presented were obtained with the angle of attack increasing, thus excluding other stable flows that are characterized by decreasing the angle of attack.

The dark regions of the shadowgraphs that partially obscure the flow are window frames of the tunnel side walls.

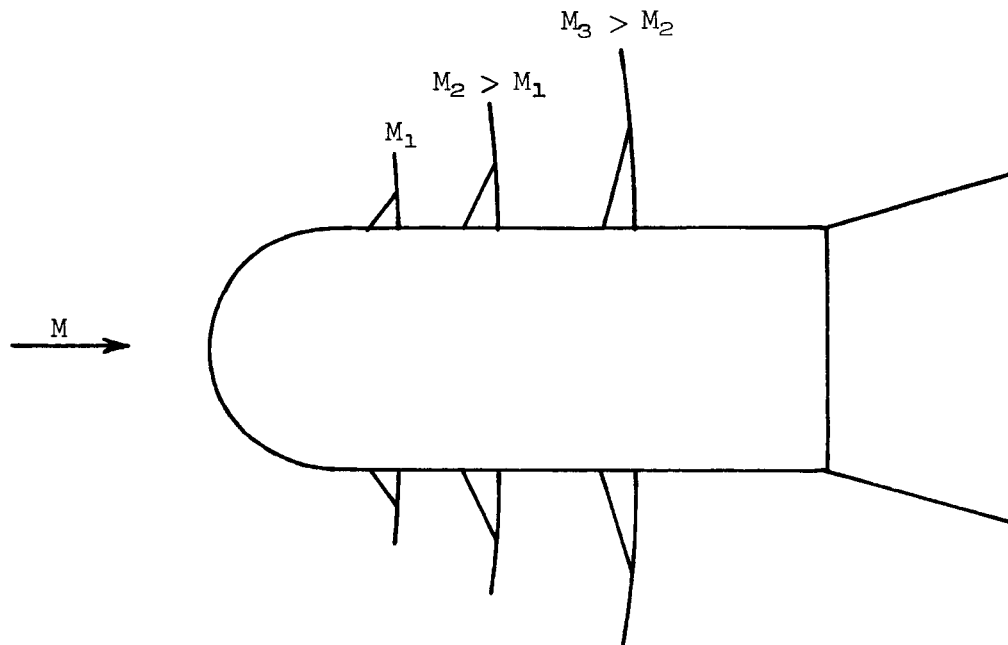
Attached flow boundary layer.- No specific measurements were made to determine to what extent the boundary layer was laminar or turbulent. However it is believed that some details of the boundary layer can be ascertained from the large shadowgraph pictures that were obtained. Figure 21 shows a section of a full-scale shadowgraph of the prolate-nosed model in the region where transition is believed to occur. There is little doubt that the boundary layer to the right of the arrow was turbulent. The extent of the laminar flow and the end of transition, however, are not clear. Because of the favorable gradient over the nose and the three-dimensional nature of the flow, laminar flow is believed to have prevailed to at least the model station at which the peak negative pressure coefficient occurred. This is supported to some extent by the laminar appearance of the white layer adjacent to the model covered

by a dark layer at what seems to be the outer edge of the boundary layer. Although the shadowgraph pictures presented in figures 15 to 20 are not clear with regard to these boundary-layer details, the full-scale shadowgraph pictures showed that for all models of this investigation the boundary-layer characteristics were of the type just described when the flow was attached.

Attached flow.- Before considering the problem of flow separation, a discussion of the general features of the attached flow pressure distribution is in order. While the three-dimensionality of blunt bodies with curved surfaces would be expected to be a relieving factor in the magnitude of the negative pressure coefficient that would be achieved, for sufficiently blunt nose shapes it is possible to attain a pressure coefficient at which local sonic velocity will occur at relatively low subsonic Mach numbers. For example on the basis that the flow was attached, the lower critical Mach number for the oblate-nosed model was estimated to be less than 0.60 at 0° angle of attack. Provided the flow is attached and subcritical, the pressure coefficients of the various models at zero angle might be expected to increase approximately in accordance with Gothert's rule (ref. 8) with increasing Mach number. However, since the models were not affinely related, Gothert's rule could not be applied to check the experimental results. Because the noses of the models were affinely related, an attempt was made to correlate the peak negative pressure coefficients on the basis of the coordinates given in figure 22. Provided the flow was attached, reasonable correlation is indicated for all three nose shapes at equal angles of attack.

Cause of flow separation.- It is important to note that flow separation may result in a maximum negative pressure coefficient less than that for attached flow at subsonic Mach numbers. This was the case for the oblate- and spherical-nosed models, but not for the prolate-nosed model. Once the critical Mach number was exceeded, the local embedded supersonic regions that formed were terminated by a system of compression waves or shocks. These shocks occurred in a region where the flow was already undergoing a significant pressure rise as a result of the basic subsonic type of pressure distribution and may, therefore, go unnoticed or be difficult to detect from static-pressure measurements. This was the case with the spherical-nosed model at 0.80 Mach number and 0° angle of attack as shown by the pressure and shadowgraph data in figures 16(d) and (e). The presence of a system of shock waves may steepen the pressure gradient and promote separation of the flow. The spherical-nosed model at 0.80 Mach number and 0° angle of attack was a marginal example of the type being considered where the flow did not completely separate but significant thickening of the boundary layer was observed (see fig. 16(d)). For the oblate-nosed model which was blunter than the spherical-nosed model the flow separation changed the flow completely to a new stable type where now a system of local Mach lines appears (fig. 17(d)) with no

significant shocks. The shocks increased in strength and stood at a more rearward position with increasing Mach number, as shown in sketch (a), and having passed downstream of the nose, the possibility of shock-induced flow separation was removed. Thus at the higher subsonic Mach



Sketch (a)

numbers, even the blunter nose shapes had attached flow. For the model without the flare, the shock passed completely over the model at all Mach numbers greater than about 1.0 as shown in figures 18(d) and 18(f). If the cylinder had a flare, the shock stood ahead of the flare (see fig. 20(g)) and with increasing Mach number, approached the flare and became more conical.

Although the shear in the boundary layer was not determined experimentally, it is believed to be an important factor in the separation phenomenon. It is evident that because of the large induced velocities and the three-dimensional aspect of the flow, the shearing rate in the boundary layer was high.

Figure 23 presents a condensed illustration of the effect of Mach number on the attached flow pressure distribution of the three models. The pressure distribution with partially separated flow of the oblate-nosed model at 0.60 Mach number was included since it closely resembled the attached flow type. It can be seen that the major effect of increasing nose bluntness at all Mach numbers was to increase the peak negative

pressure coefficient at or just forward of the nose-body juncture. It is clear that pressure gradients measured along the surface are more severe for nose shapes of increasing bluntness by virtue of both higher peak negative pressures and the shorter distance over which recovery occurred. The effect of increasing Mach number from 0.60 to 1.15 was to reduce markedly the peak negative pressure coefficient for the oblate-nosed model and to reduce the attendant pressure gradients that followed. As a result, at 0° angle of attack the flow attached on the oblate-nosed model at about 0.98 Mach number and remained attached for all higher Mach numbers.

A
2
9
6
Increasing angle of attack increased the negative pressure coefficients over approximately the upper half of the model at all Mach numbers provided the flow was attached (see figs. 15 to 20). Of interest is the large effect of angle of attack on the pressure distribution at $\theta = 90^\circ$ (the side row of orifices) for model longitudinal stations a short distance from the nose. This is indicative of a strong crossflow component and shows that the three-dimensional end effect of the flow was confined to the forward part of the model.

Flow separation.- The existence of flow separation can be easily discerned from the shadowgraphs as shown for example in figure 17(d). Separation was manifested in the pressure distributions by a collapse in the peak negative pressure coefficient on the upper surface of the nose with increasing angle of attack as shown in figures 17(e), 17(g), and 17(i). Also at subsonic Mach numbers when the flow was separated at 0° angle of attack the peak negative pressure coefficients were significantly lower than they would have been if the flow were attached. Interestingly enough, both of these evidences of separation existed for the oblate model at 0.80 Mach number (see fig. 17(e)) lending evidence to the belief that the type of separation occurring at 0° angle of attack was not complete but rather a highly turbulent, unsteady, and thick boundary layer. The fact that the attached flow peak negative pressure coefficient was not achieved for the oblate nose at 0° angle of attack can be deduced from the data of figure 17(a).

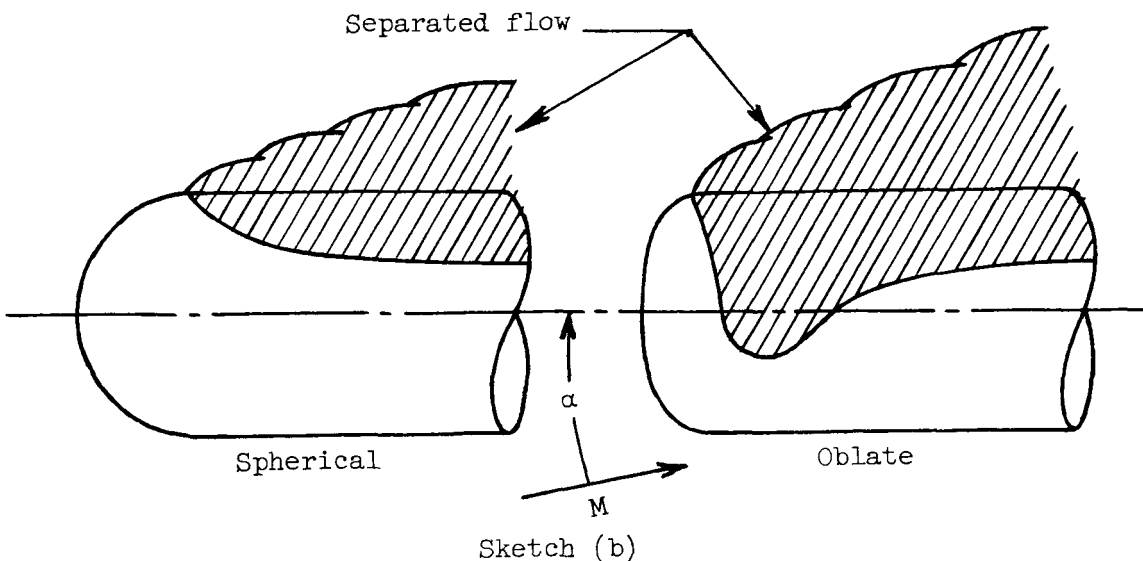
If the flow was incompletely separated at 0° angle of attack, complete separation occurred gradually with increasing angle of attack. As shown in figure 17(e) for θ of 0° , the peak first increased with increasing angle of attack, then decreased until at about 12° a saddle-type pressure distribution was formed. This was in contrast to a more abrupt type of separation that occurred to form hysteresis loops in the force data if the flow initially was completely attached (see fig. 17(i)).

Without the flare, separation occurred near the nose-body juncture on the oblate-nosed model but did not occur on the prolate-nosed model; thus it is clear that degree of nose bluntness or nose shape is the dominating factor to be considered in the transonic separation problem. In

particular, the magnitude of the peak negative pressure coefficient, which in turn was dependent on nose curvature, is considered to be an important factor governing whether the flow would separate or attach. This point is illustrated in some detail by plots of the peak negative pressure coefficient of the three nose shapes versus Mach number presented in figure 24. It can be seen from this figure that the range of Mach numbers and angles of attack for which the flow was separated was greatest for the oblate-nosed model which also had the highest peak negative pressure coefficients when the flow was attached. As a rough rule-of-thumb, it would appear that separation could be avoided by selecting a nose shape having maximum negative pressure coefficients not exceeding about -0.9 .

Separation boundaries have been superimposed on the plots of figure 24 to show approximate values of peak negative pressure coefficient and angle of attack for which separation or hysteresis loops will likely occur. The important but perhaps secondary influence of removing the flare is to raise and extend this boundary. This effect is believed due to some relief by removing the flare on the over-all pressure gradient following the peak negative pressure coefficient. Thus it would seem that a shallow flare angle or possibly longer body length could be resorted to as a means of coping with an otherwise marginal separation problem.

It is anomalous that the separation boundary of the spherical-nosed model is lower than that of the oblate-nosed model (see fig. 24). A possible explanation for this may lie in the smaller extent of the separated region of the spherical-nosed model. The approximate extent of separated flow as obtained from the pressure distributions is as shown by sketch (b).



The more three-dimensional aspect of the separated region of the oblate model was indicative that the higher negative pressures achieved along the sides of the oblate nose offer some restraint to keep the flow from separating until a higher peak negative pressure coefficient was achieved.

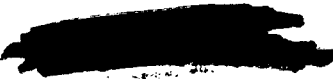
Hysteresis loops.- The hysteresis loops in the moment and force data represent a range of angles of attack for which both stable attached and separated flow existed. The hysteresis phenomenon is discussed in some detail in reference 1. The pressure distributions for these two types of stable flows are compared in figure 25 for an angle of attack of 12° and a Mach number of 1.15. Also shown are the approximate shock patterns and regions of flow separation at the model surface. It is apparent from these data that the effects of flow separation are felt primarily on the upper half of the model. Near the nose, flow separation extended around the periphery of the model from θ of 0° to past θ of 90° . Because of the abruptness with which the separation occurred during the tests, the history of the separation phenomena was not established. On the basis of pressure distributions before and after separation, it appears reasonable to assume that separation was initiated at the top of the model where the peak negative pressure coefficient was observed and then spread rapidly over the upper surface of the model as exemplified in figure 25.

Normal-shock pressure distribution.- The designation "normal-shock pressure distribution" has been assigned to a technique relating subsonic and supersonic pressure distributions of blunt bodies through normal-shock and isentropic flow relations. The principle is developed in detail in the appendix from which is obtained a relation between pressure coefficient based on flow properties downstream of a normal shock to the true free-stream pressure coefficient. This relationship for air is:

$$C_p = \frac{M^2 + 5}{6M^2} C_{p_1} + \frac{10(M^2 - 1)}{6M^2}$$

where the subscript 1 applies to the flow downstream of a normal shock. By the nature of the assumptions, this relationship is confined to a Mach number range near unity and is similar in principle to the Mach number freeze concept (see ref. 8). For a specified free-stream Mach number greater than unity, it is evident that a linear relation exists between the pressure distribution at that Mach number and its counterpart at a subsonic Mach number.

The validity of the concept has been checked with the pressure data obtained from this investigation and the results are shown in figure 26. It can be seen that the data for all three nose shapes are in good



agreement with the calculated line at a Mach number of 1.1. At the more negative values of pressure coefficient and for pressure stations after the peak there is a slight departure from the calculated line.


Nose Selection

Reference 9 presents heat-transfer data that show the advantages of maximum nose bluntness to achieve minimum rates of heat transfer. Bluntness increases the drag and is also advantageous for the heat sink method of cooling because the missile decelerates rapidly and thereby the total heat input is reduced. These advantages of extreme nose bluntness dictate a shape opposite to one having desirable transonic stability characteristics. However, transonic stability may be of considerable importance in the selection of nose shape when the heating loads associated with the slimmer nose shapes can be controlled by other means such as ablative cooling. The problem may then be to decide what nose shape should be used for a specified ratio of nose length to body diameter. For this case, the results of this investigation clearly demonstrate distinct advantages by shapes with generous radii of curvature at and near the nose-body juncture to avoid transonic flow separation.

The prolate-ellipsoidal-shaped nose appears to be one offering a good compromise between a generous radius of curvature at the nose-body juncture while still retaining a measure of bluntness at the stagnation point. In contrast, a blunted conical nose shape having the same ratio of nose length to body diameter and the same nose radius as the prolate nose would, because of its linear element, have a sharper radius at the nose body juncture. Other nose shapes, such as a Rankine oval, may prove more desirable than the ellipsoid for a specified ratio of nose length to body diameter.

CONCLUSIONS

Conclusions deduced from transonic wind-tunnel tests of a flare-stabilized cylinder having ellipsoidal noses of varying degrees of bluntness are:

1. The subsonic and transonic separation phenomena of extremely blunt-nosed cylinder models characterized by symmetrical flow separation at 0° angle of attack at subsonic speeds and by hysteresis loops at angle of attack at transonic speeds were alleviated by nose shapes that had a generous radius of curvature at or near the nose-body juncture. A prolate-ellipsoidal nose of semimajor-to-semiminor axis ratio 2 eliminated the separation phenomena and still retained a significant degree of bluntness.
- 

2. The separation phenomenon was associated with high peak negative pressure coefficients that result from sharp curvature at or near the nose-body juncture. Such peak negative pressures promote extreme shear in the boundary layer and adverse pressure gradients causing separation of the flow.

3. For blunt-nosed bodies on which the flow was separated at 0° angle of attack at subsonic Mach numbers, flow reattachment occurred with increasing Mach number by virtue of a progressive change in the type of pressure distribution that diminished the peak negative pressure coefficients and the adverse pressure gradient. Once the flow was attached, however, an asymmetric separation occurred as a result of increasing angle of attack due to the development of a high negative pressure coefficient.

4. The change in the type of pressure distribution as Mach number increases from subsonic to supersonic was predicted by an extension of the Mach number freeze concept that, in general, applied to the experimental pressure distributions for Mach numbers from about 0.90 to 1.10.

5. The prolate-ellipsoidal-nosed cylinder-flare model appears to be a promising nonlifting configuration for a wide range of Mach numbers. This configuration was both statically and dynamically stable about a reasonable center-of-gravity position.

Ames Research Center

National Aeronautics and Space Administration

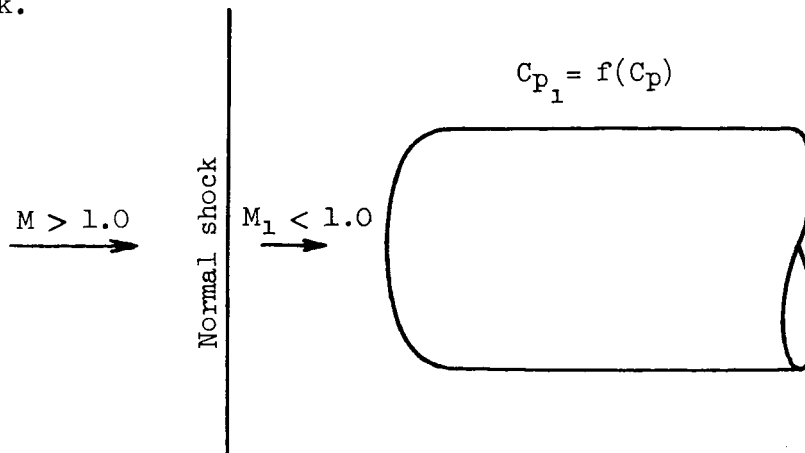
Moffett Field, Calif., Feb. 23, 1960

APPENDIX

NORMAL-SHOCK PRESSURE DISTRIBUTION

Normal-shock pressure distribution is derived from the assumption that a normal shock stands upstream from the model and thus the flow over the model is subsonic. Moreover the existence of a normal shock (no shock curvature) is assurance that the flow over the model is uniform and irrotational. This flow concept becomes more unrealistic, of course, as the Mach number becomes large compared to unity. Not only does the bow shock then become more curved but it also approaches nearer to the model, thus confining the region of subsonic flow. The utility of the concept will be to apply to the blunt-body pressure data a relation to be derived between pressure coefficient based on flow properties downstream of a normal shock and the usual definition of pressure coefficient based on free-stream flow properties. If applicable, such a concept would be useful in extending data obtained at Mach numbers slightly less than 1.0 to slightly supersonic Mach numbers. Although similar in principle to the Mach number freeze concept for transonic flows, the normal-shock technique utilizes the exact relation between Mach number upstream and downstream of a normal shock. It would appear from the assumptions that the technique is more applicable to blunt bodies than to slender pointed bodies.

The development of a relation between the pressure coefficient based on the flow properties downstream of the shock and the true free-stream pressure coefficient is obtained from the fact that the local pressure on the model is the same for both definitions of pressure coefficient. Sketch (c) illustrates the main features relating to the pressure coefficients; the subscript 1 refers to the subsonic flow downstream of the shock.



Sketch (c)

The definitions of pressure coefficient are

$$C_p = \frac{p_l - p}{q} \quad \text{and} \quad C_{p_1} = \frac{p_l - p_1}{q_1}$$

Equating the pressure, p_l , for both cases gives

$$C_{p_1} q_1 + p_1 = C_p q + p$$

or

$$C_{p_1} = C_p \frac{q}{q_1} + \frac{p}{q_1} - \frac{p_1}{q_1}$$

$$C_{p_1} = C_p \frac{q/p}{(q_1/p_1)(p_1/p)} + \frac{1}{(q_1/p_1)(p_1/p)} - \frac{1}{q_1/p_1}$$

From normal-shock and isentropic-flow relations for air with a ratio of specific heats of 1.4 (see ref. 10):

$$\frac{p_1}{p} = \frac{7M^2 - 1}{6}$$

$$\frac{q}{p} = 0.7M^2$$

$$\frac{q_1}{p_1} = 0.7M_1^2$$

$$M_1^2 = \frac{M^2 + 5}{7M^2 - 1}$$

Substituting in the functional relation between C_{p_1} and C_p gives

$$\begin{aligned} C_{p_1} &= C_p \left[\frac{0.7M^2}{0.7 \left(\frac{M^2 + 5}{7M^2 - 1} \right) \left(\frac{7M^2 - 1}{6} \right)} \right] + \frac{1}{0.7 \left(\frac{M^2 + 5}{7M^2 - 1} \right) \left(\frac{7M^2 - 1}{6} \right)} - \frac{1}{0.7 \left(\frac{M^2 + 5}{7M^2 - 1} \right)} \\ &= \frac{6M^2}{M^2 + 5} C_p + \frac{1}{0.7(M^2 + 5)} (6 - 7M^2 + 1) \end{aligned}$$

or

$$C_{p_1} = \frac{6M^2}{M^2 + 5} C_p - \frac{10(M^2 - 1)}{M^2 + 5}$$

In this form it can be seen that for a given Mach number, a supersonic pressure distribution is related to a subsonic one by an extension and a translation of its ordinates. Conversely, if C_p is expressed as a function of C_{p_1} ,

$$C_p = \frac{M^2 + 5}{6M^2} C_{p_1} + \frac{10(M^2 - 1)}{6M^2}$$

it is evident that subsonic pressure distributions are related to supersonic ones by a contraction and opposite translation of its ordinates. The assumptions, in general, limit the application of the linear relation between C_p and C_{p_1} to regions of flow over the model that are isentropic behind the normal shock.

A
2
9
6

REFERENCES

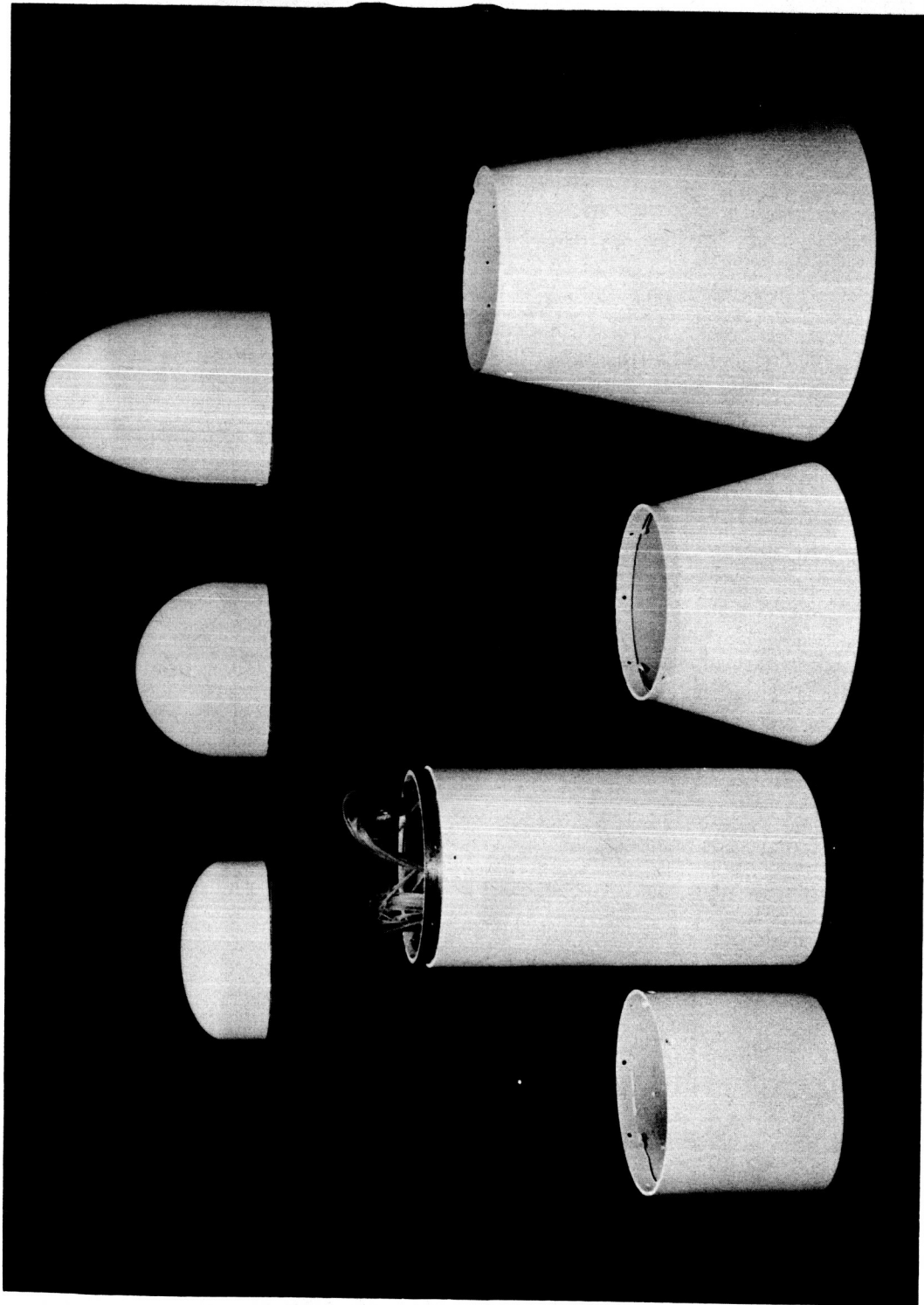
1. Reese, David E., Jr., and Wehrend, William R., Jr.: An Investigation of the Static and Dynamic Aerodynamic Characteristics of a Series of Blunt-Nosed Cylinder-Flare Models at Mach Numbers From 0.65 to 2.20. NASA TM X-110, 1959.
2. Fletcher, Herman S., and Wolhart, Walter D.: Damping in Pitch and Static Stability of a Group of Blunt-Nose and Cone-Cylinder-Flare Models at a Mach Number of 6.83. NASA MEMO 5-6-59L, 1959.
3. Hall, James R., and Graham, John B., Jr.: Aerodynamic Heating and Lateral Force Measurements of a Blunt-Nose Flare-Cylinder Configuration Undergoing Large Lateral Oscillations at Mach Numbers Up to 10.15. NASA TM X-45, 1959.
4. Van Dyke, Milton D.: The Supersonic Blunt-Body Problem - Review and Extension. Jour. Aero/Space Sci., vol. 25, no. 8, Aug. 1958, pp. 485-496.
5. Fisher, Lewis R., and Di Camillo, Joseph R.: Investigation of Several Blunt Bodies to Determine Transonic Aerodynamic Characteristics Including Effects of Spinning and of Extendible Afterbody Flaps and Some Measurements of Unsteady Base Pressures. NASA MEMO 1-21-59L, 1959.
6. Emerson, Horace F., and Robinson, Robert C.: The Transonic Damping in Pitch of Three Cylinder-Flare Models With Various Degrees of Nose Bluntness. NASA TM X-368, 1960.
7. Beam, Benjamin H., and Hedstrom, C. Ernest: The Damping in Pitch of Bluff Bodies of Revolution at Mach Numbers From 2.5 to 3.5. NASA TM X-90, 1959.
8. Liepmann, H. W., and Roshko, A.: Elements of Gasdynamics. John Wiley and Sons, Inc., New York, 1957.
9. Stoney, William E., Jr.: Aerodynamic Heating of Blunt Nose Shapes at Mach Numbers Up to 14. NACA RM L58E05a, 1958.
10. Ames Research Staff: Equations, Tables, and Charts for Compressible Flow. NACA Rep. 1135, 1953.

TABLE I.- PRESSURE ORIFICE LOCATION

Values of x/l , percent					
Prolate nose standard flare	Prolate nose no flare	Prolate nose extended flare	Spherical nose standard flare	Oblate nose standard flare	Oblate nose no flare
0	0	0	0	0	0
1.04	1.04	.845	1.16	.278	.278
3.15	3.15	2.56	3.10	.975	.975
5.96	5.96	4.85	5.03	2.02	2.02
8.78	8.78	7.13	6.77	3.41	3.41
11.55	11.55	9.42	8.90	4.46	4.46
14.40	14.40	11.70	10.80	5.50	5.50
17.20	17.20	14.00	12.80	6.54	6.54
20.00	20.00	16.30	14.70	7.94	7.94
22.82	22.82	18.50	17.90	11.40	11.40
25.63	25.63	20.80	24.40	18.40	18.40
28.50	28.50	23.10	30.80	25.30	25.30
34.10	34.10	27.70	37.30	32.30	32.30
39.70	39.70	32.30	43.70	39.30	39.30
45.35	45.35	36.80	50.20	46.20	46.20
51.00	51.00	41.40	56.60	53.20	53.20
56.60	56.60	46.00	63.10	60.20	60.20
62.20	62.20	50.50	69.50	67.10	67.10
67.90	67.90	59.70	77.90	76.20	76.20
73.50	73.50	67.30	83.30	82.00	82.20
80.90	80.90	71.80	89.50	88.70	89.20
85.50	85.60	76.30	95.70	95.30	96.20
90.90	91.40	80.80			
96.30	97.00	89.80			
		94.30			
		98.80			

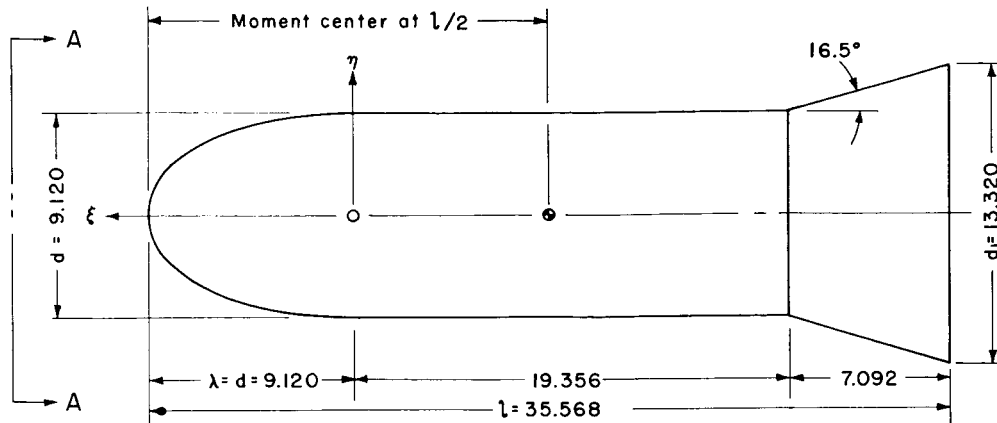
TABLE II.- PRESSURE DISTRIBUTION AND SHADOWGRAPH FIGURE LEGENDS

Model configuration		Mach number	Data	Figure
Nose	Flare			
Prolate	Standard	0.40	Pressure	15(a)
		.60	Shadowgraph	15(b)
		.60	Pressure	15(c)
		.80	Shadowgraph	15(d)
		.80	Pressure	15(e)
		1.05	Shadowgraph	15(f)
		1.05	Pressure	15(g)
		1.15	Shadowgraph	15(h)
		1.15	Pressure	15(i)
Spherical		.40	Pressure	16(a)
		.60	Shadowgraph	16(b)
		.60	Pressure	16(c)
		.80	Shadowgraph	16(d)
		.80	Pressure	16(e)
		1.05	Shadowgraph	16(f)
		1.05	Pressure	16(g)
		1.15	Shadowgraph	16(h)
		1.15	Pressure	16(i)
Oblate		.40	Pressure	17(a)
			Shadowgraph	
		.60	Shadowgraph	17(b)
		.60	Pressure	17(c)
		.80	Shadowgraph	17(d)
		.80	Pressure	17(e)
		1.05	Shadowgraph	17(f)
		1.05	Pressure	17(g)
		1.15	Shadowgraph	17(h)
		1.15	Pressure	17(i)
Prolate	None	.60	Pressure	18(a)
		.80	Shadowgraph	18(b)
		.80	Pressure	18(c)
		1.05	Shadowgraph	18(d)
		1.05	Pressure	18(e)
		1.18	Shadowgraph	18(f)
		1.18	Pressure	18(g)
Oblate		.60	Shadowgraph	19(a)
		.60	Pressure	19(b)
		.80	Shadowgraph	19(c)
		.80	Pressure	19(d)
		1.05	Shadowgraph	19(e)
		1.05	Pressure	19(f)
		1.16	Pressure	19(g)
Prolate	Extended	.60	Shadowgraph	20(a)
		.60	Pressure	20(b)
		.80	Shadowgraph	20(c)
		.80	Pressure	20(d)
		1.05	Shadowgraph	20(e)
		1.05	Pressure	20(f)
		1.15	Shadowgraph	20(g)
		1.15	Pressure	20(h)



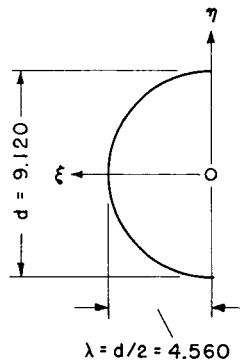
A-24717

Figure 1.- Components of the models.

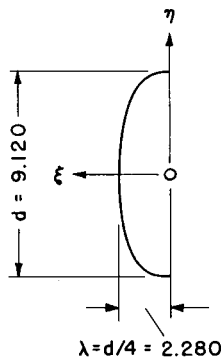


(a) Model with standard flare and prolate nose

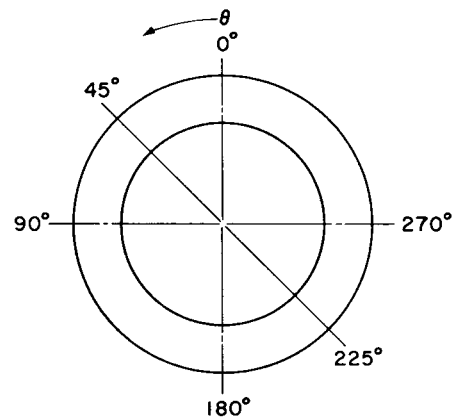
Equation of noses, $(\xi/\lambda)^2 + (\eta/d/2)^2 = 1$



Spherical nose

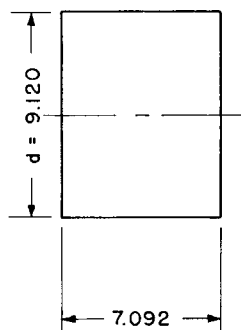


Oblate nose

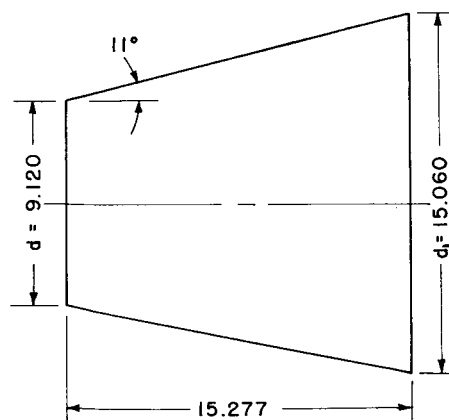
Pressure orifice rows
View A-A

(b) Alternate noses.

Dimensions in inches



Body extension



Extended flare

(c) Alternate flares.

Figure 2.- Dimensional details of the models.



Figure 3.- Oblate-nosed model mounted in the wind tunnel.

A-24711

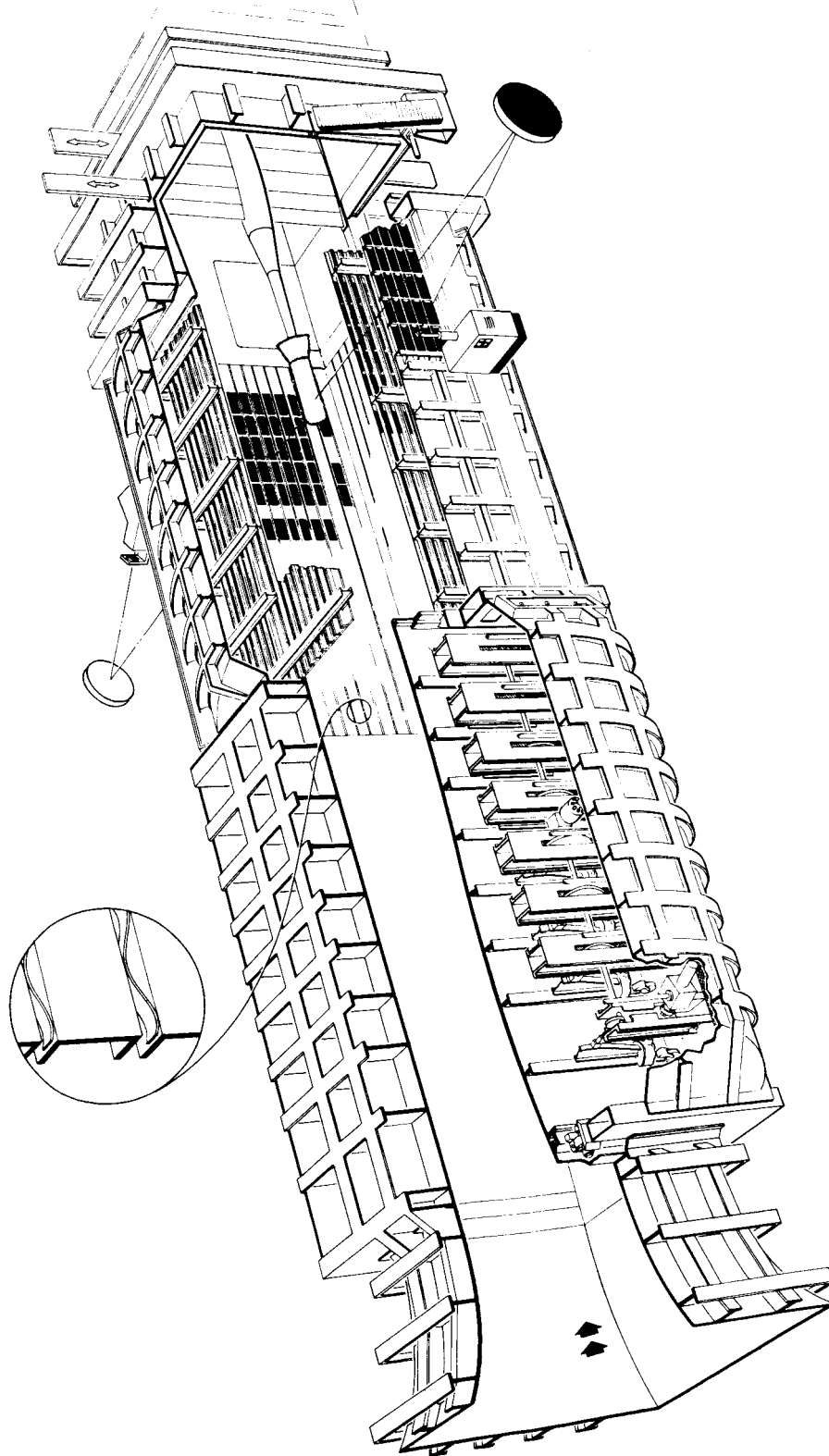


Figure 4.- Nozzle and test section of the 14-Foot Transonic Wind Tunnel.

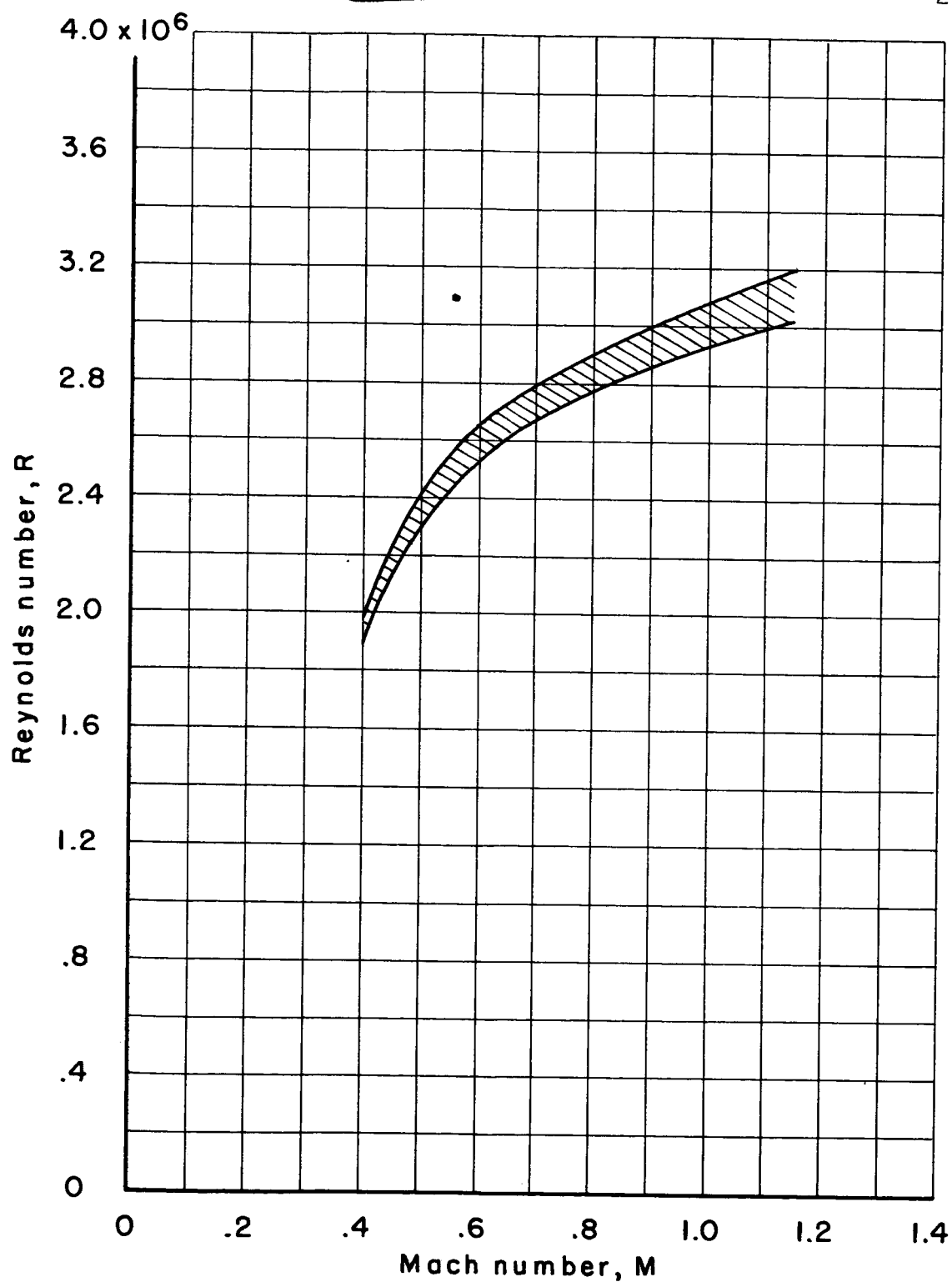
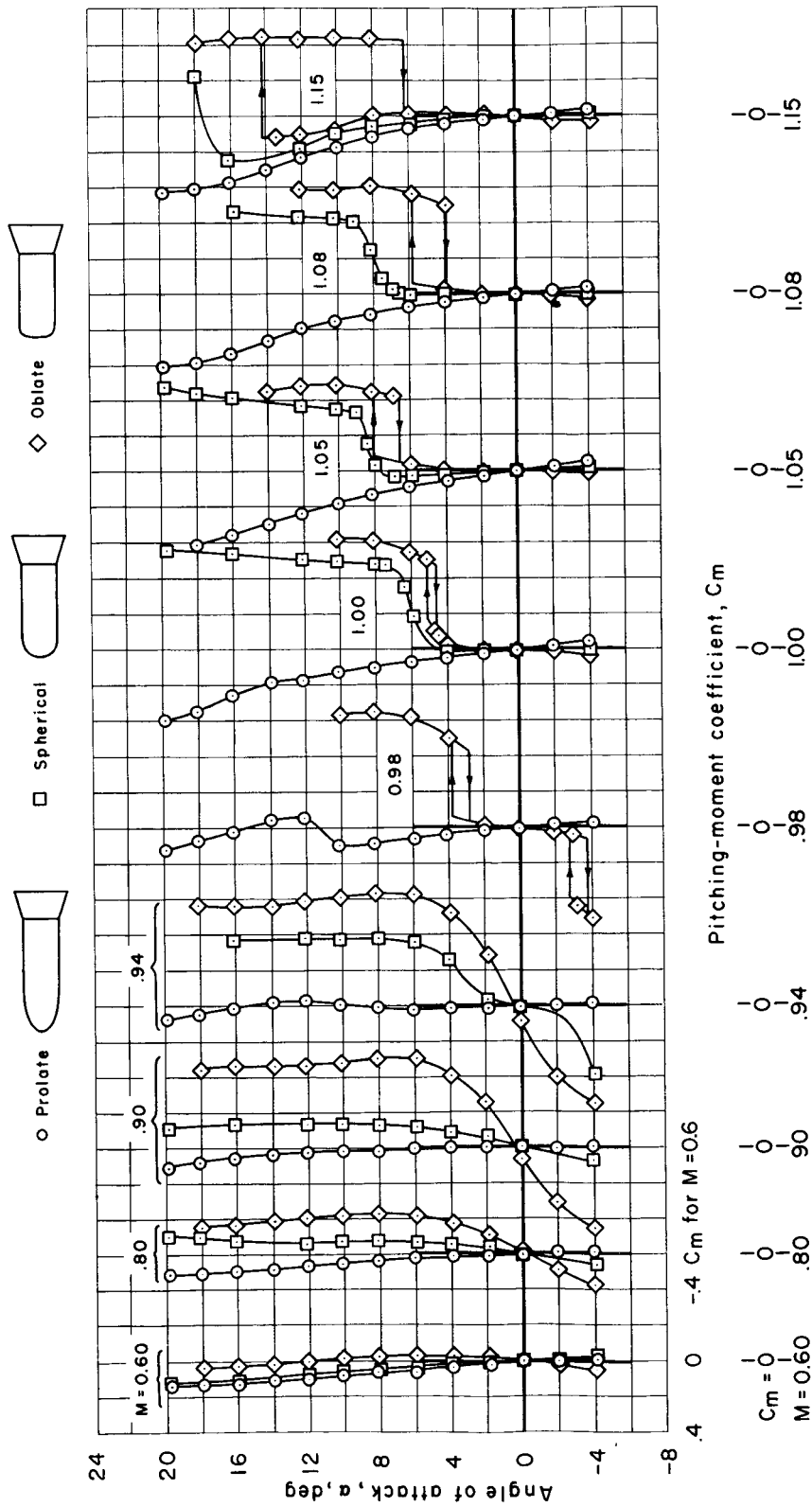
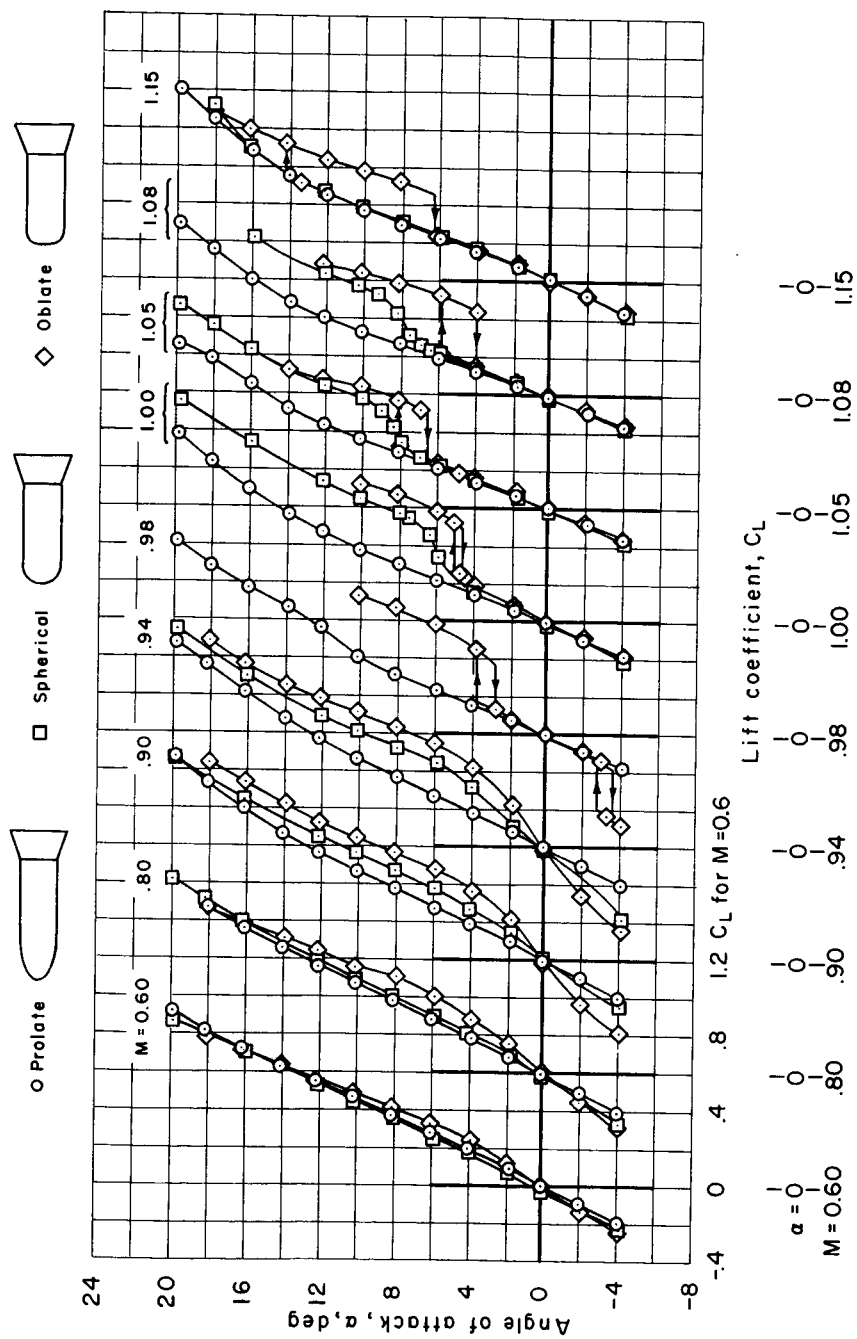


Figure 5.- Reynolds number range of the tests.



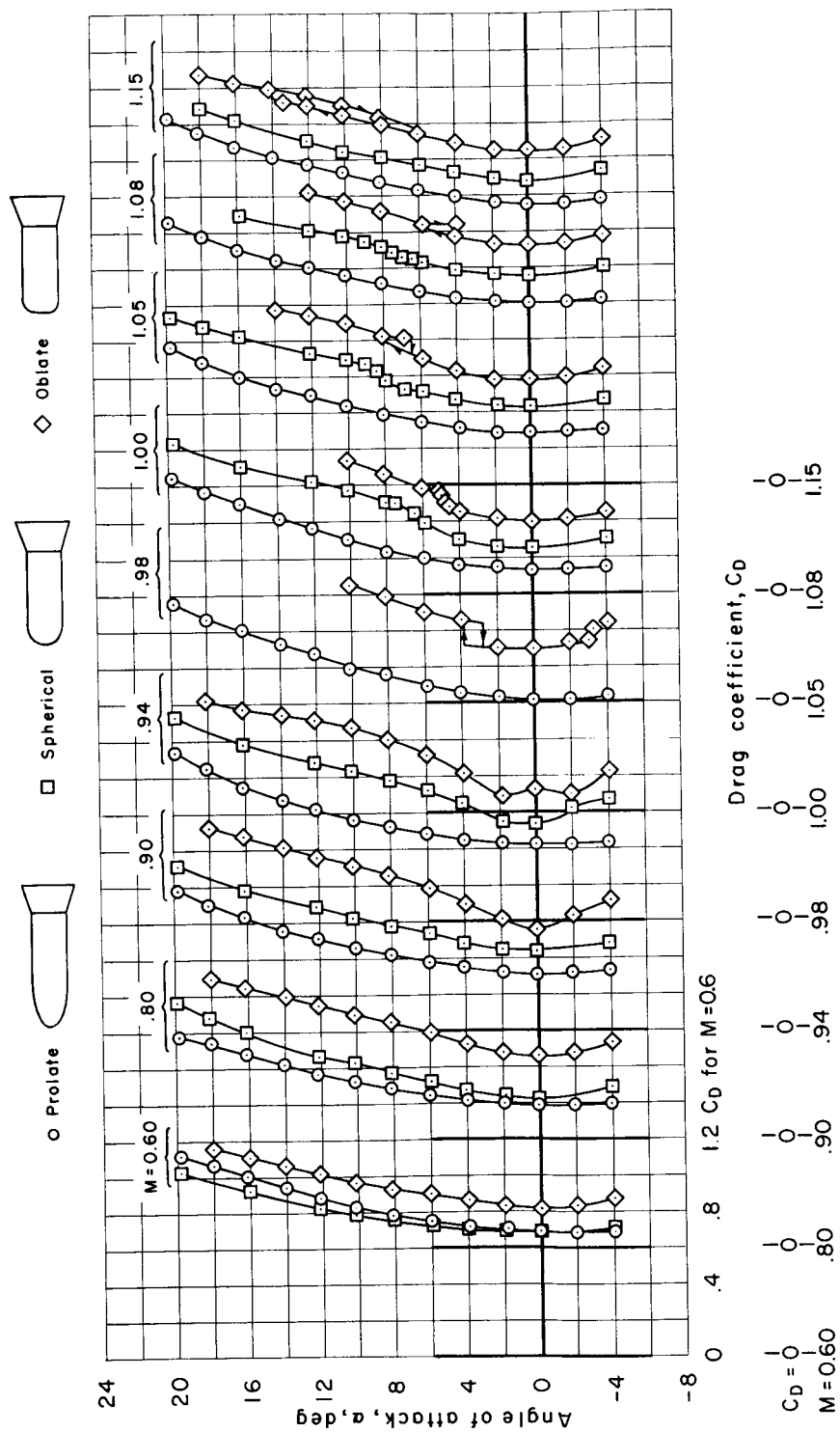
(a) Pitching-moment characteristics.

Figure 6.- The effect of nose shape on the pitching-moment, lift, and drag characteristics of the cylindrical body with the standard flare.



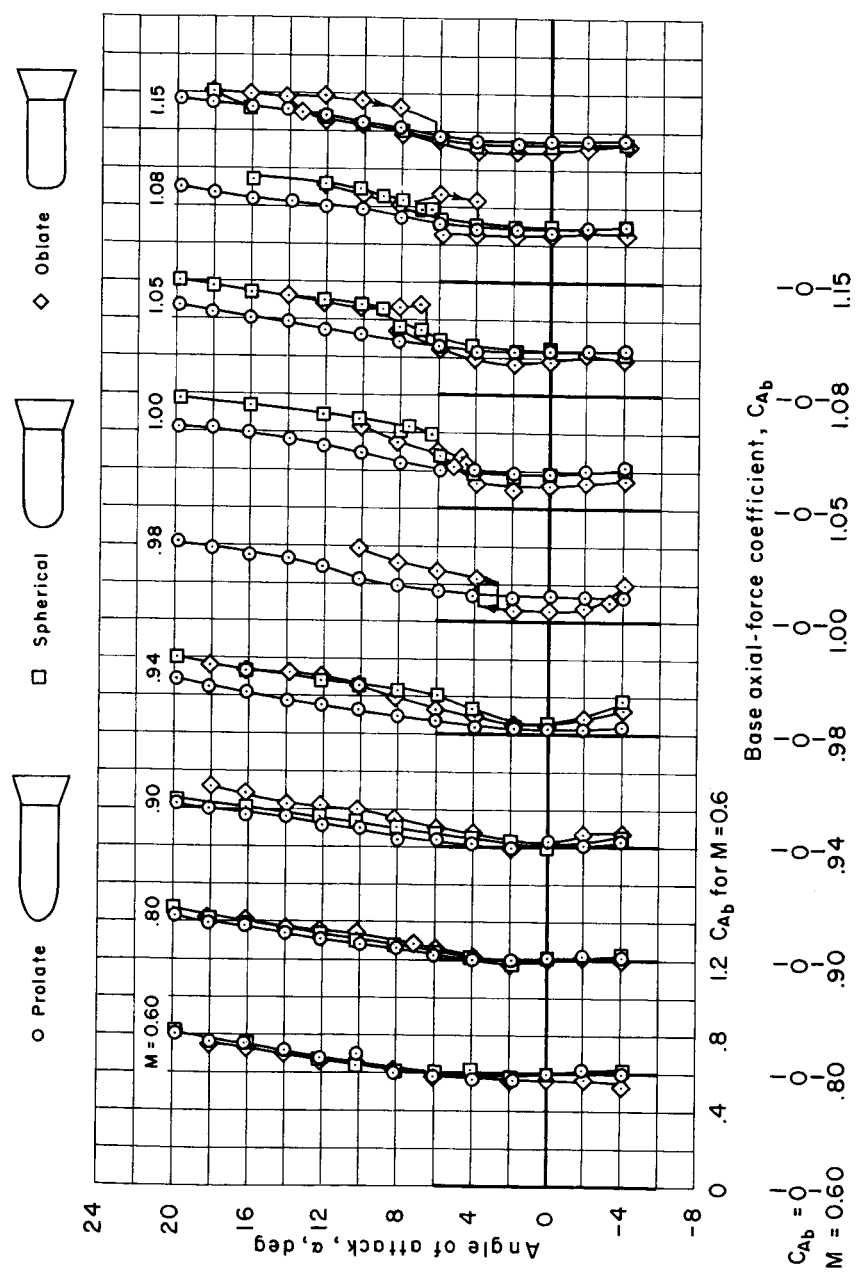
(b) Lift characteristics.

Figure 6.- Continued.



(c) Total-drag characteristics.

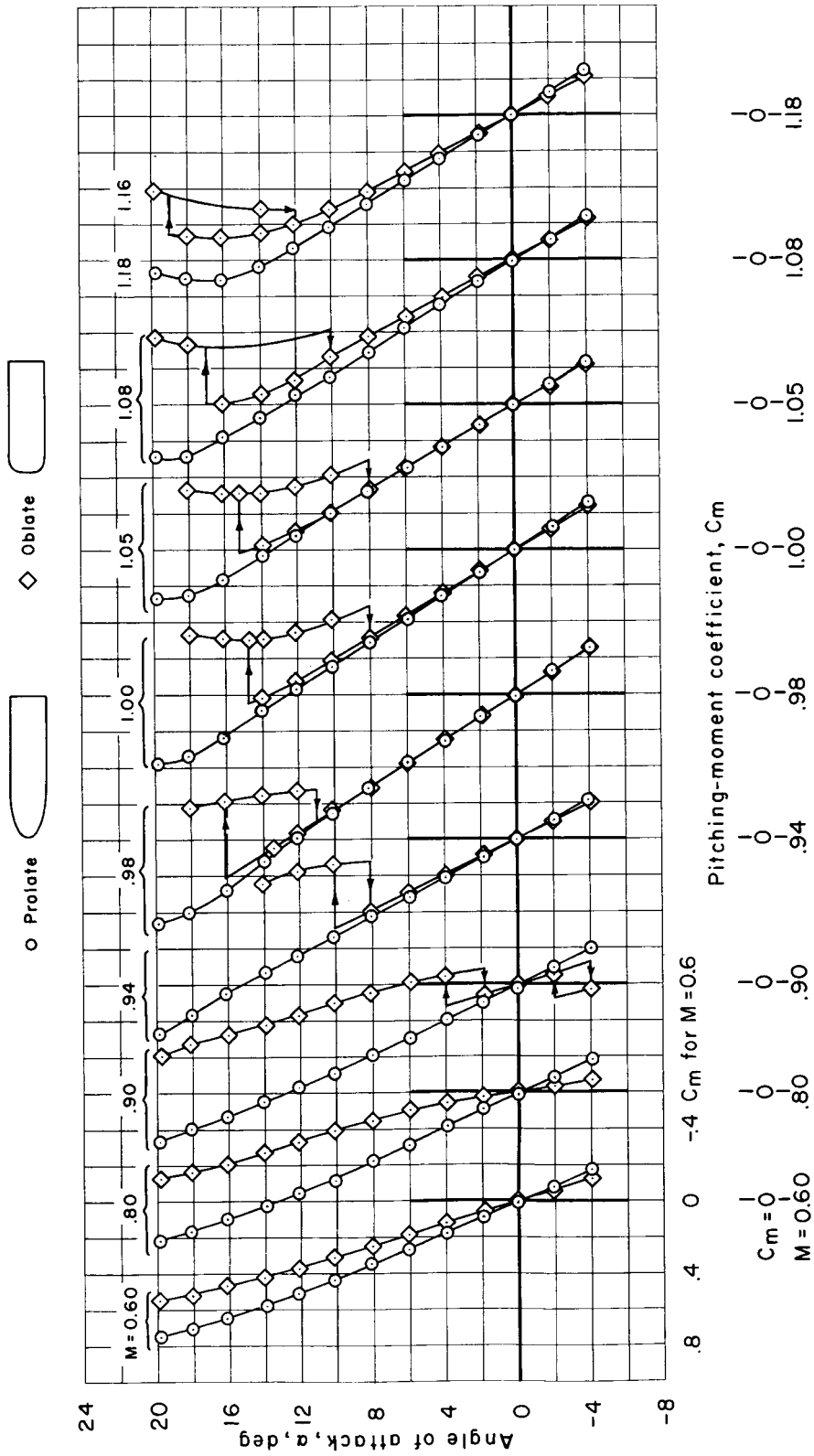
Figure 6.- Continued.



(d) Base axial-force characteristics.

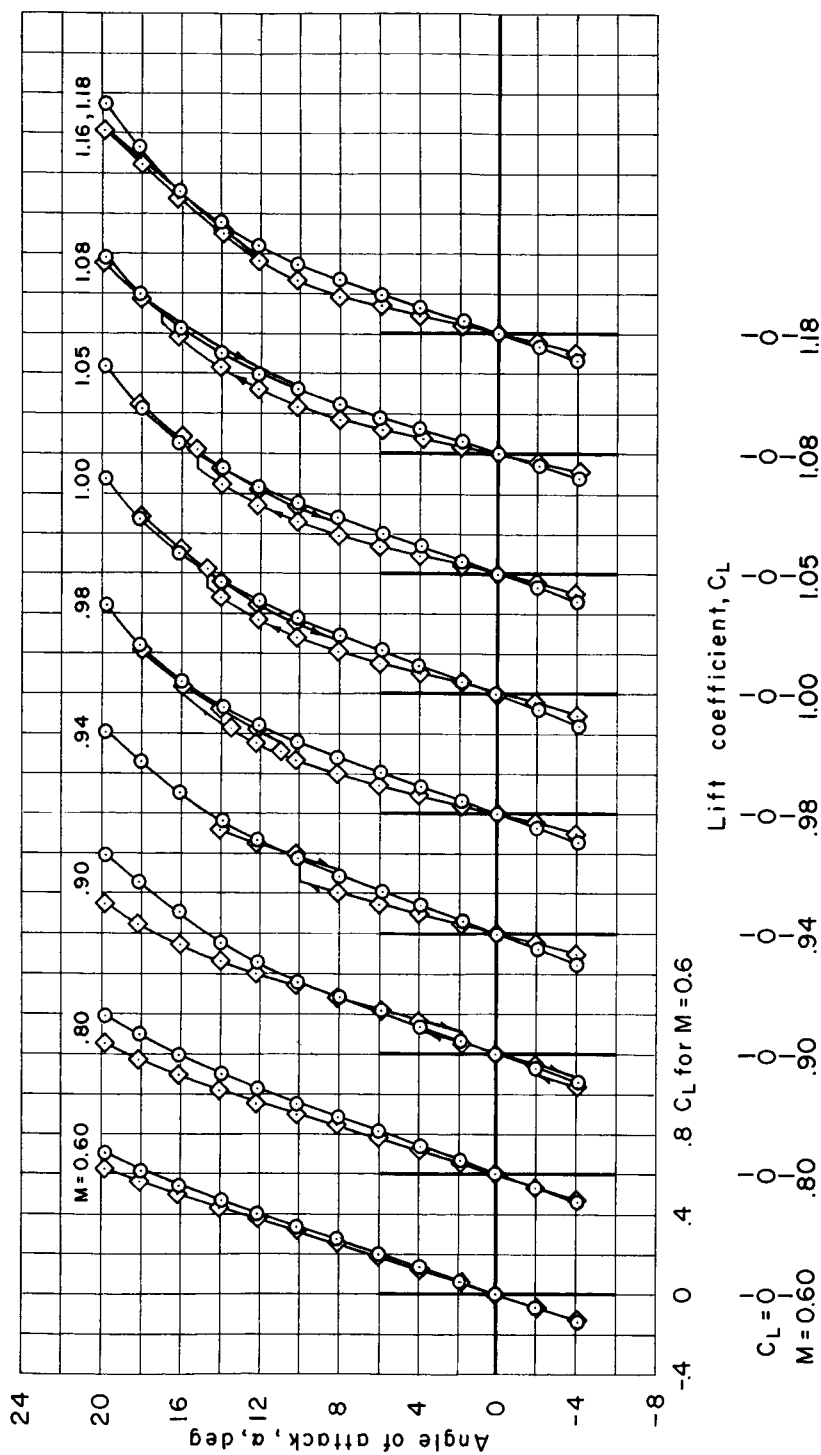
Figure 6.- Concluded.

CONFIDENTIAL



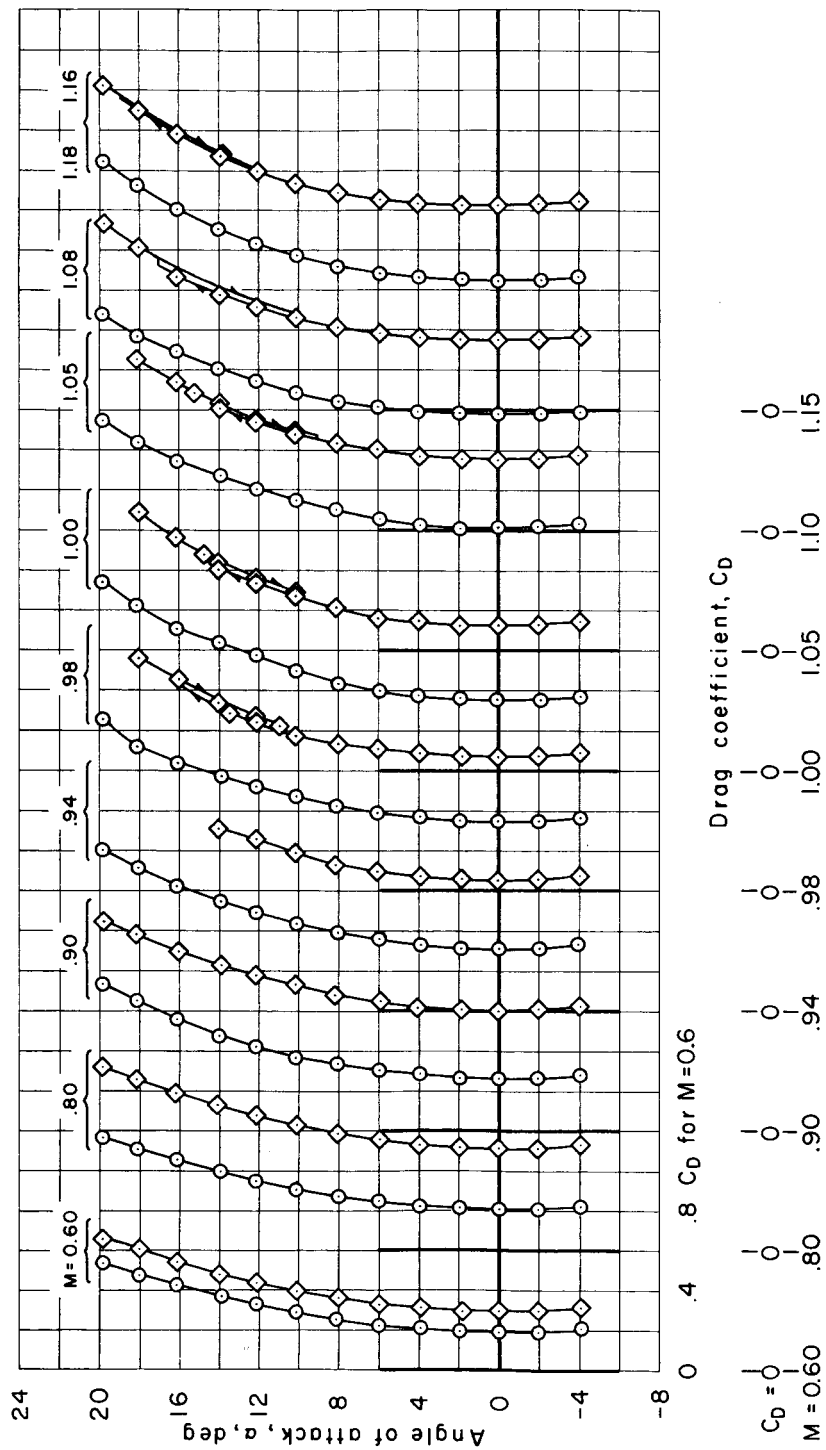
(a) Pitching-moment characteristics.

Figure 7.- The effect of nose shape on the pitching-moment, lift, and drag characteristics of the cylindrical body without the flare.



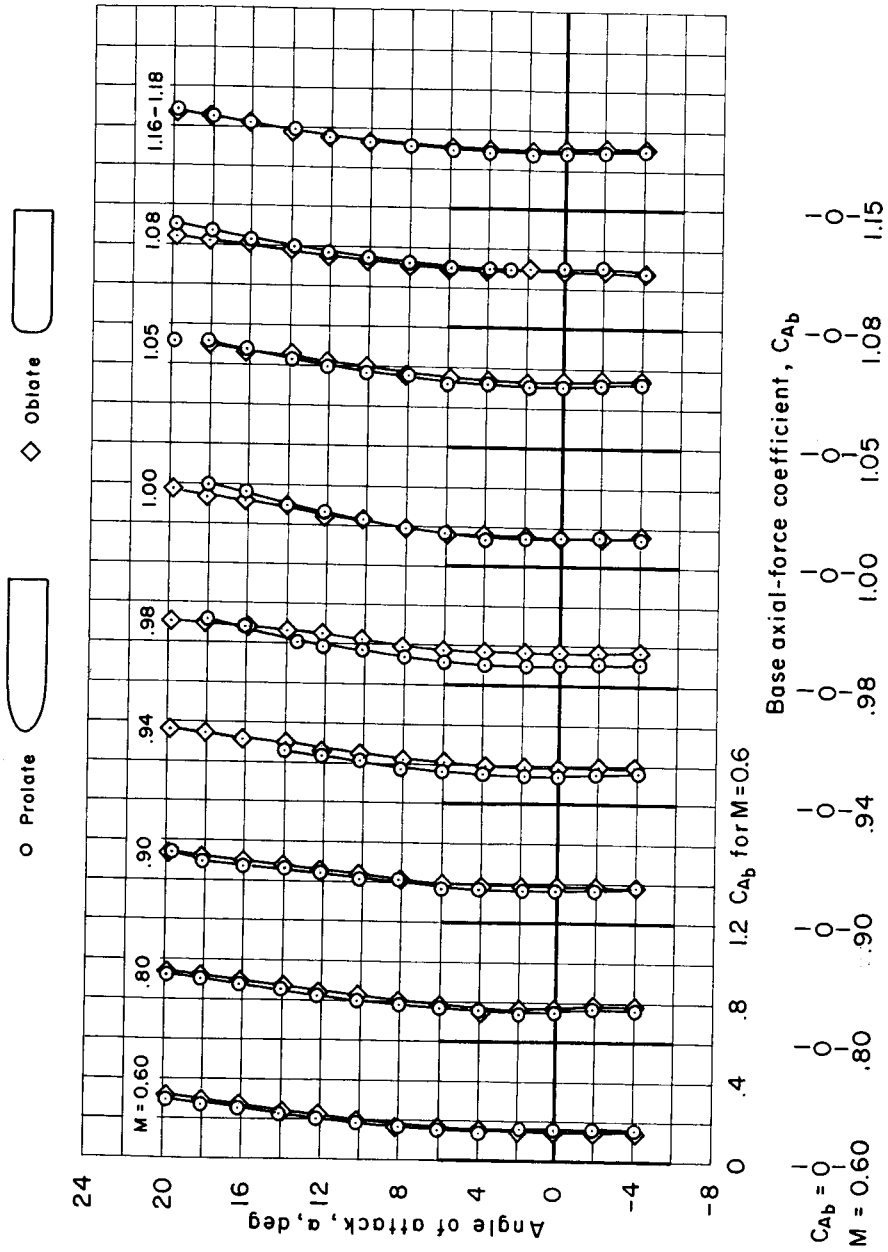
(b) Lift characteristics.

Figure 7.- Continued.



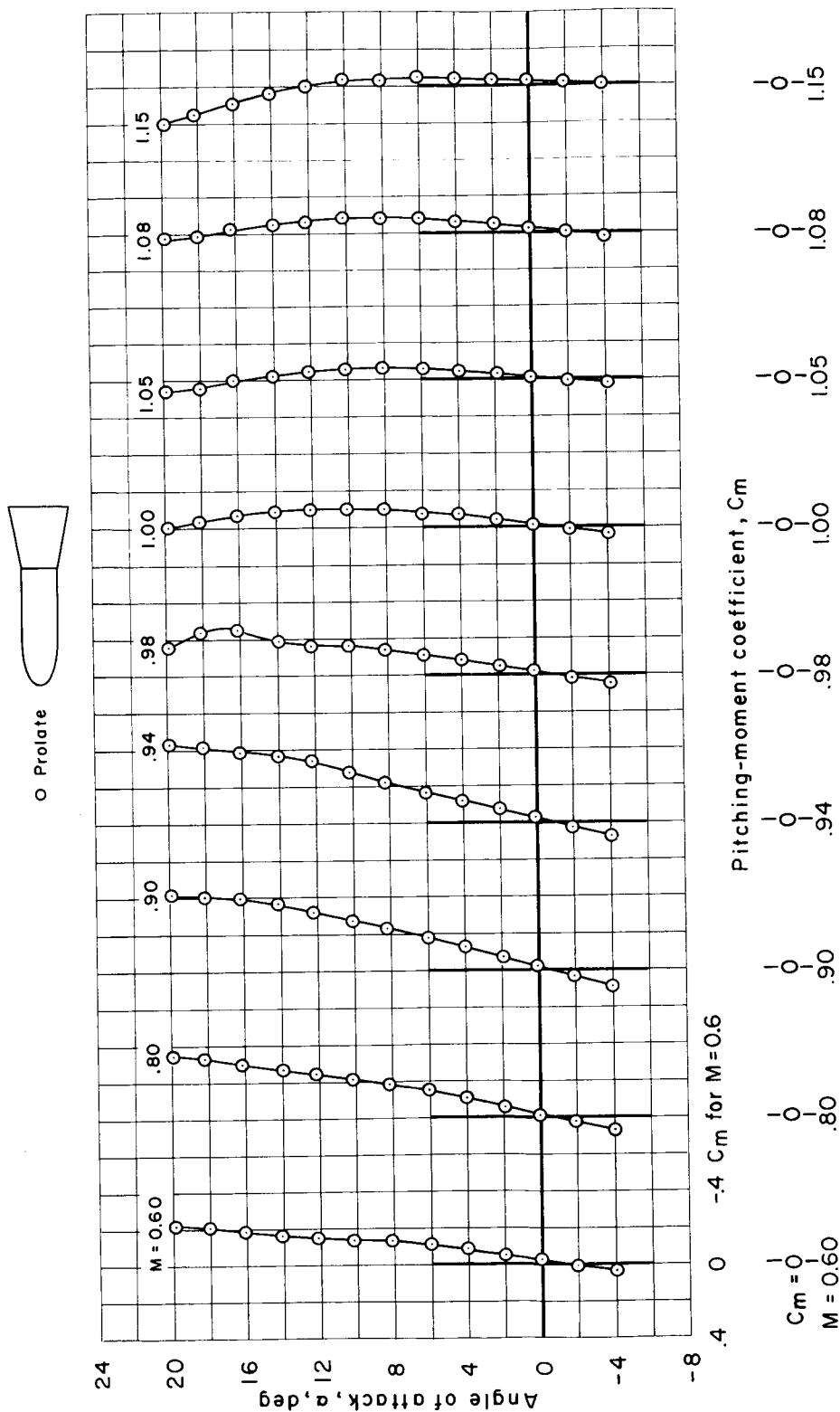
(c) Total-drag characteristics.

Figure 7.- Continued.



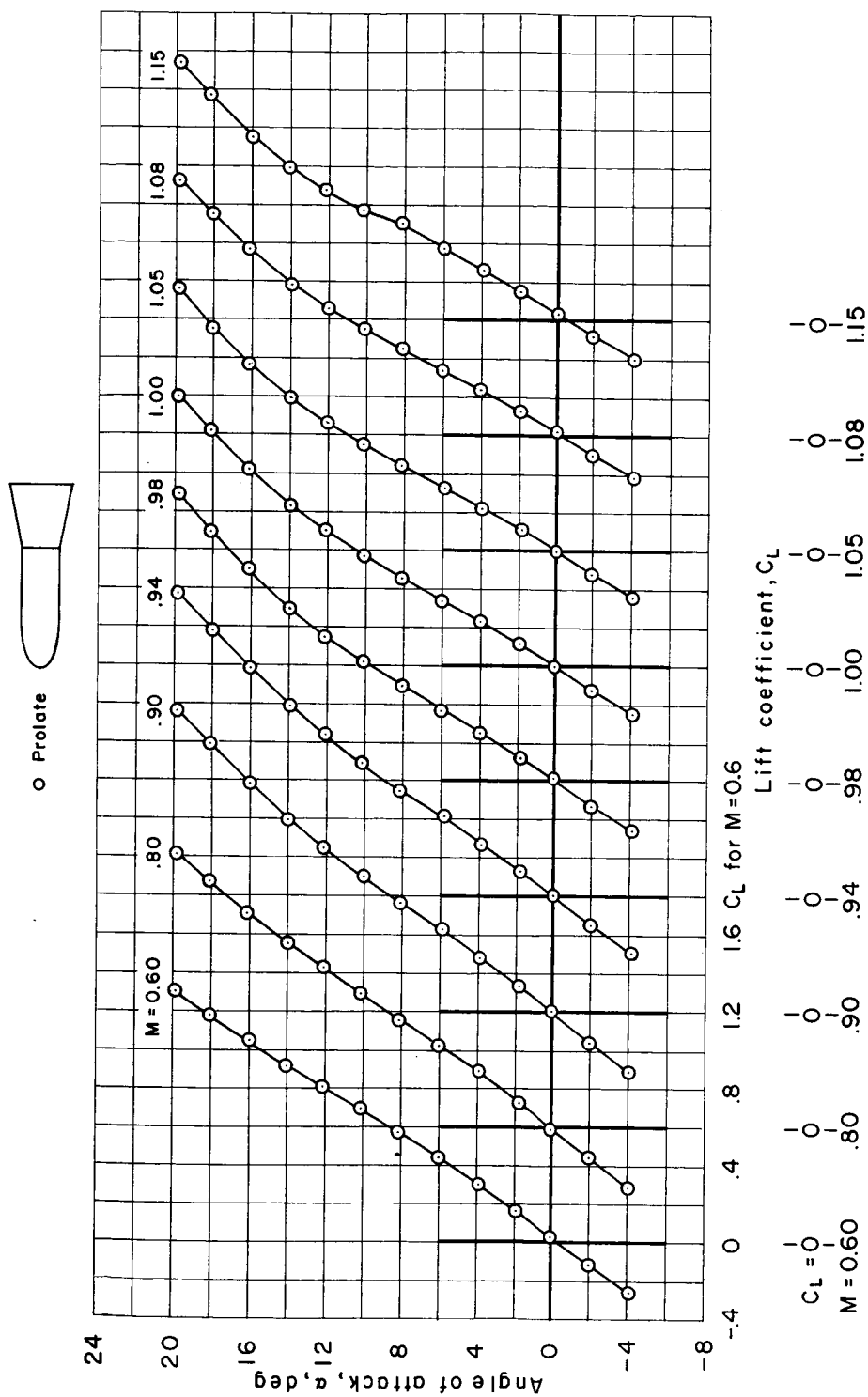
(d) Base axial-force characteristics.

Figure 7.- Concluded.



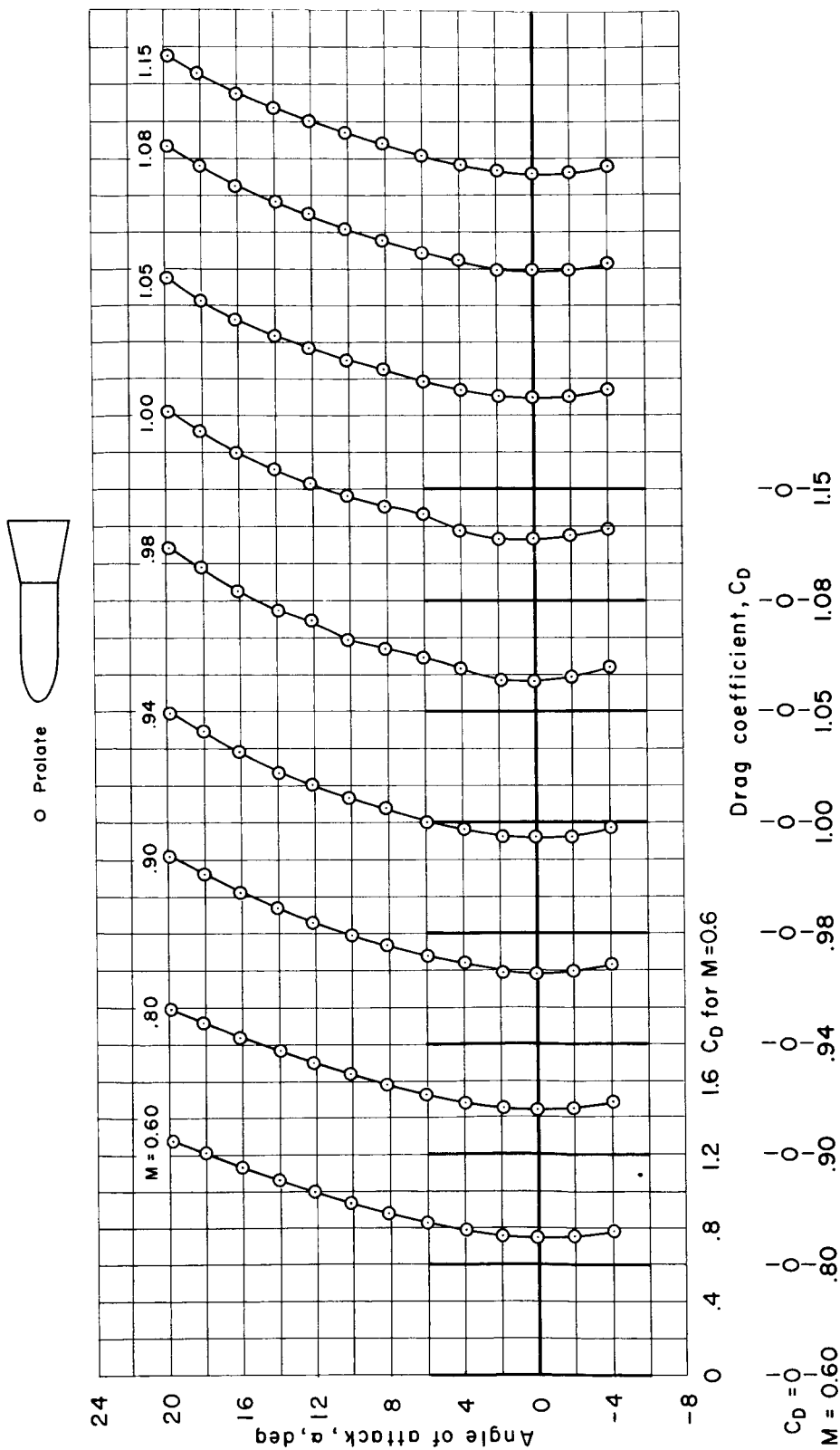
(a) Pitching-moment characteristics.

Figure 8.- The pitching-moment, lift, and drag characteristics of the cylindrical body with the prolate nose and extended flare.



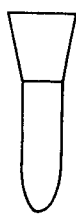
(b) Lift characteristics.

Figure 8.- Continued.



(c) Total-drag characteristics.

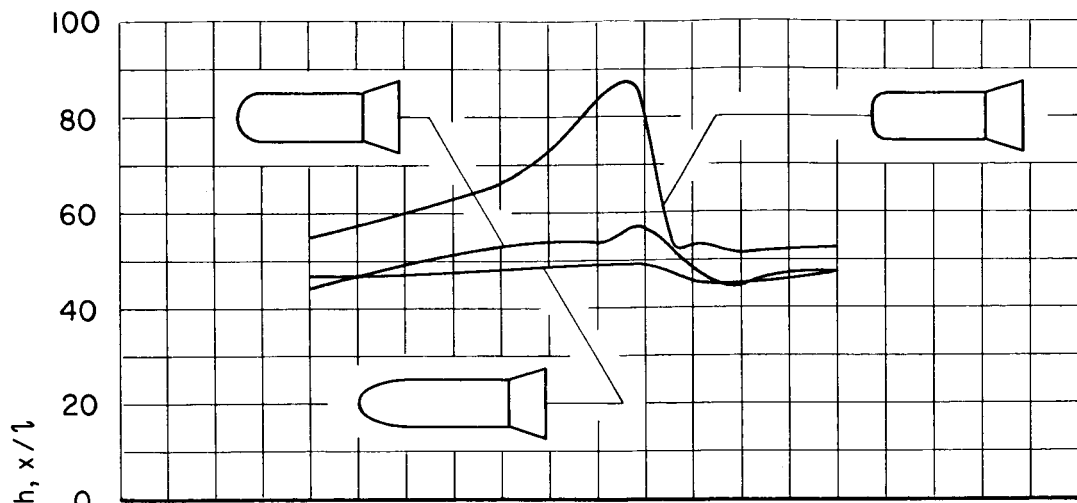
Figure 8.- Continued.



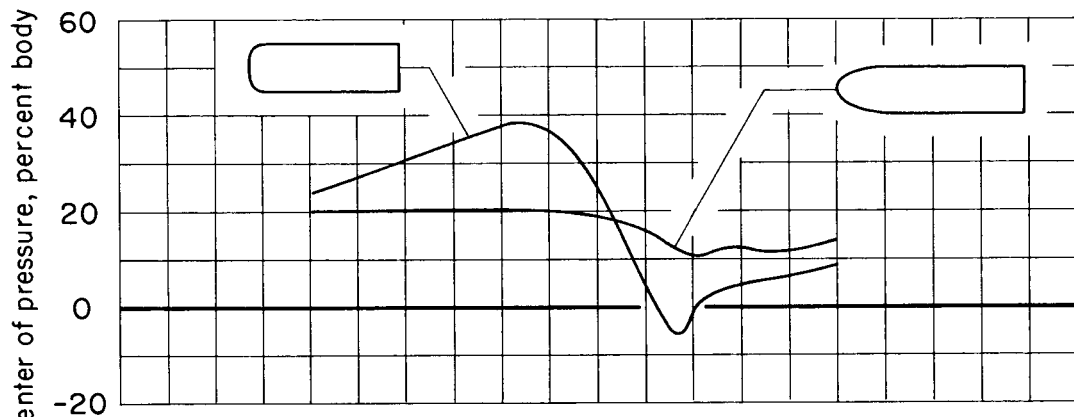
(d) Base axial-force characteristics.

Figure 8.- Concluded.

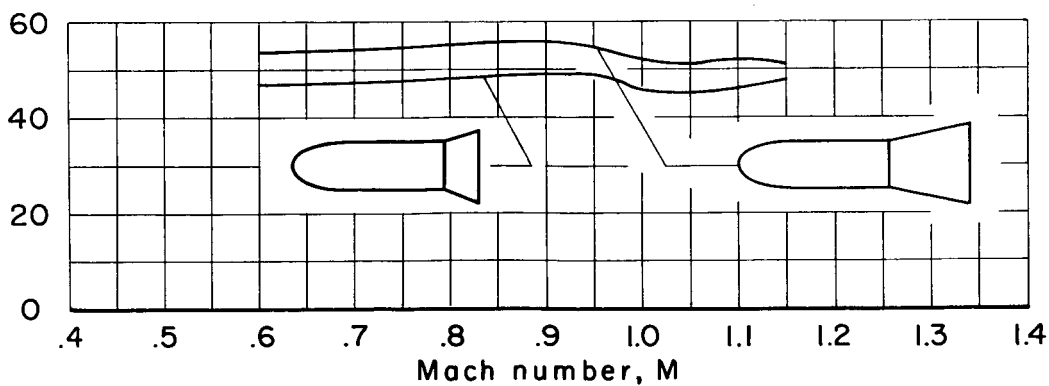
~~CONFIDENTIAL~~



(a) Effect of nose shape. Model with standard flare.

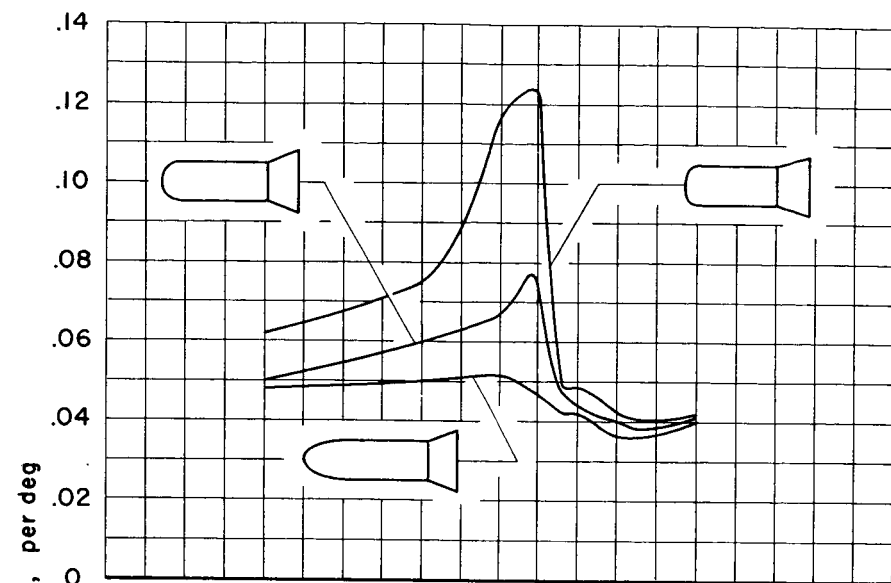


(b) Effect of nose shape. Model without flare.

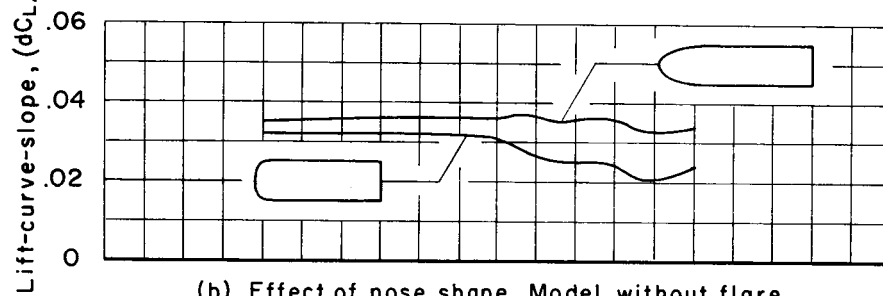


(c) Effect of changing the flare. Model with prolate nose.

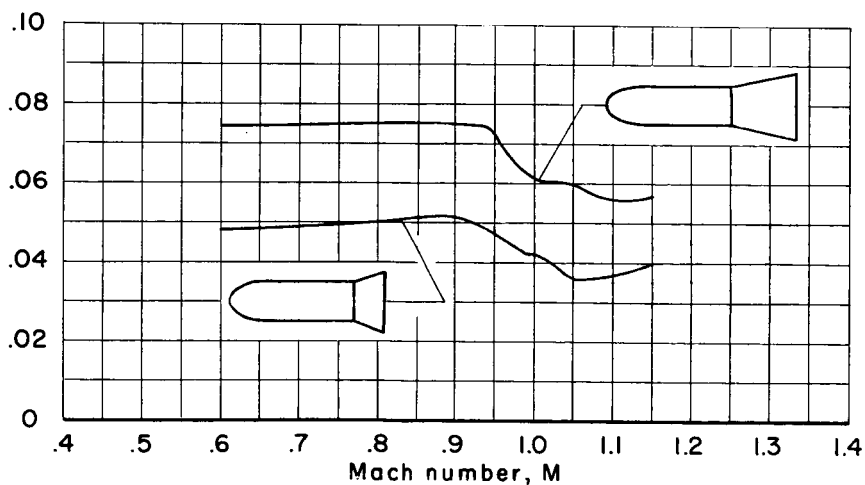
Figure 9.- Center of pressure of cylinder-flare models for an angle of attack of 0° .



(a) Effect of nose shape. Model with standard flare.



(b) Effect of nose shape. Model without flare.



(c) Effect of changing the flare. Model with prolate nose.

Figure 10.- Lift-curve slope of cylinder-flare models for an angle of attack of 0° .

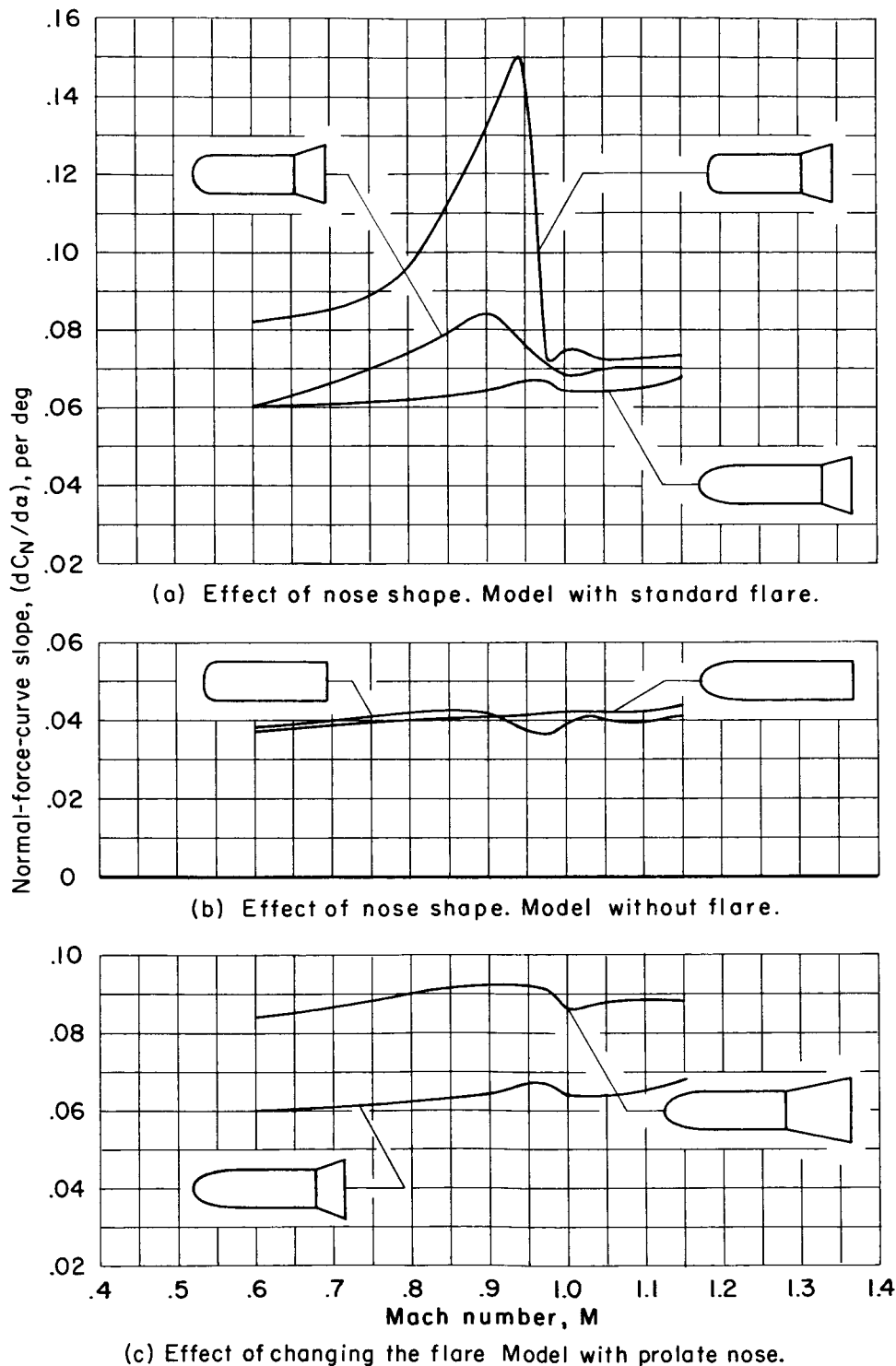


Figure 11.- Normal-force-curve slope of cylinder-flare models for an angle of attack of 0° .

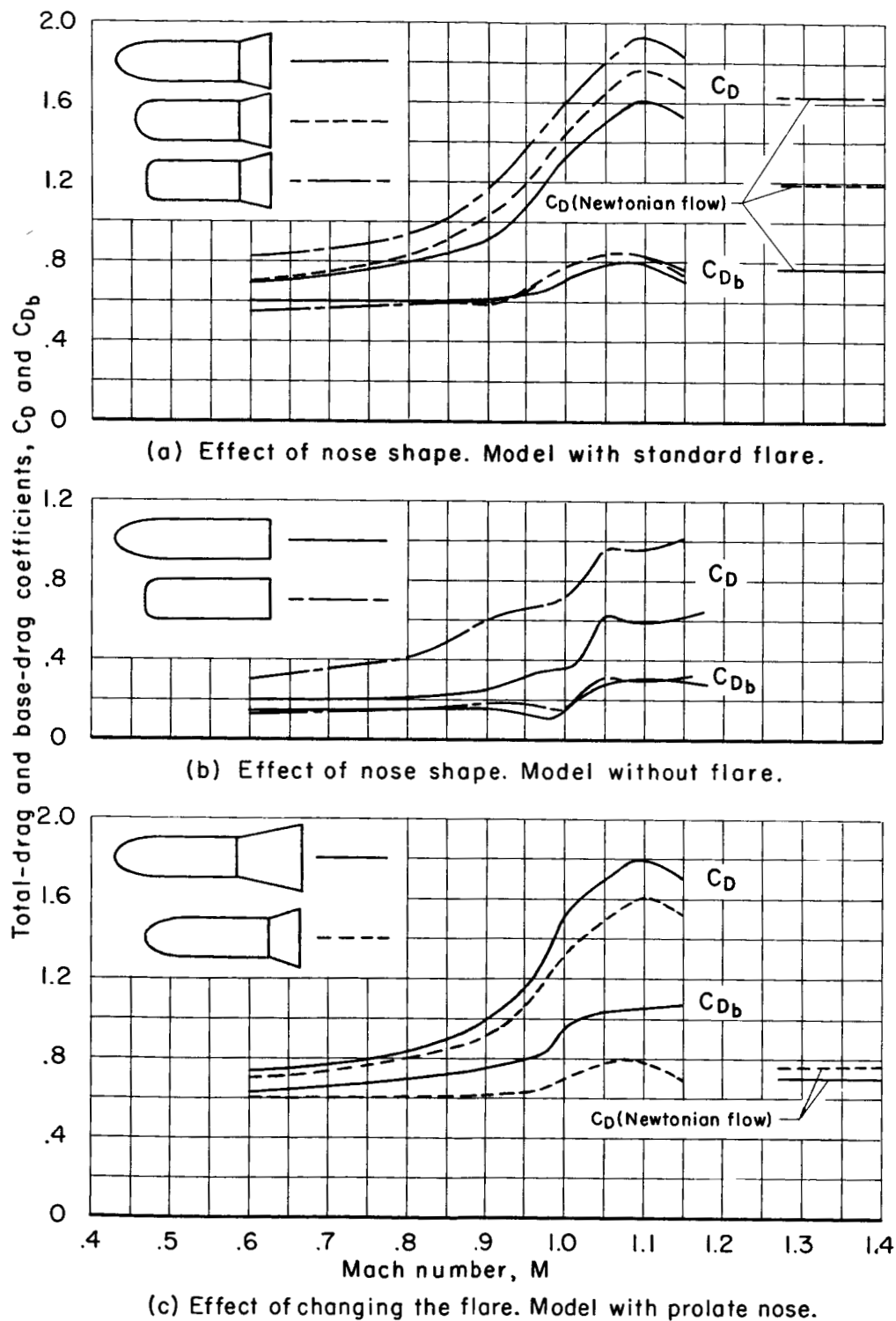


Figure 12.- Drag coefficient of cylinder-flare models for an angle of attack of 0° .

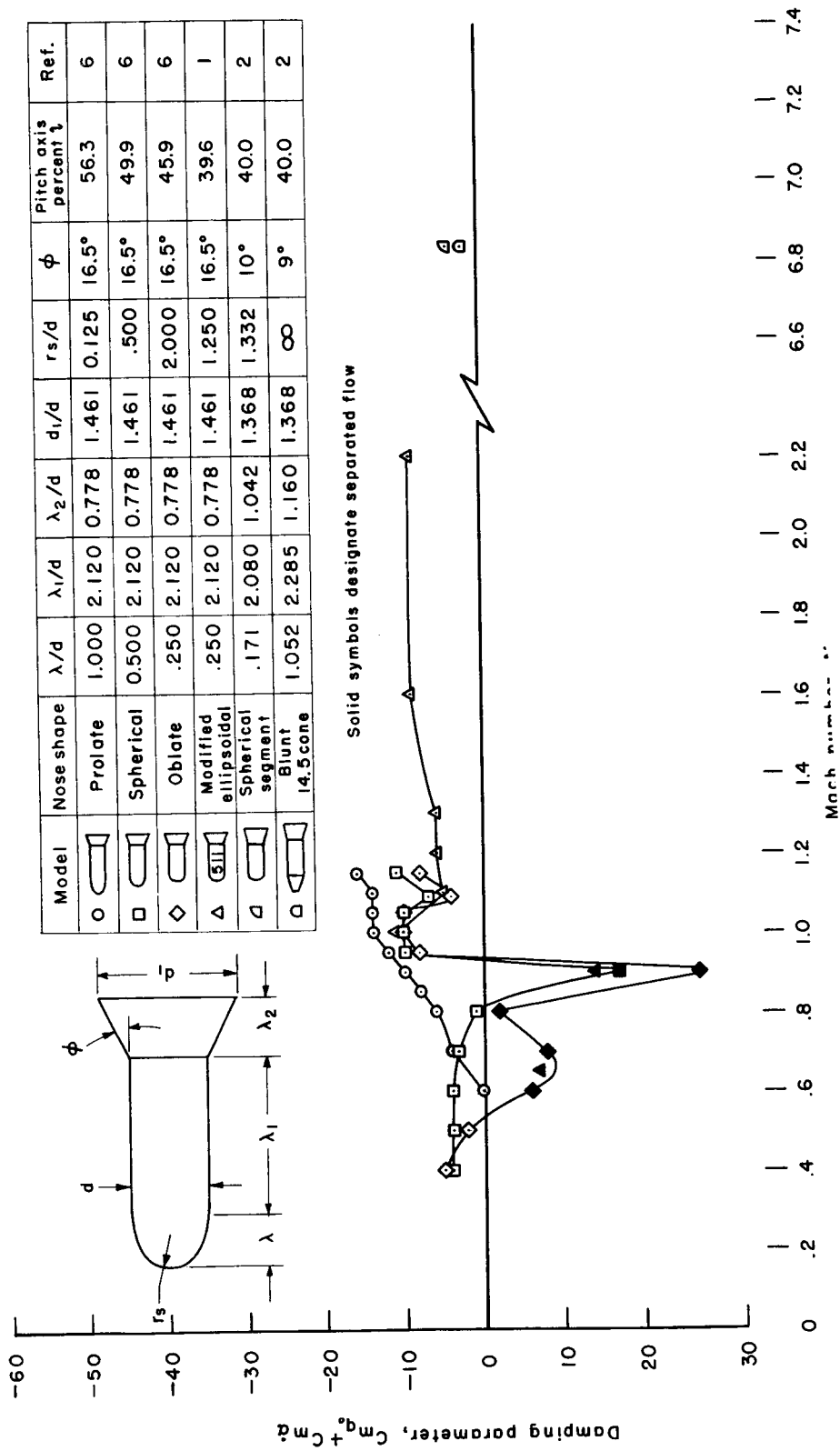


Figure 13.- Dynamic stability characteristics of cylinder-flare models.

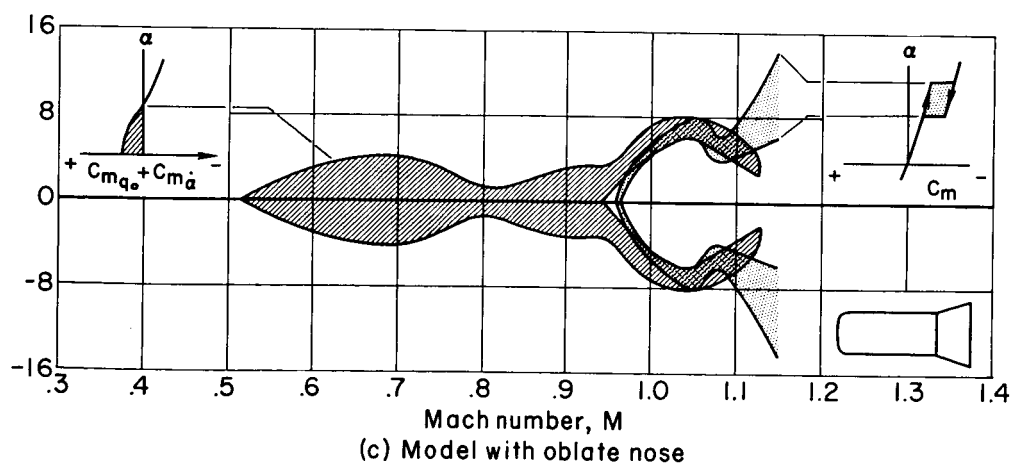
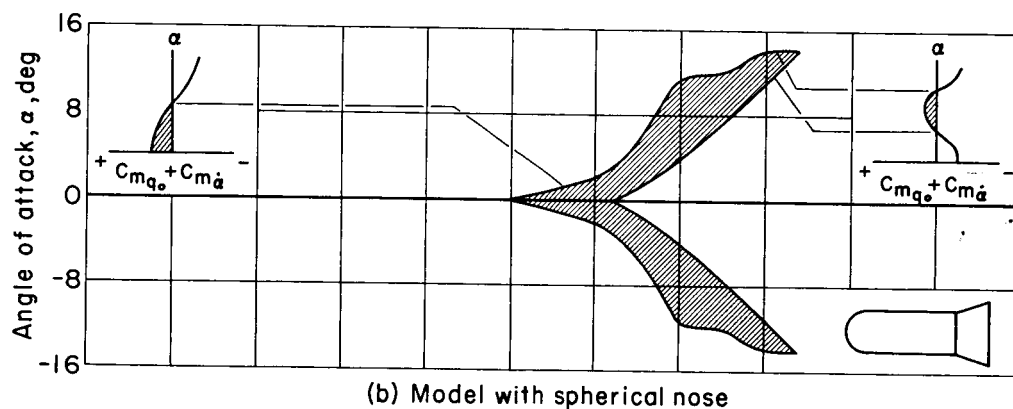
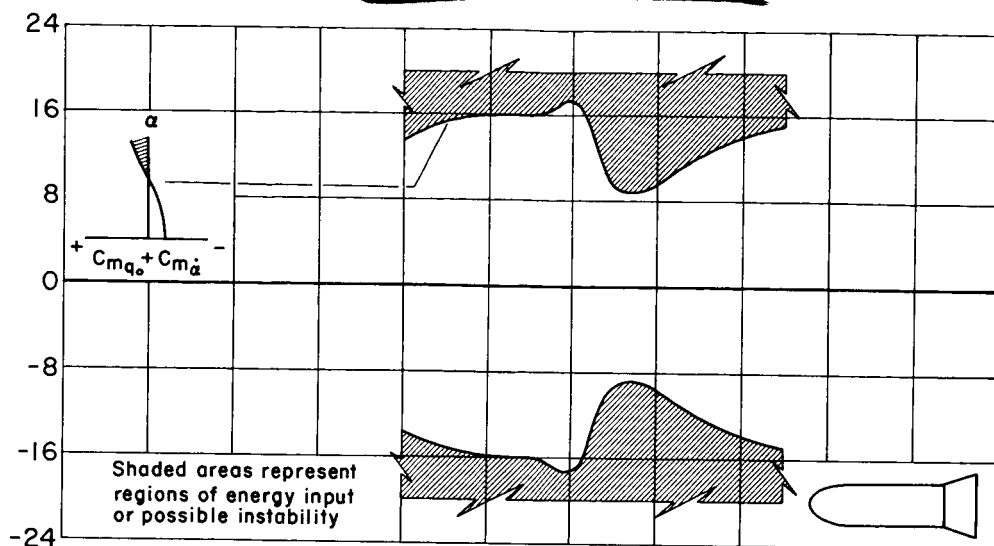
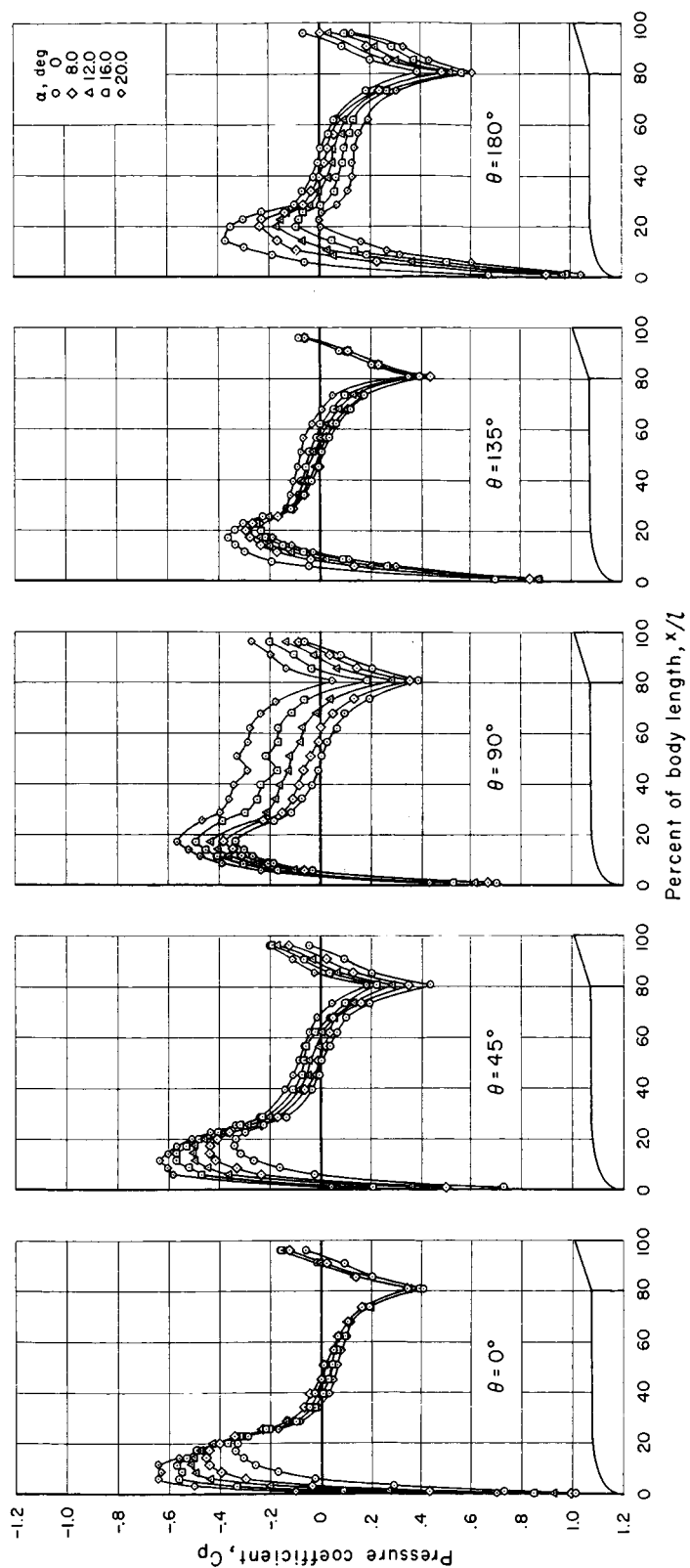


Figure 14.- Angle-of-attack regions for energy input to the missile system oscillating in one degree of freedom.

[REDACTED]

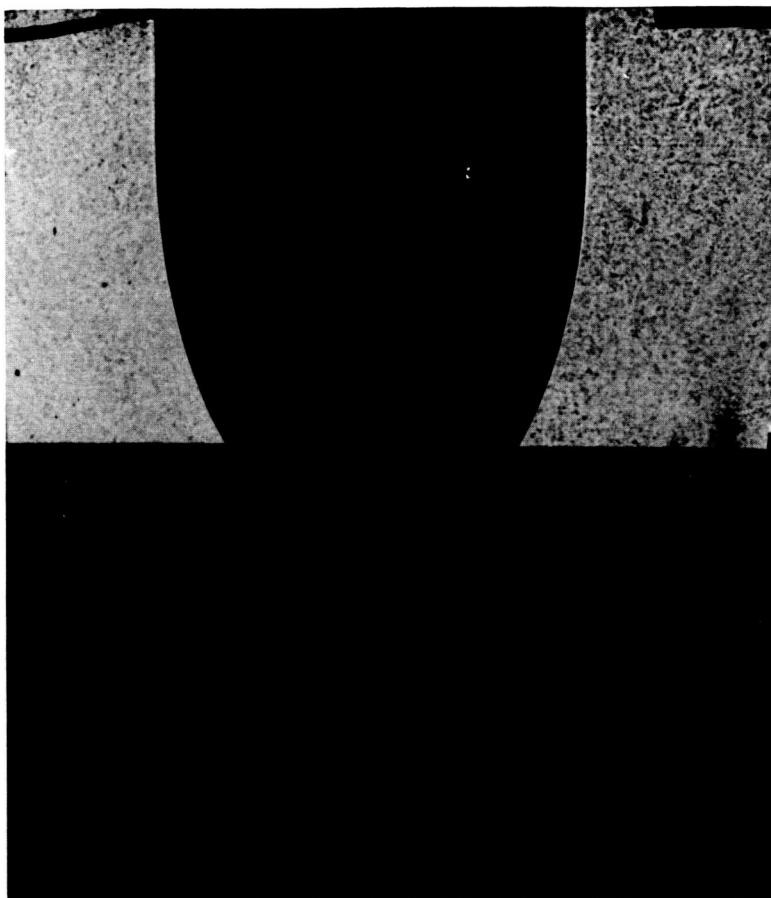
A
2
5
6

[REDACTED]



(a) Pressure distribution, $M = 0.40$.

Figure 15.- Pressure distribution and shadowgraph of the flow of the prolate-nosed model with the standard flare.



$$\alpha = 0^\circ$$

(b) Shadowgraph, $M = 0.60$.

Figure 15.- Continued.

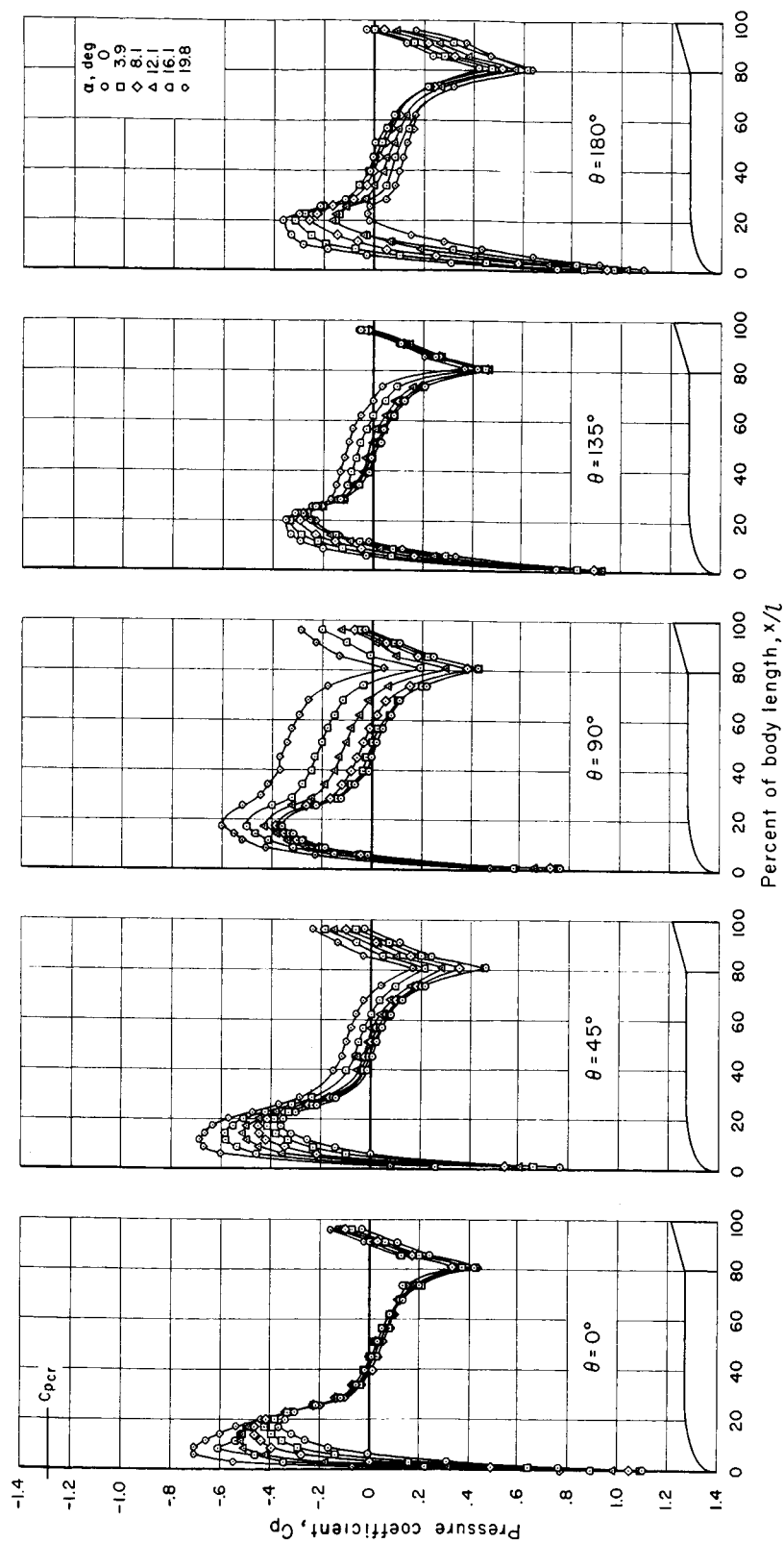
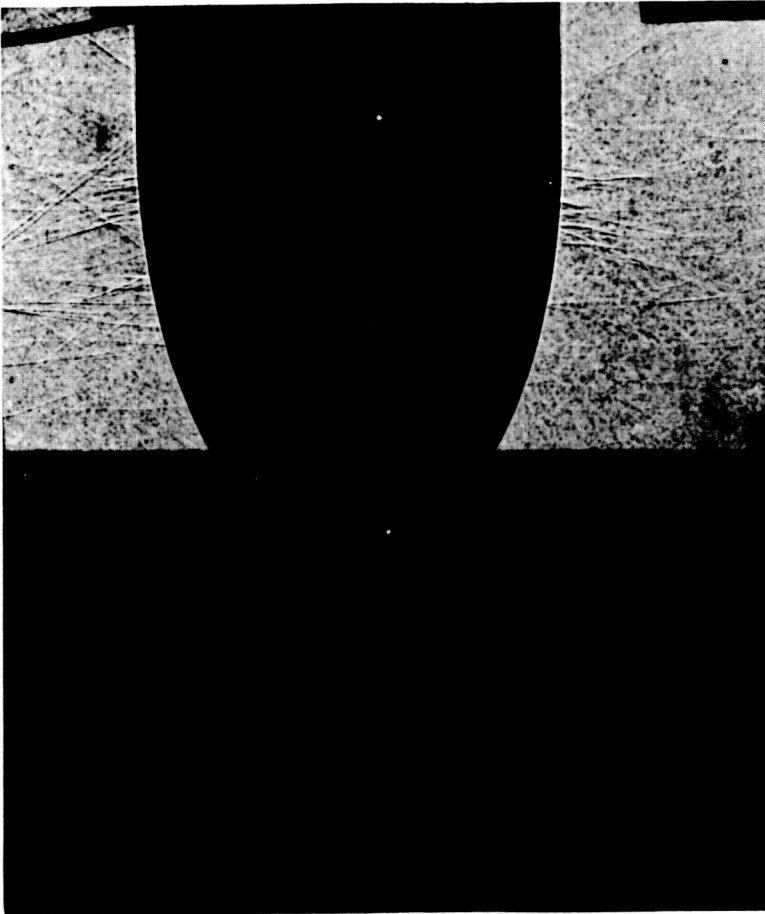
(c) Pressure distribution, $M = 0.60$.

Figure 15.- Continued.

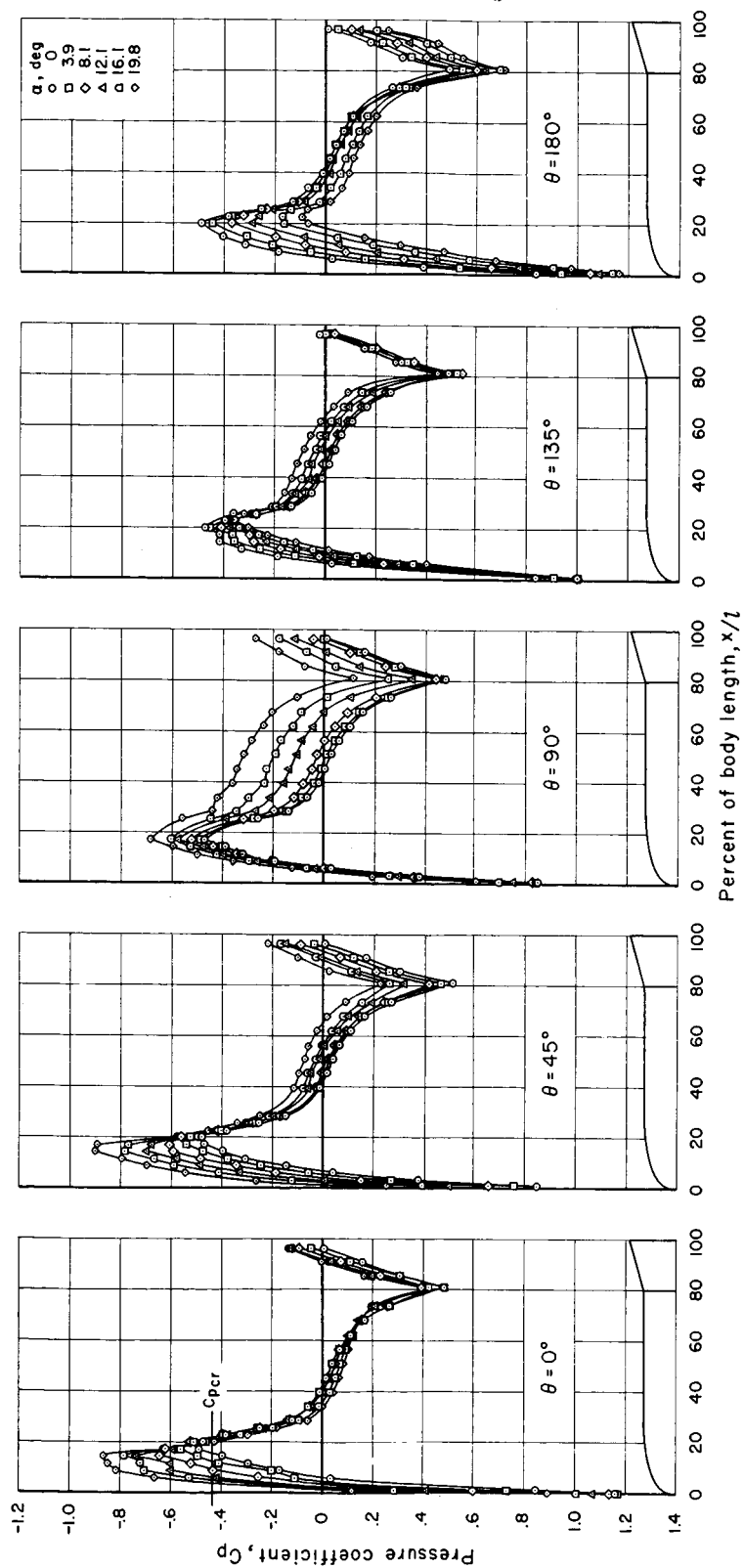
~~CONFIDENTIAL~~

$$\alpha = 0^\circ$$

(a) Shadowgraph, $M = 0.80$.

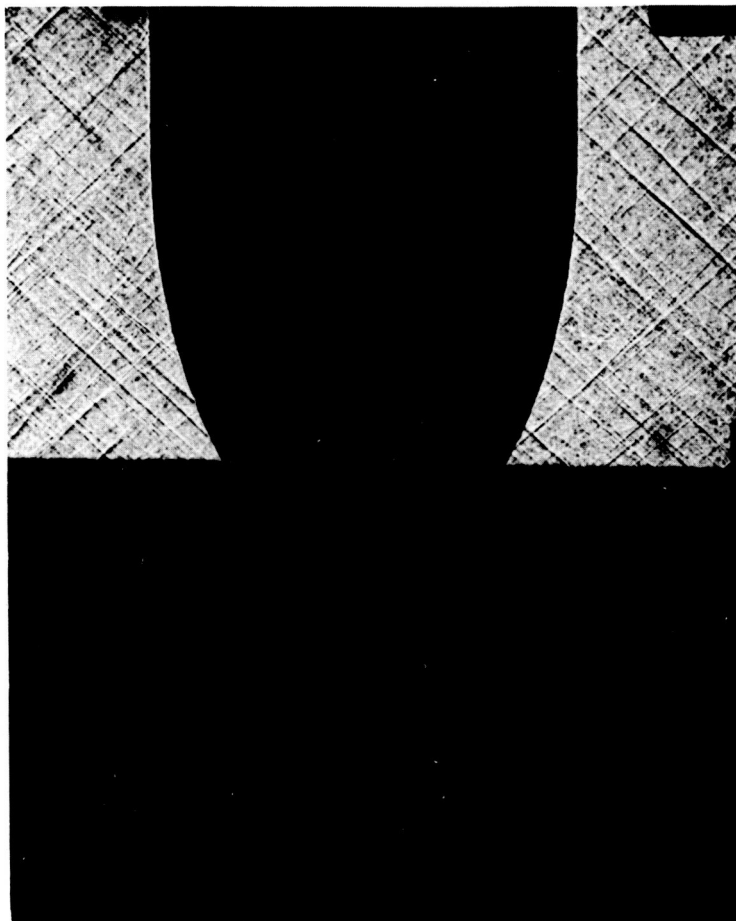
Figure 15.- Continued.

A
2
9
6~~CONFIDENTIAL~~



(e) Pressure distribution, $M = 0.80$.

Figure 15.- Continued.

~~CONFIDENTIAL~~

$$\alpha = 0^\circ$$

(f) Shadowgraph, $M = 1.05$.

Figure 15.- Continued.

~~CONFIDENTIAL~~

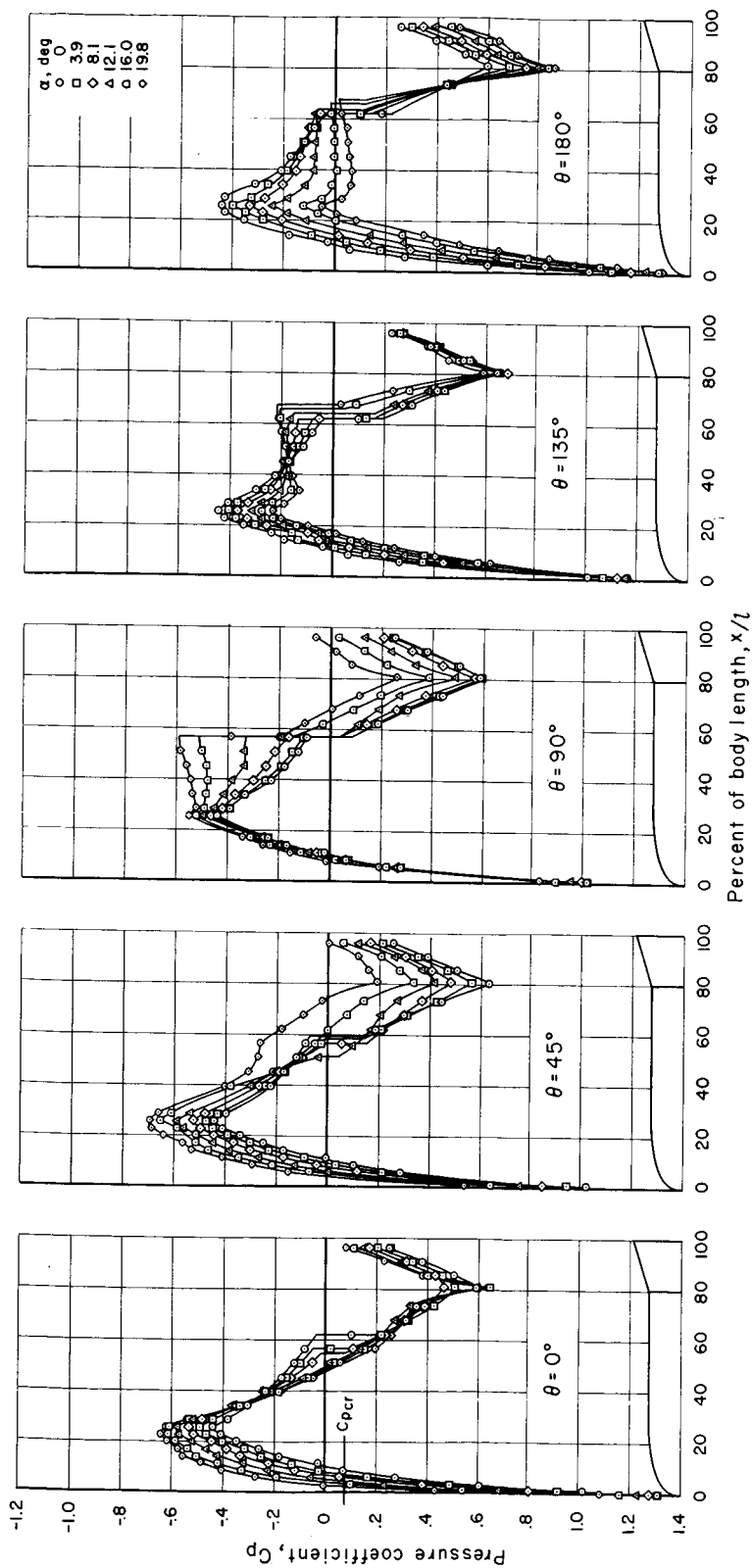
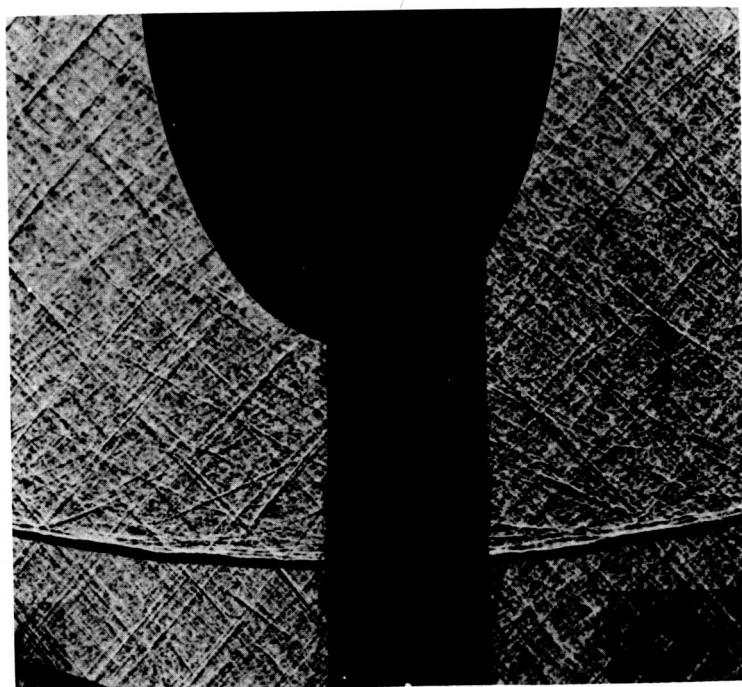
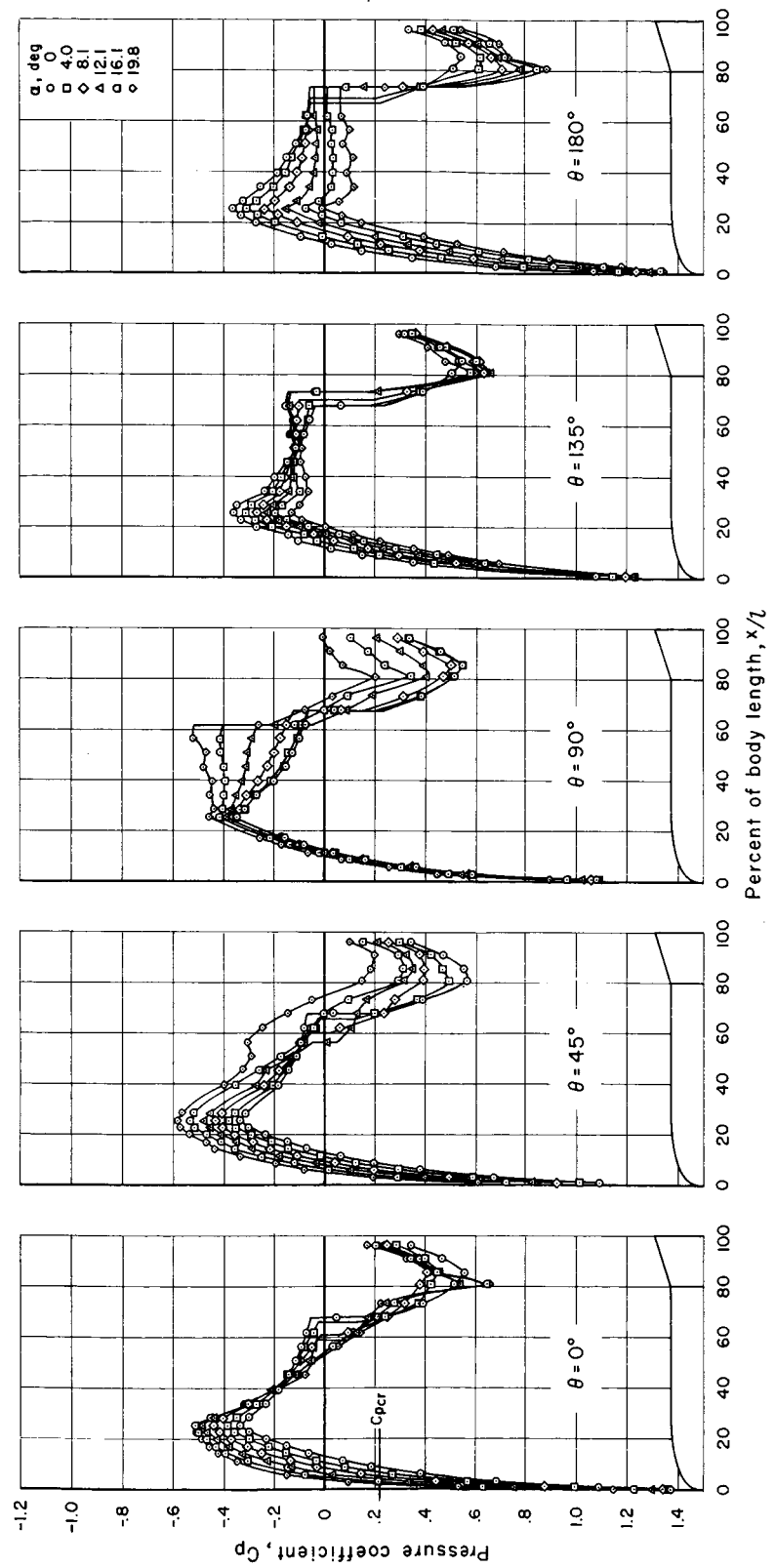
(g) Pressure distribution, $M = 1.05$.

Figure 15.- Continued.



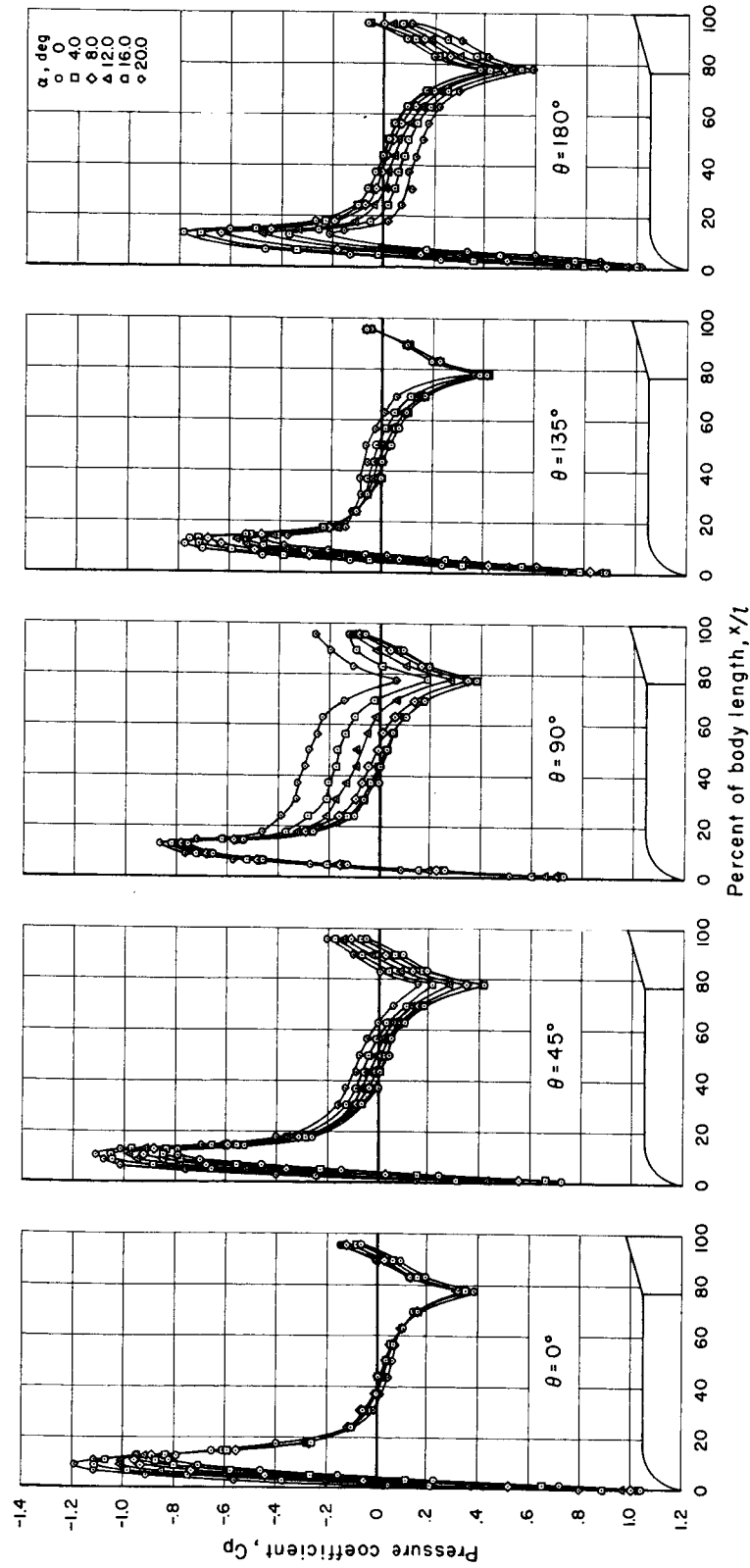
$\alpha = 0^\circ$
(h) Shadowgraph, $M = 1.15$.

Figure 15.- Continued.



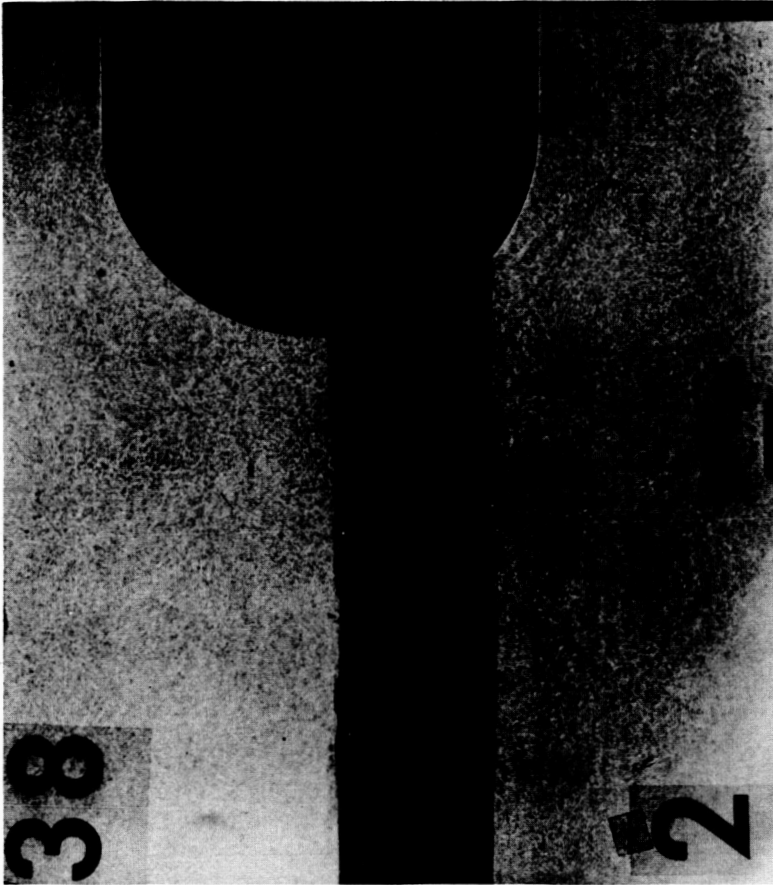
(i) Pressure distribution, $M = 1.15$.

Figure 15.- Concluded.



(a) Pressure distribution, $M = 0.40$.

Figure 16.- Pressure distribution and shadowgraph of the flow of the spherical-nosed model with the standard flare.

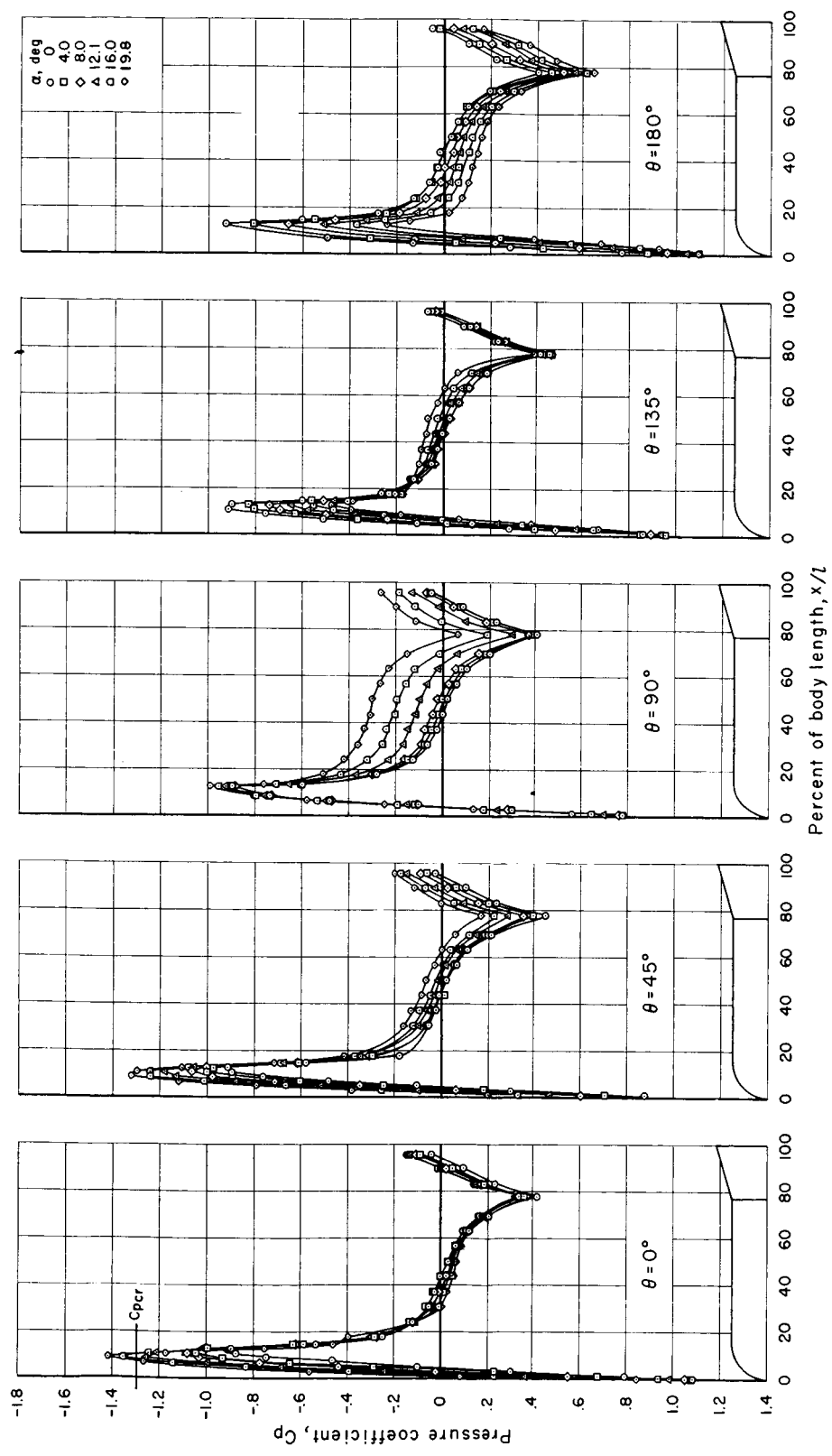
~~CONFIDENTIAL~~

$$\alpha = 0^\circ$$

(b) Shadowgraph, $M = 0.60$.

Figure 16.- Continued.

~~CONFIDENTIAL~~



(c) Pressure distribution, $M = 0.60$.

Figure 16.- Continued.

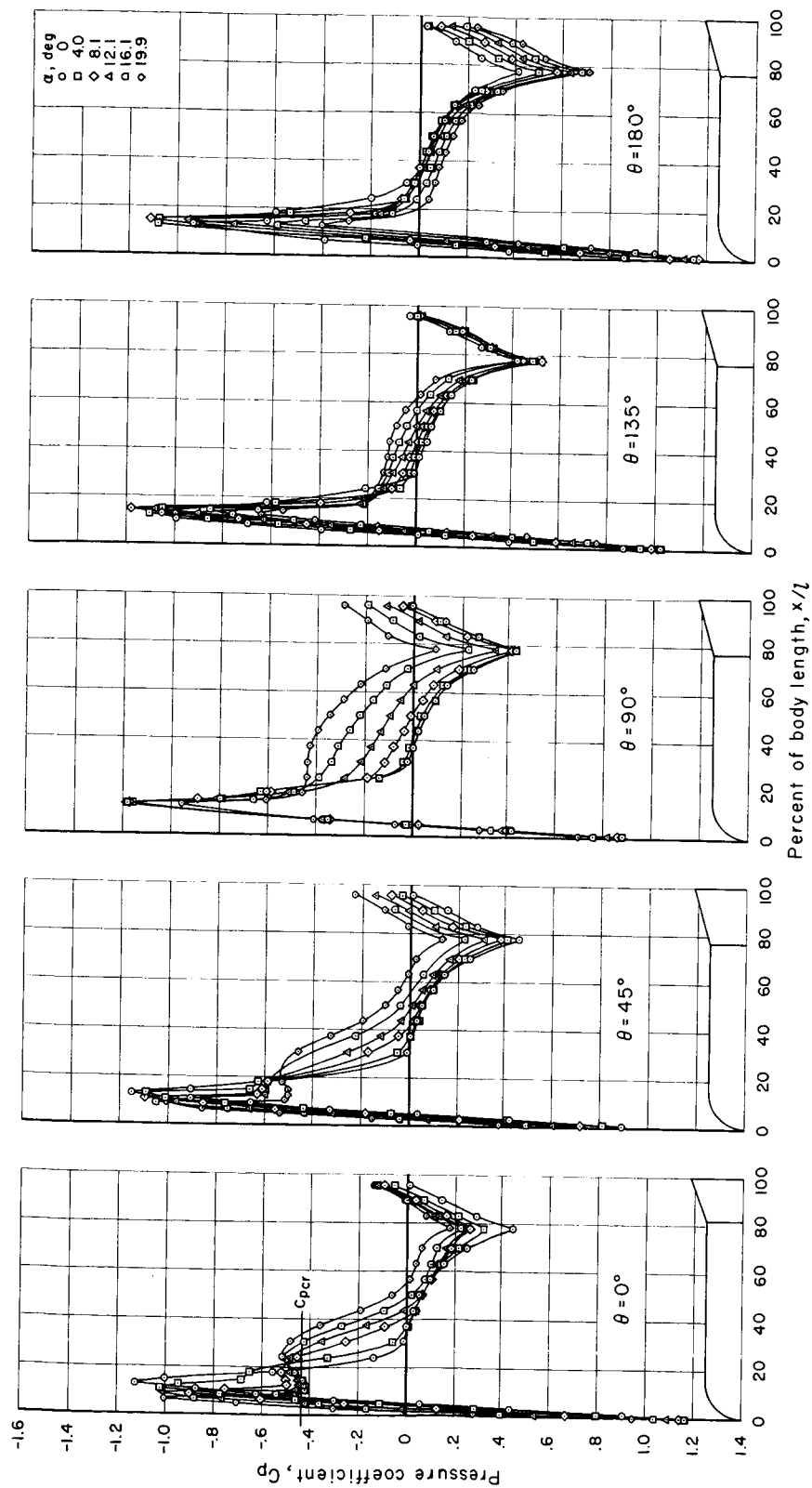
~~CONFIDENTIAL~~

$$\alpha = 0^\circ$$

(d) Shadowgraph, $M = 0.80$.

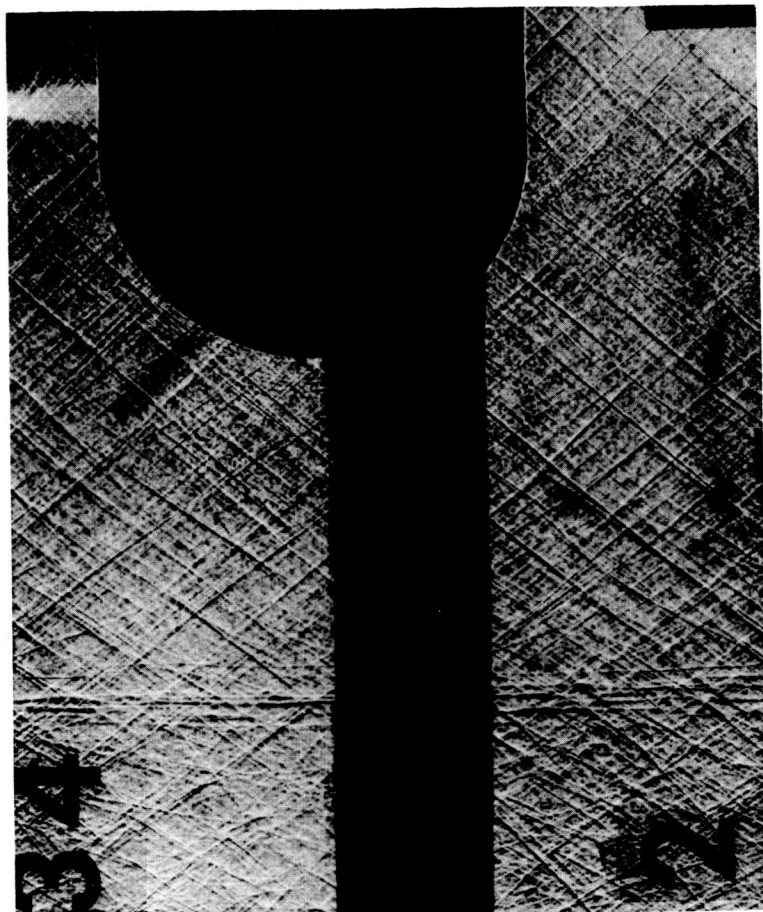
Figure 16.- Continued.

~~CONFIDENTIAL~~



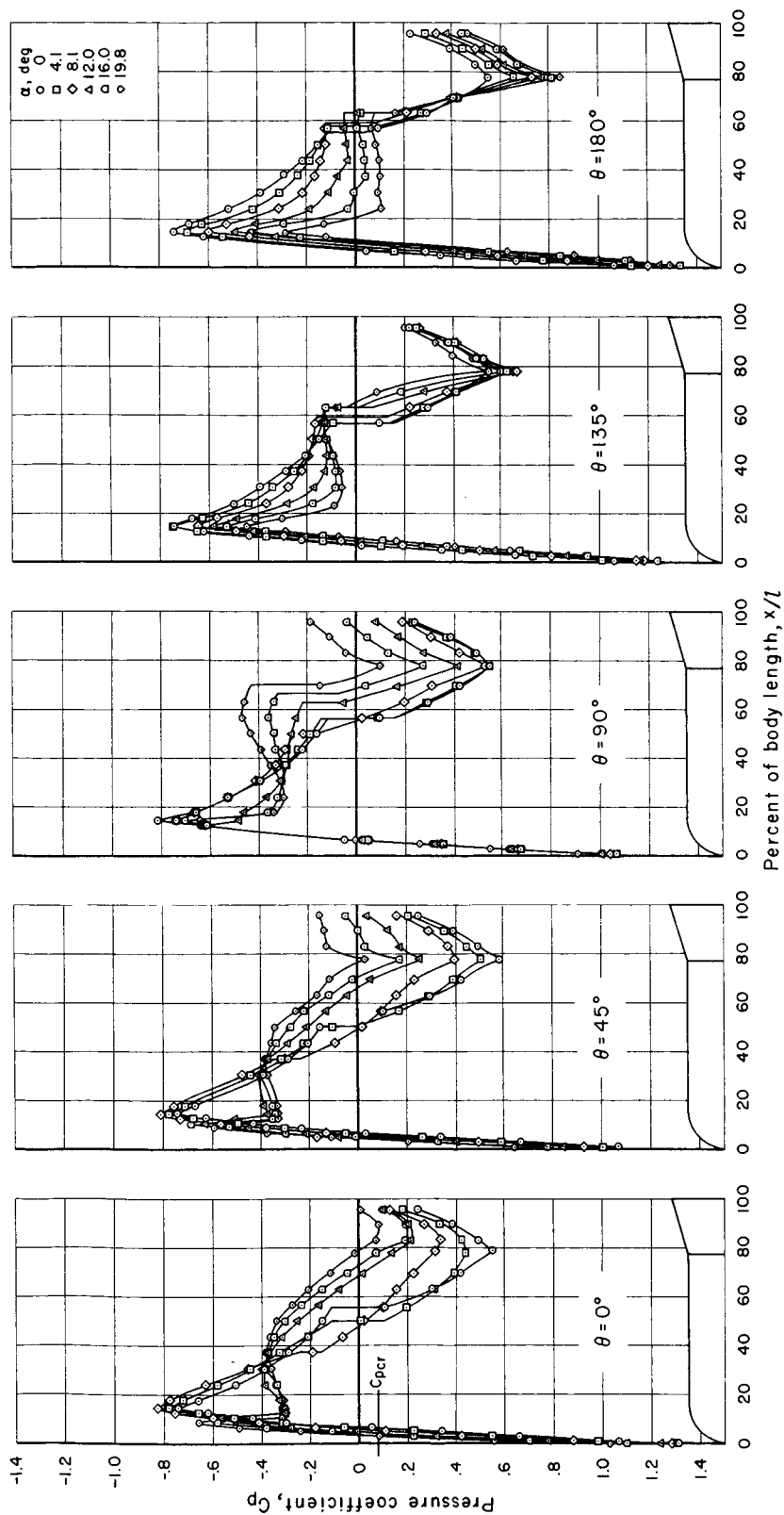
(e) Pressure distribution, $M = 0.80$.

Figure 16.- Continued.



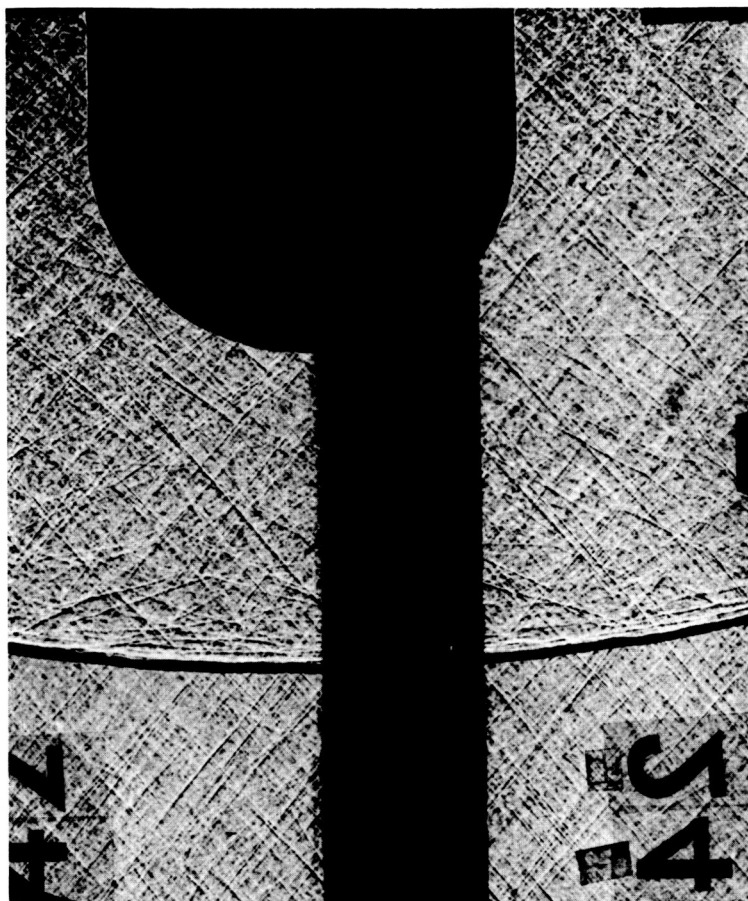
$\alpha = 0^\circ$
(f) Shadowgraph, $M = 1.05$.

Figure 16.- Continued.



(g) Pressure distribution, $M = 1.05$.

Figure 16.- Continued.



$$\alpha = 0^\circ$$

(h) Shadowgraph, $M = 1.15$.

Figure 16.- Continued.

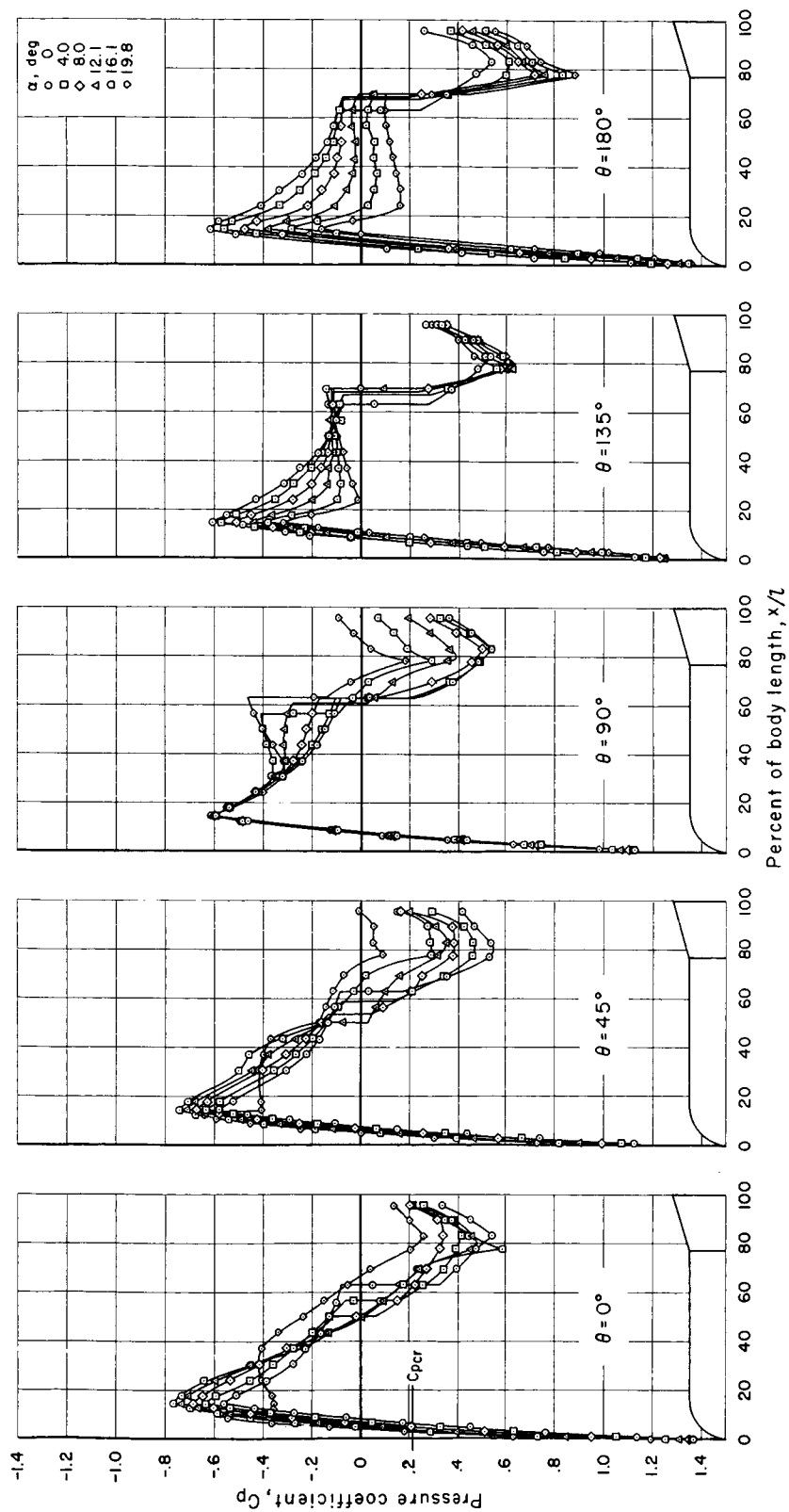
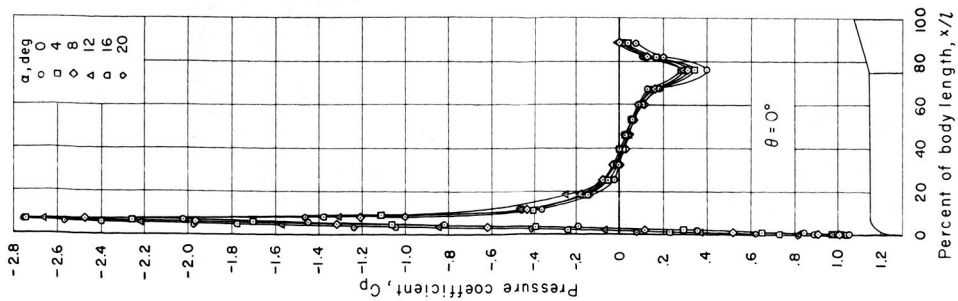
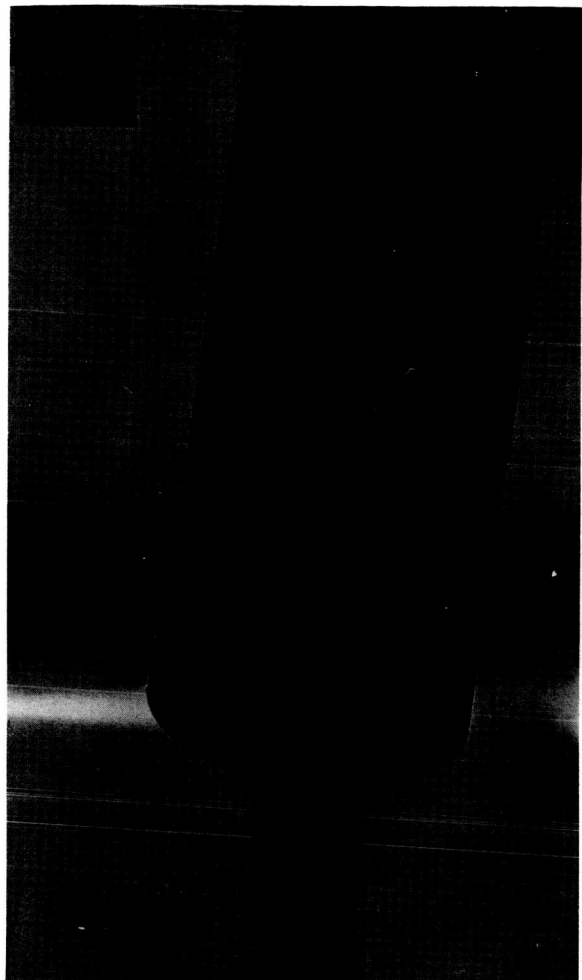
(i) Pressure distribution, $M = 1.15$.

Figure 16.- Concluded.

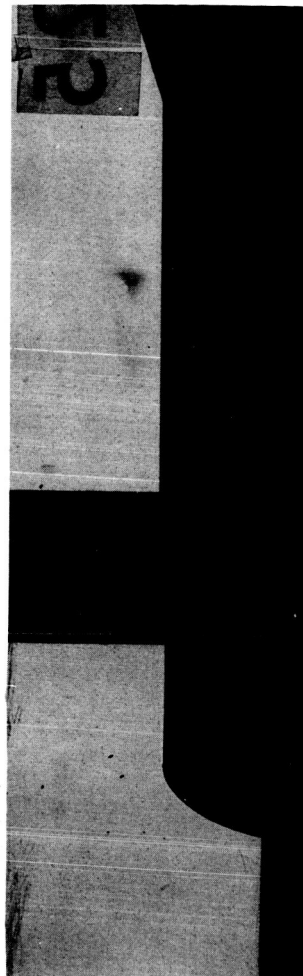
~~CONFIDENTIAL~~A
2
9
6~~CONFIDENTIAL~~



(a) $M = 0.40$.

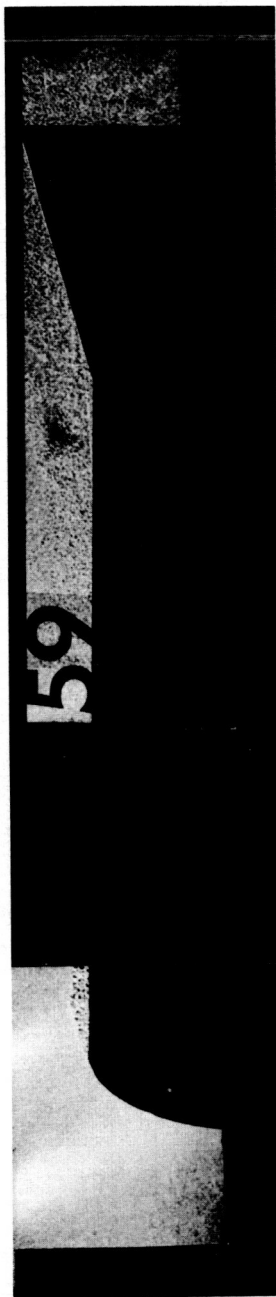


$\alpha = 8^\circ$



$\alpha = 0^\circ$

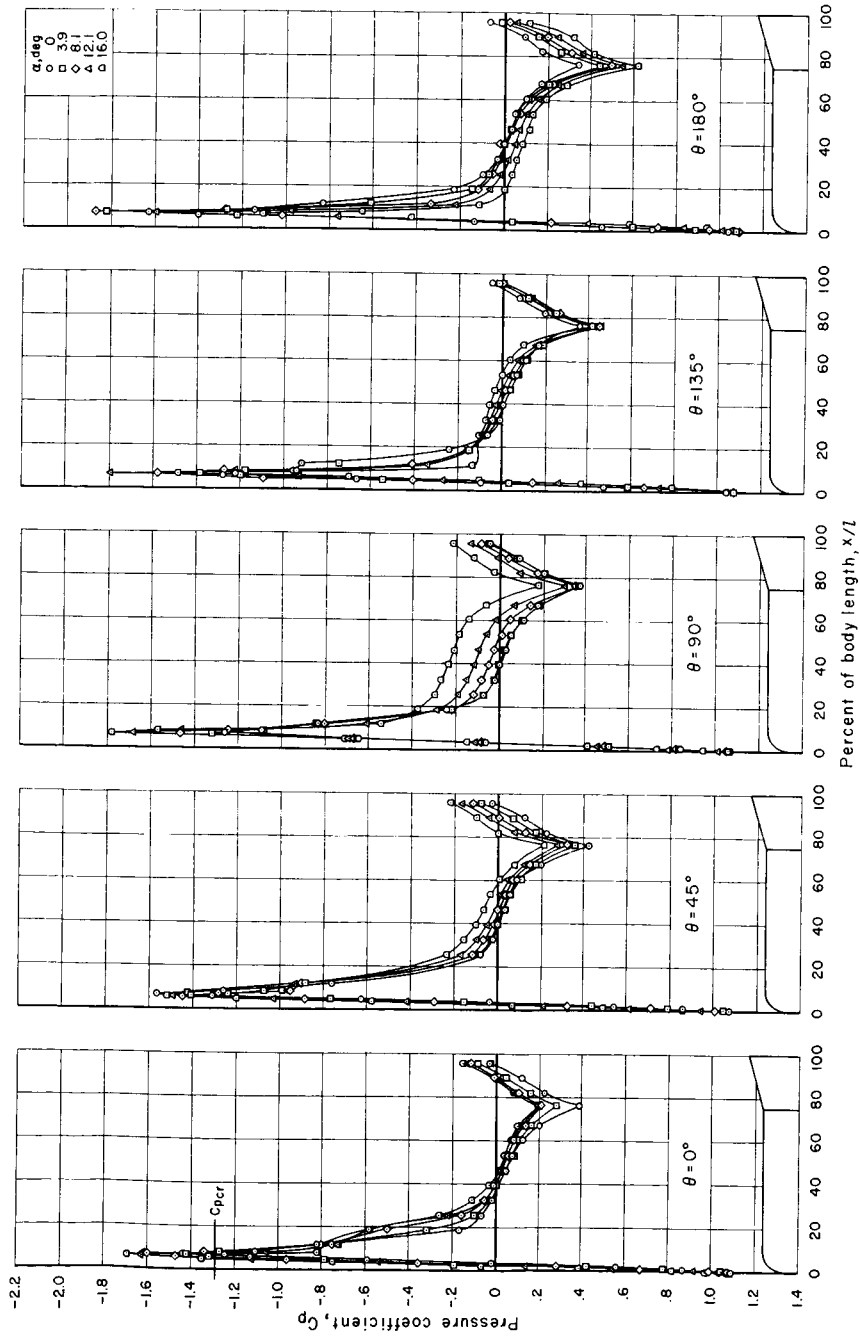
Figure 17.- Pressure distribution and shadowgraph of the flow of the oblate-nosed model with the standard flare.

~~CONFIDENTIAL~~ $\alpha = 8^\circ$  $\alpha = 0^\circ$

(b) Shadowgraph, $M = 0.60$.

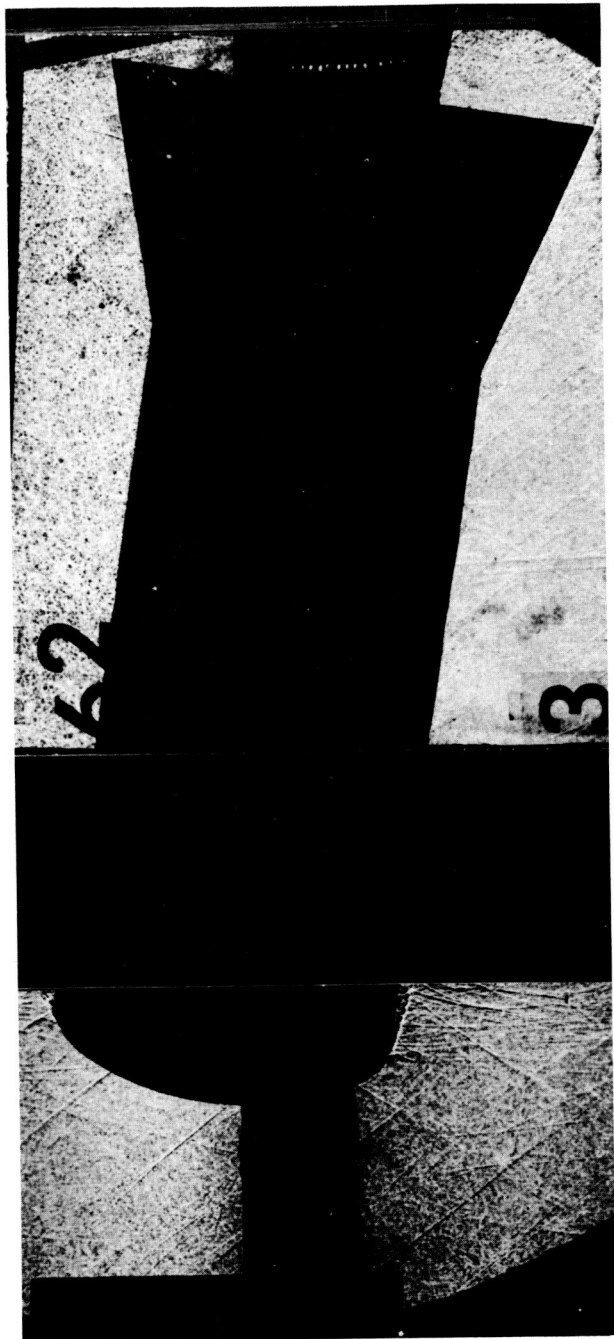
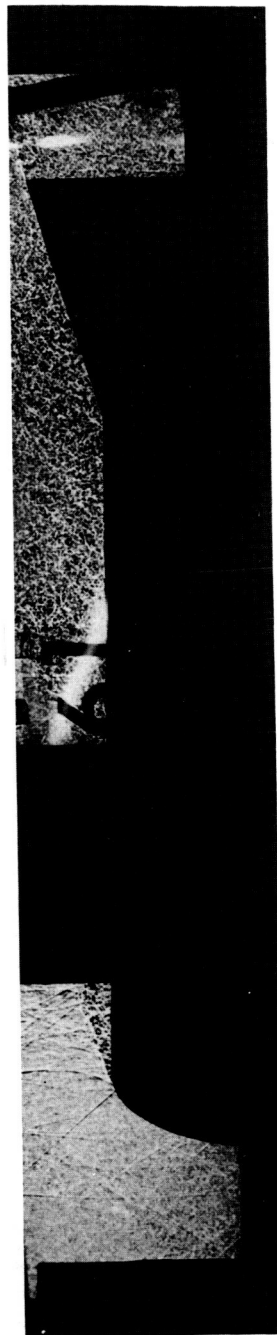
Figure 17.- Continued.

~~CONFIDENTIAL~~



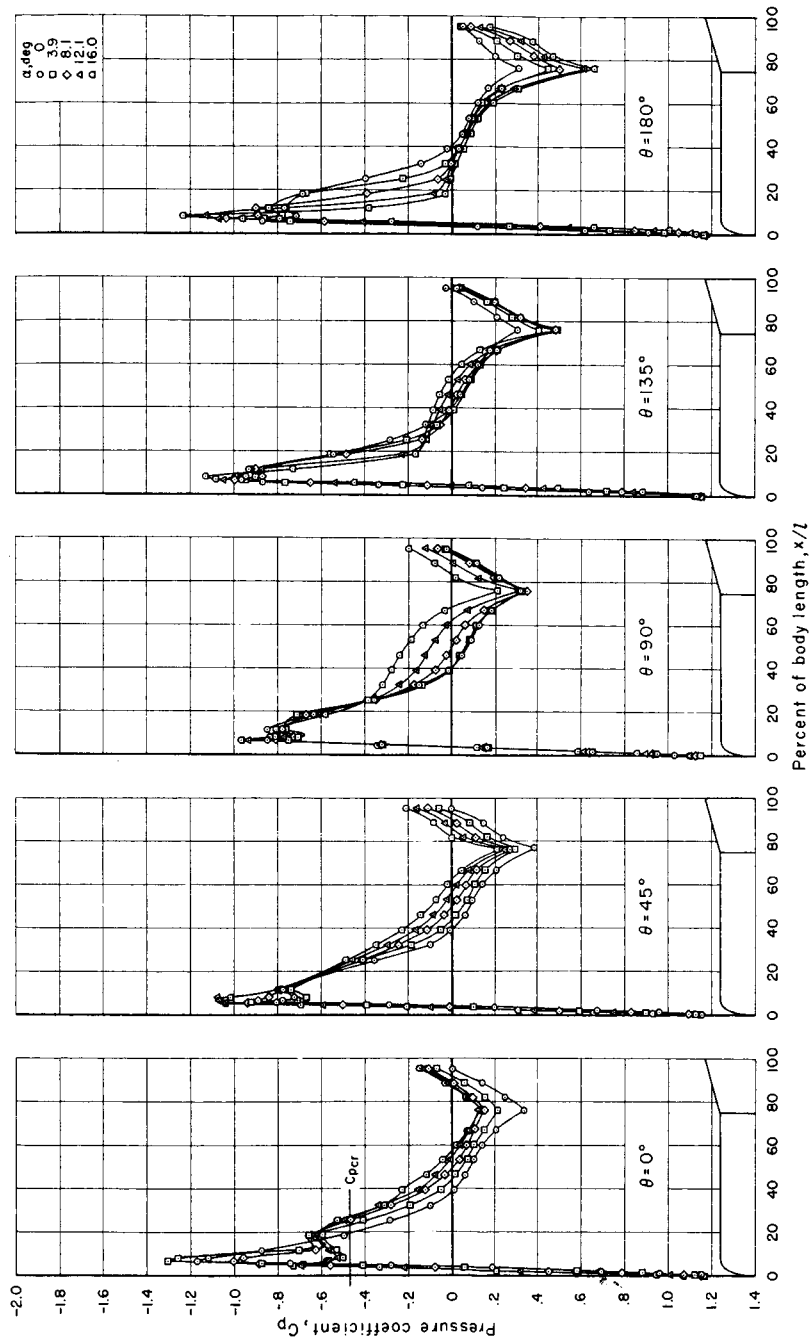
(c) Pressure distribution, $M = 0.60$.

Figure 17.- Continued.


 $\alpha = 8^\circ$

 $\alpha = 0^\circ$

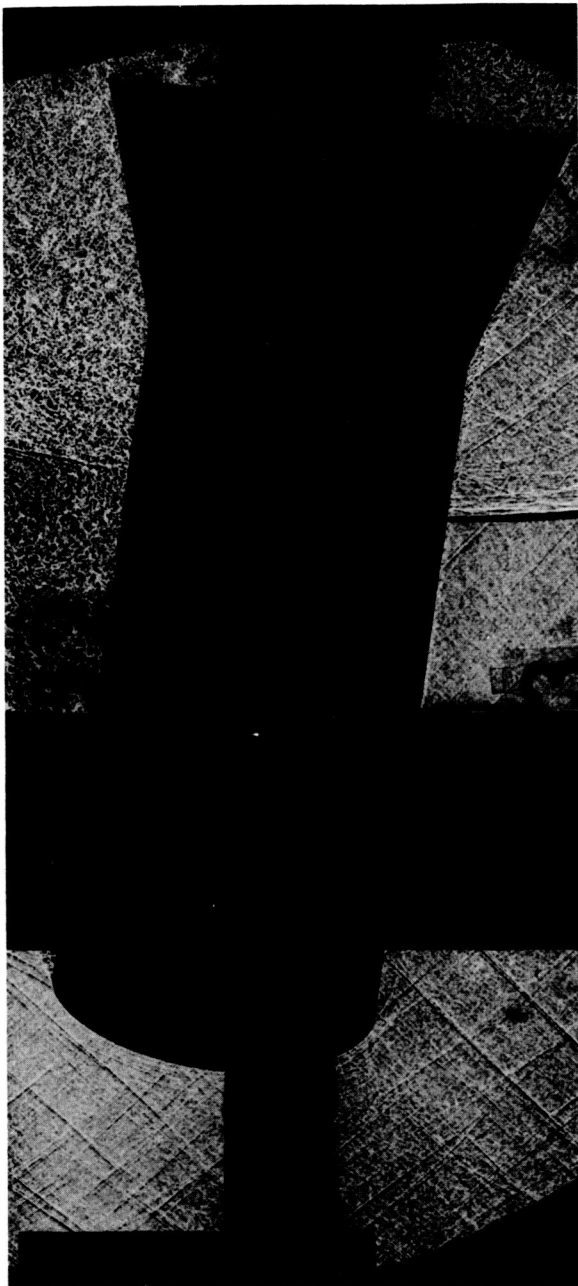
(a) Shadowgraph, $M = 0.80$.

Figure 17.- Continued.



(e) Pressure distribution, $M = 0.80$.

Figure 17.- Continued.

 $\alpha = 8^\circ$  $\alpha = 0^\circ$

(f) Shadowgraph, $M = 1.05$.

Figure 17.- Continued.

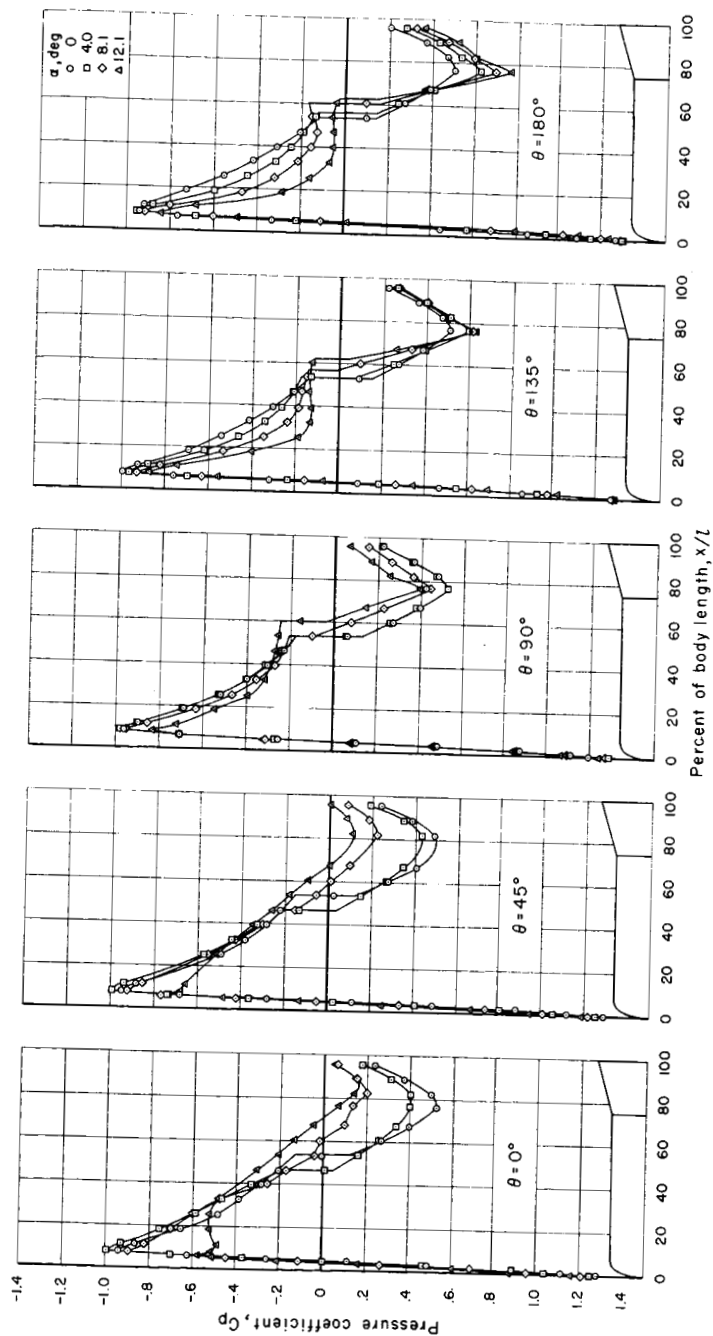
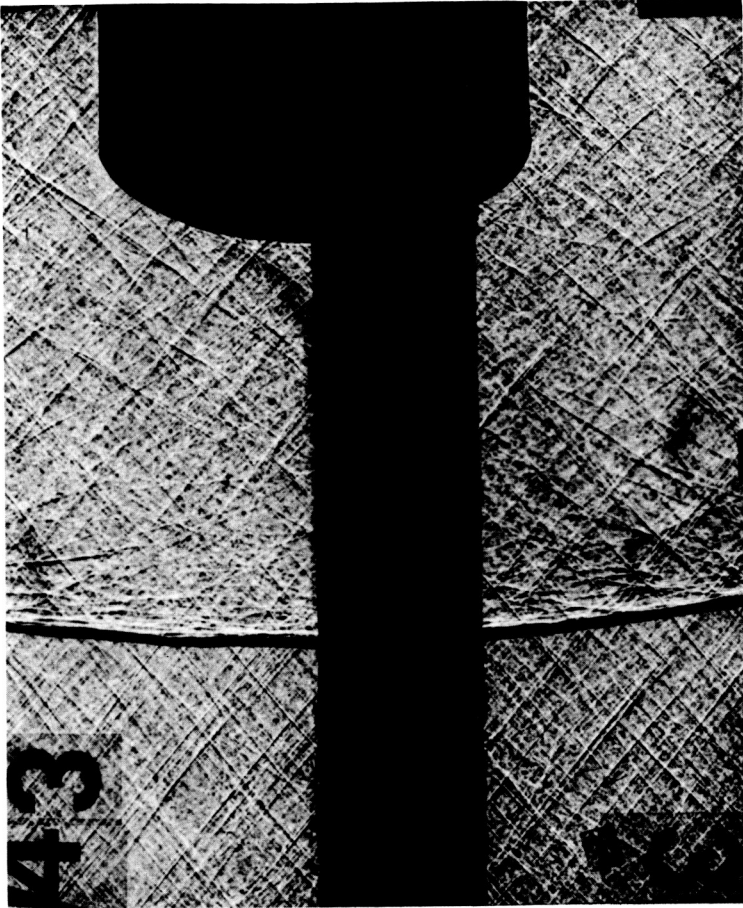
(g) Pressure distribution, $M = 1.05$.

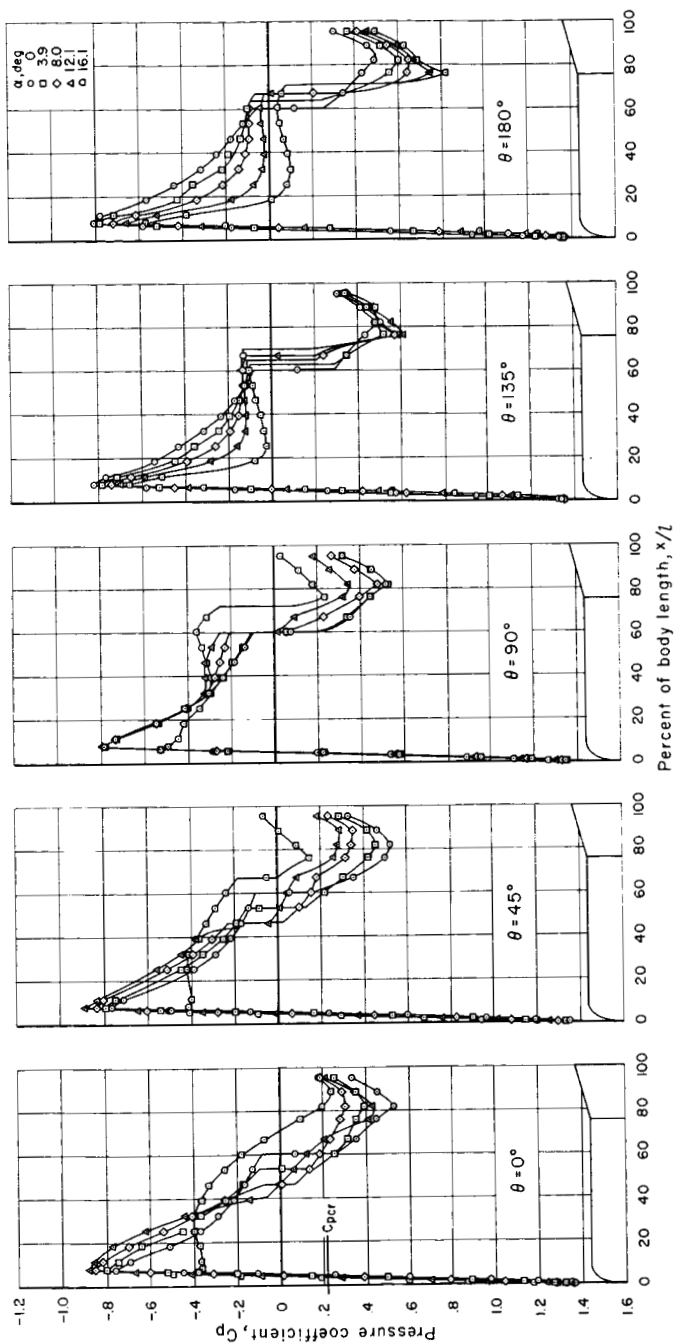
Figure 17.- Continued.



$$\alpha = 0^{\circ}$$

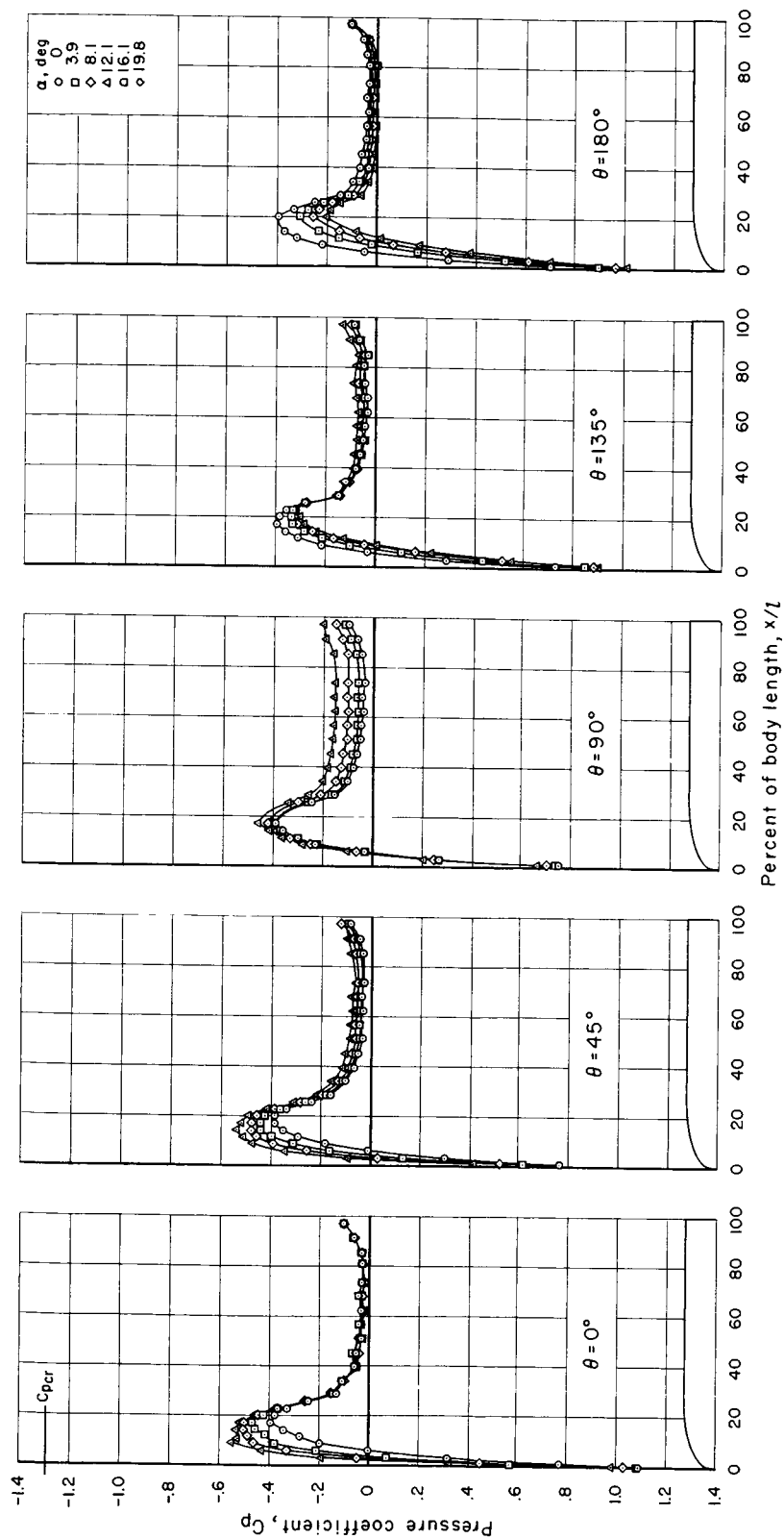
(h) Shadowgraph, $M = 1.15$.

Figure 17.- Continued.



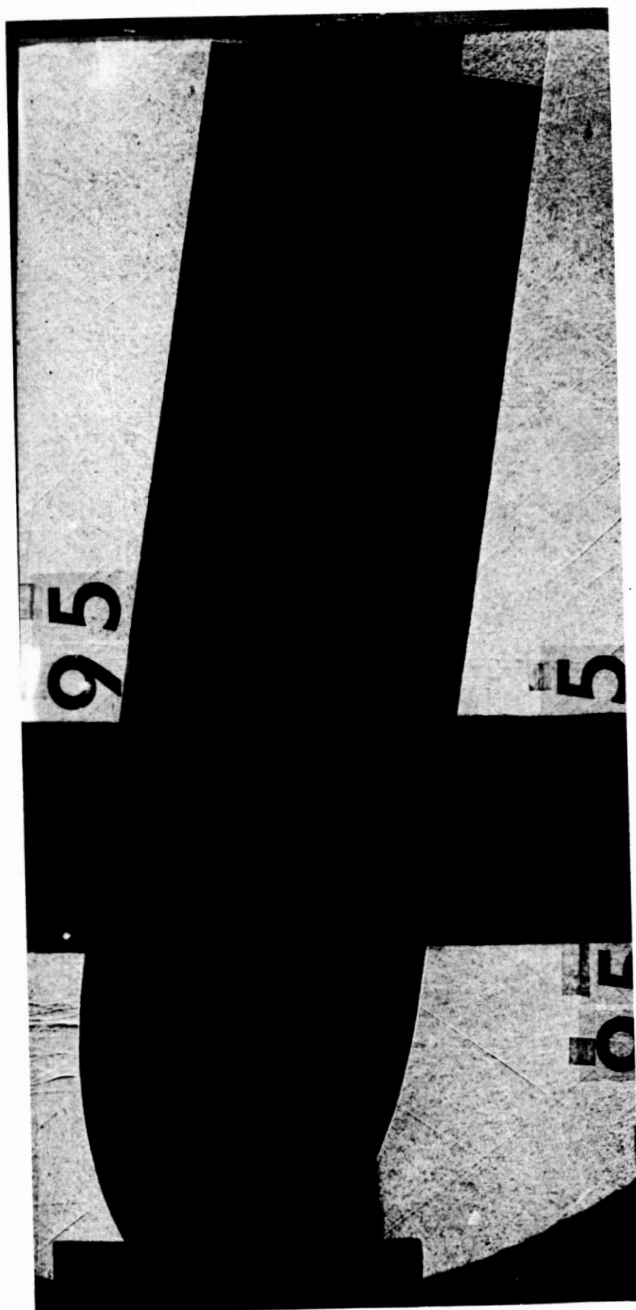
(i) Pressure distribution, $M = 1.15$.

Figure 17.- Concluded.



(a) Pressure distribution, $M = 0.60$.

Figure 18.- Pressure distribution and shadowgraph of the flow of the prolate-nosed model without the flare.



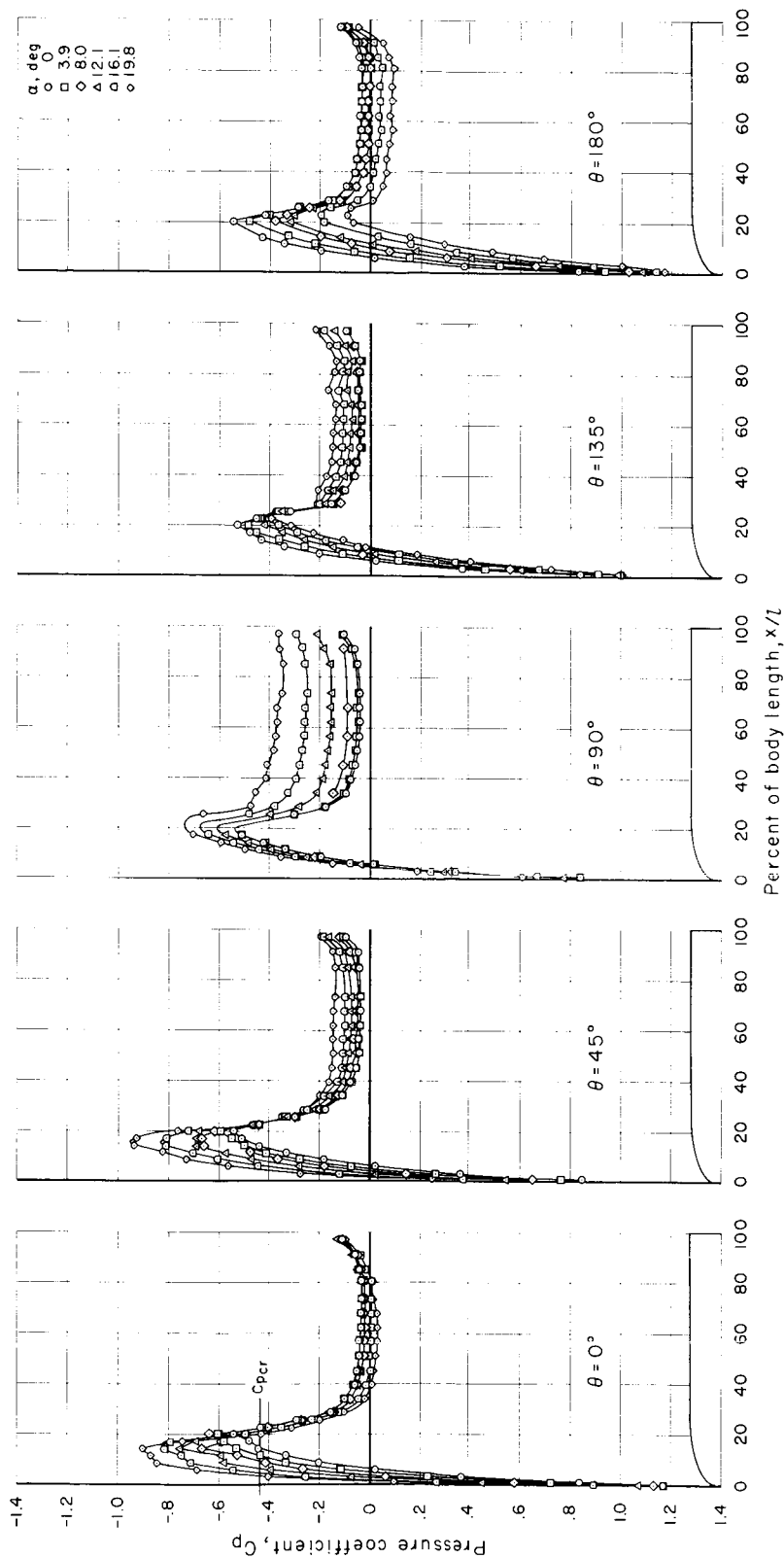
$\alpha = 8^\circ$



$\alpha = 0^\circ$

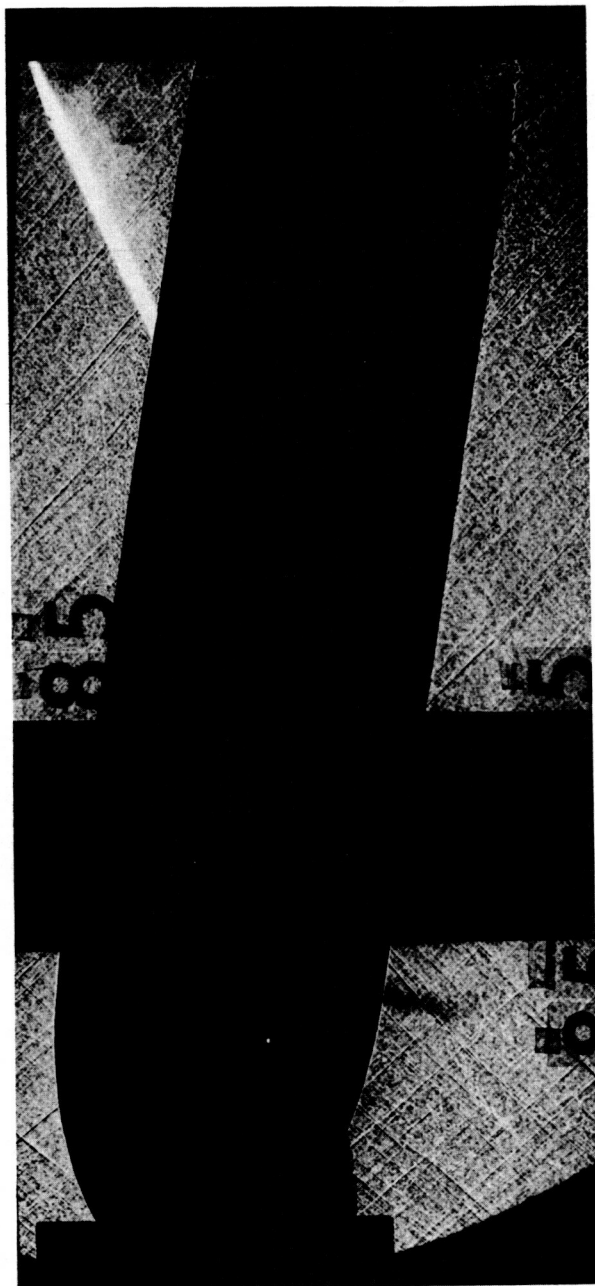
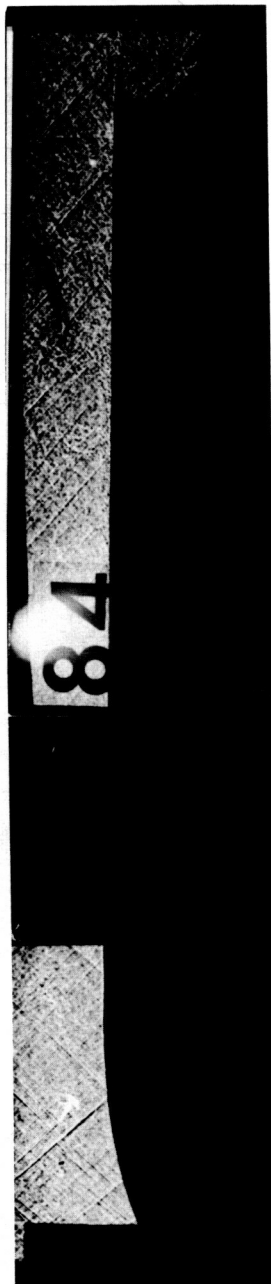
(b) Shadowgraph, $M = 0.80$.

Figure 18.- Continued.



(c) Pressure distribution, $M = 0.80$.

Figure 18.- Continued.


 $\alpha = 8^\circ$

 $\alpha = 0^\circ$

(a) Shadowgraph, $M = 1.05$.

Figure 18.- Continued.

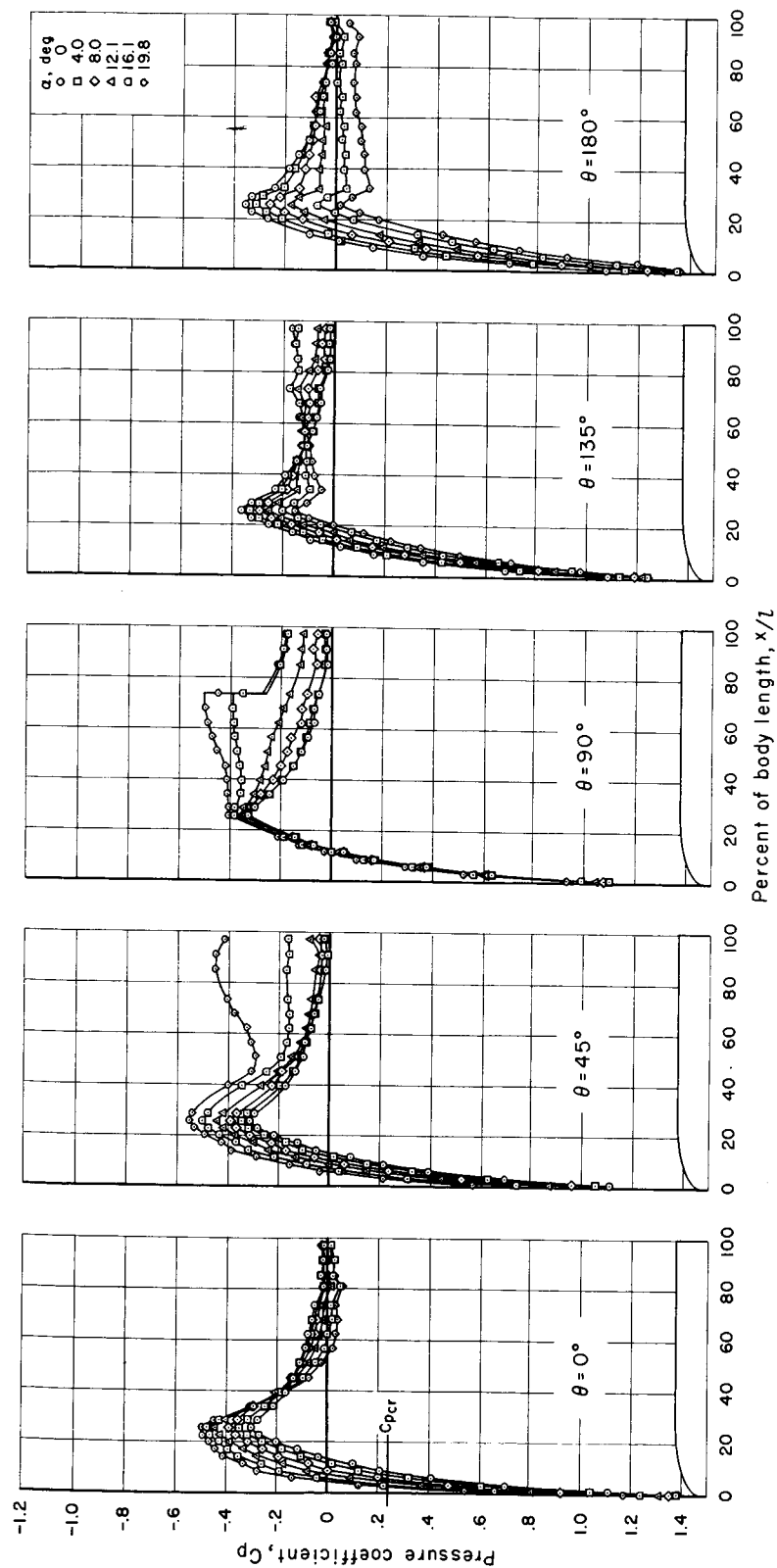
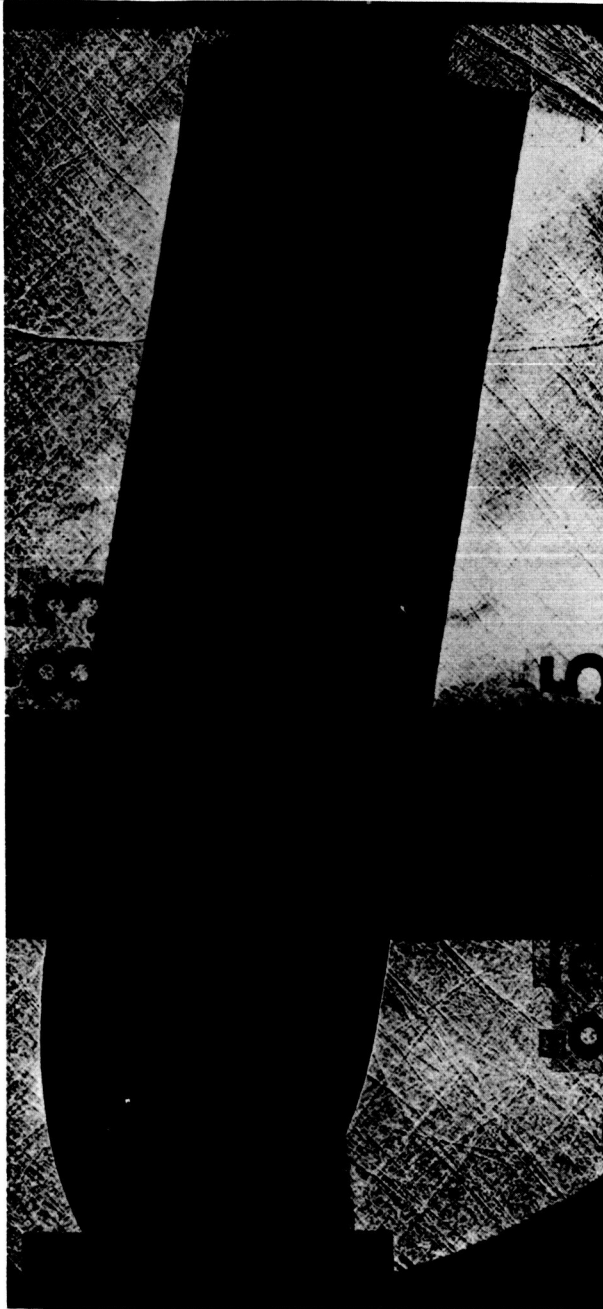
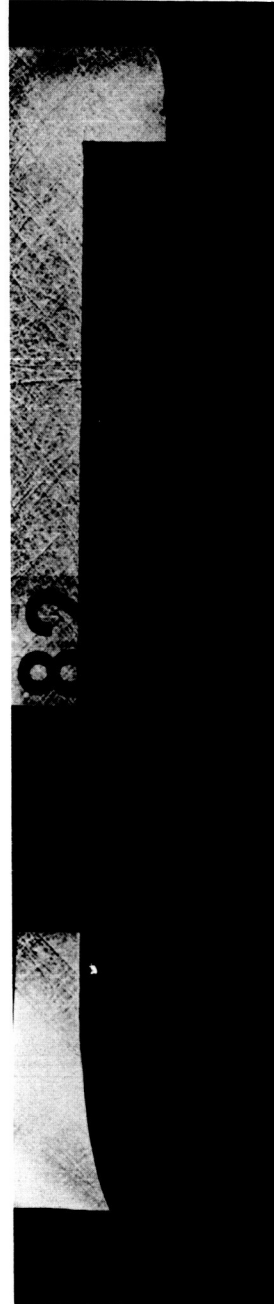
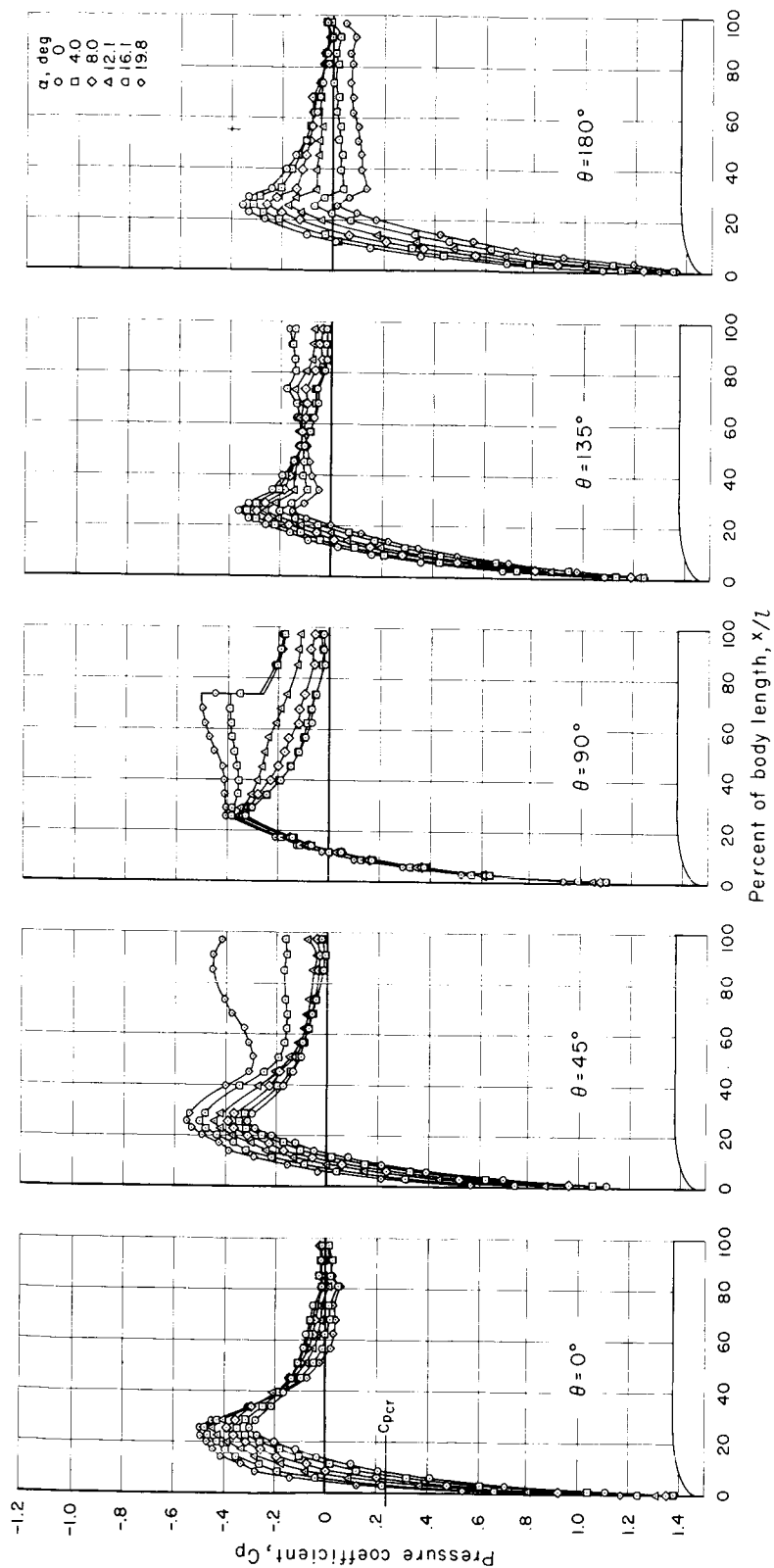
(g) Pressure distribution, $M = 1.18$.

Figure 18.- Concluded.


 $\alpha = 8^\circ$

 $\alpha = 0^\circ$

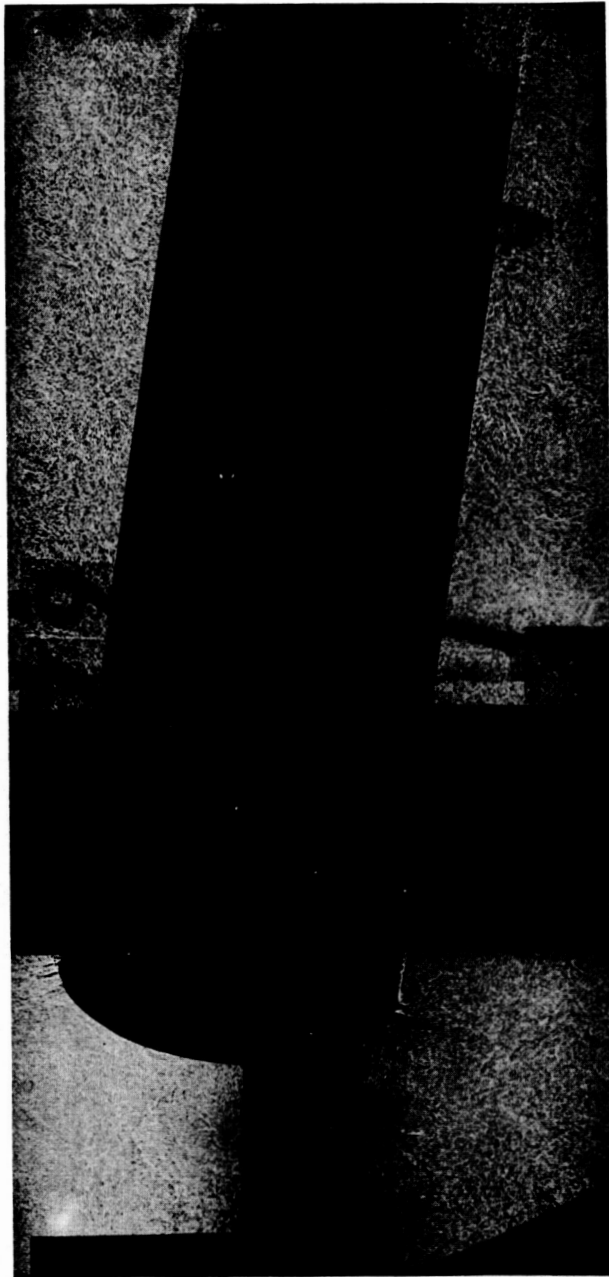
(f) Shadowgraph, $M = 1.18$.

Figure 18.- Continued.



(g) Pressure distribution, $M = 1.18$.

Figure 18.- Concluded.

~~CONFIDENTIAL~~ $\alpha = 8^\circ$  $\alpha = 0^\circ$

(a) Shadowgraph, $M = 0.60$.

Figure 19.- Pressure distribution and shadowgraph of the flow of the oblate-nosed model without the flare.

~~CONFIDENTIAL~~

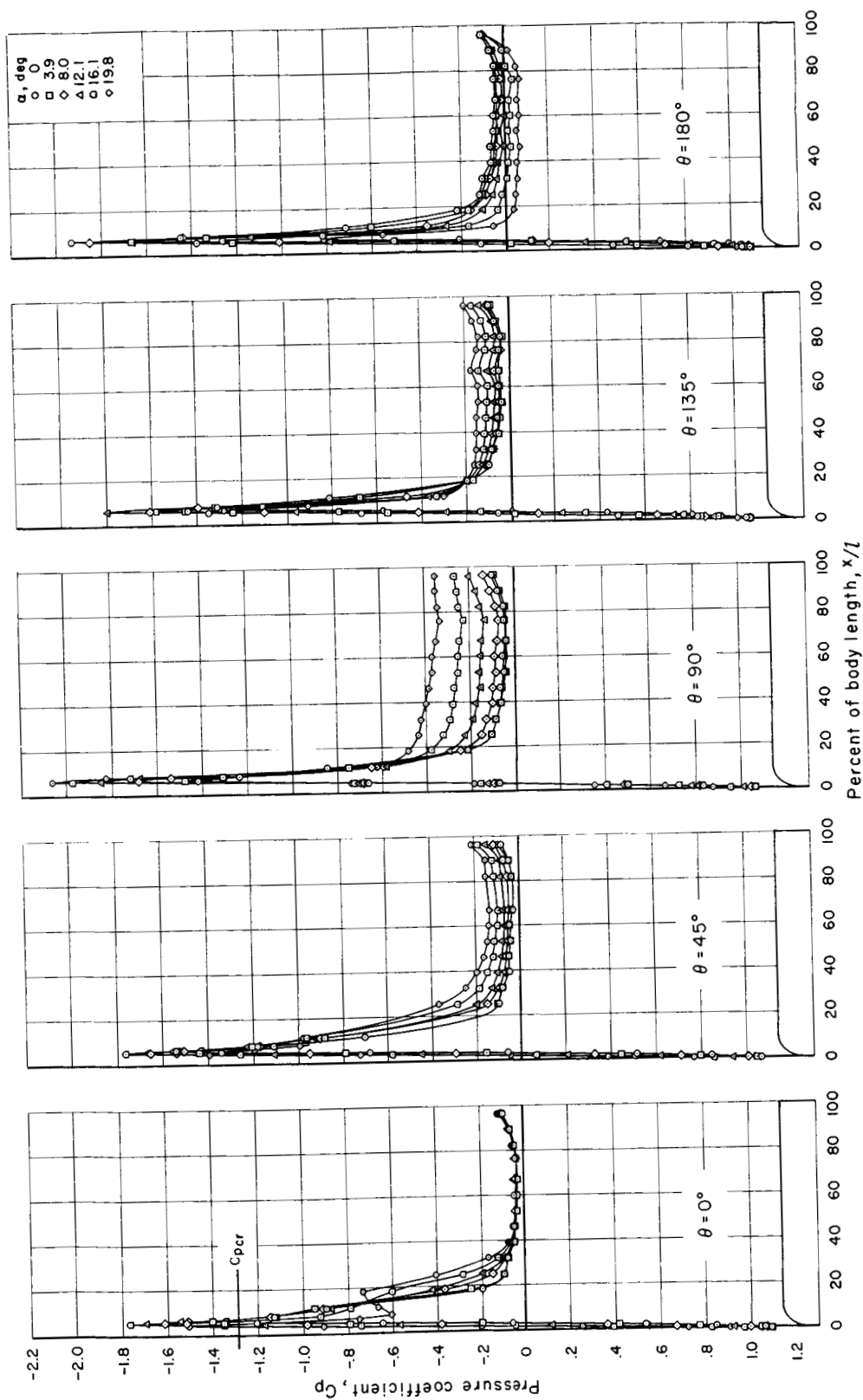
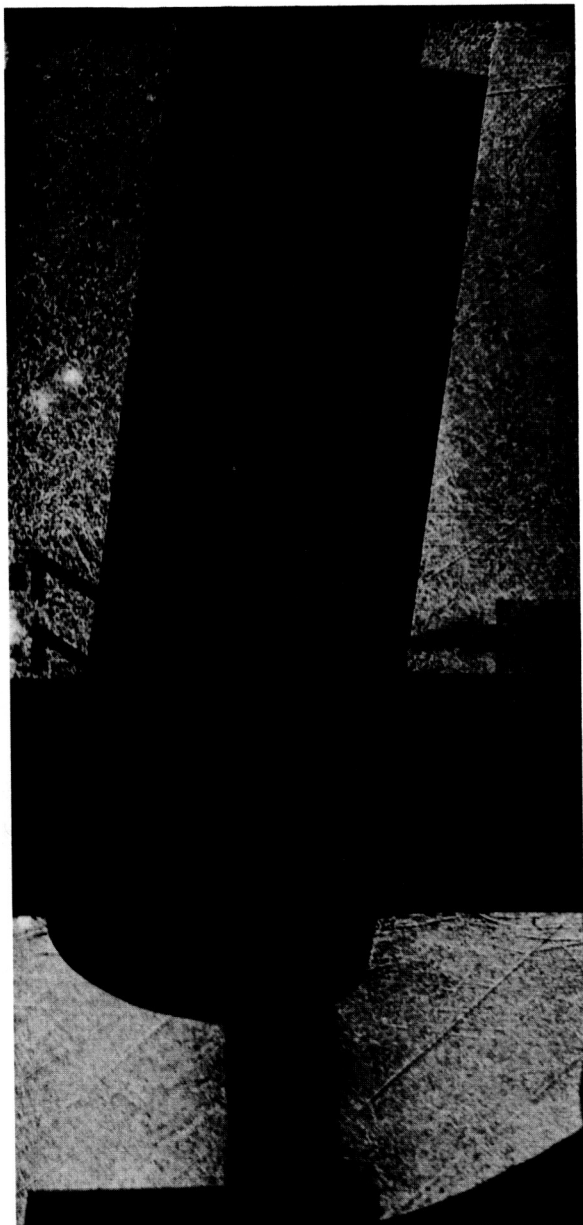
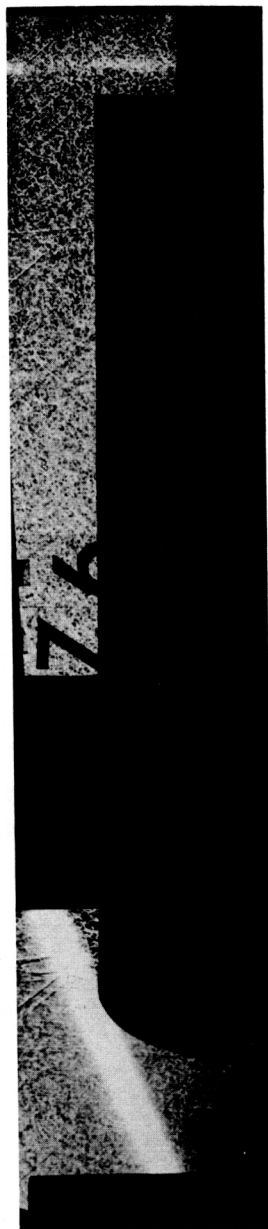
(b) Pressure distribution, $M = 0.60$.

Figure 19.- Continued.

~~CONFIDENTIAL~~

$$\alpha = 8^{\circ}$$

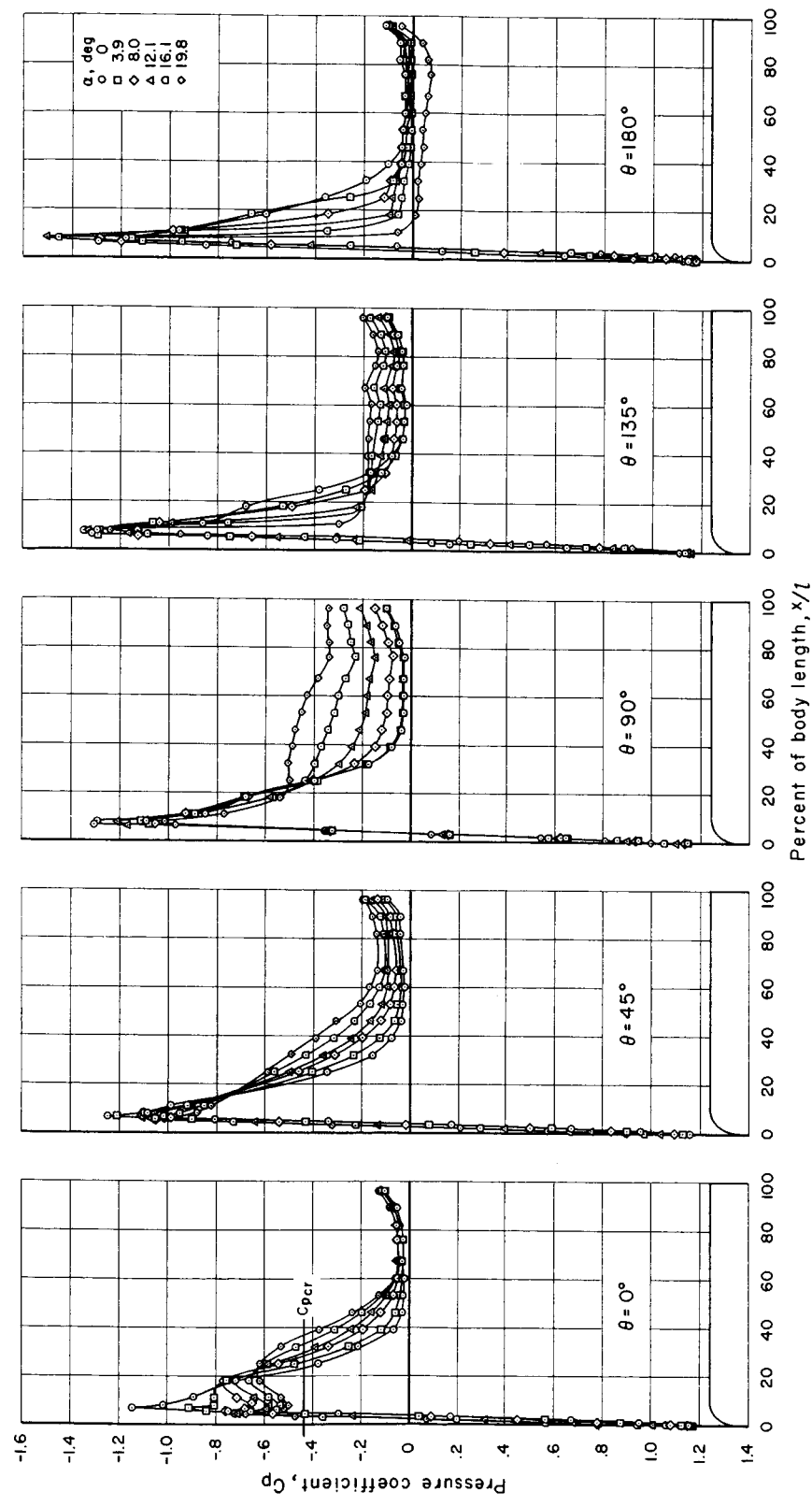


$\alpha = 0^{\circ}$
(c) Shadowgraph, $M = 0.80$.

Figure 19.- Continued.

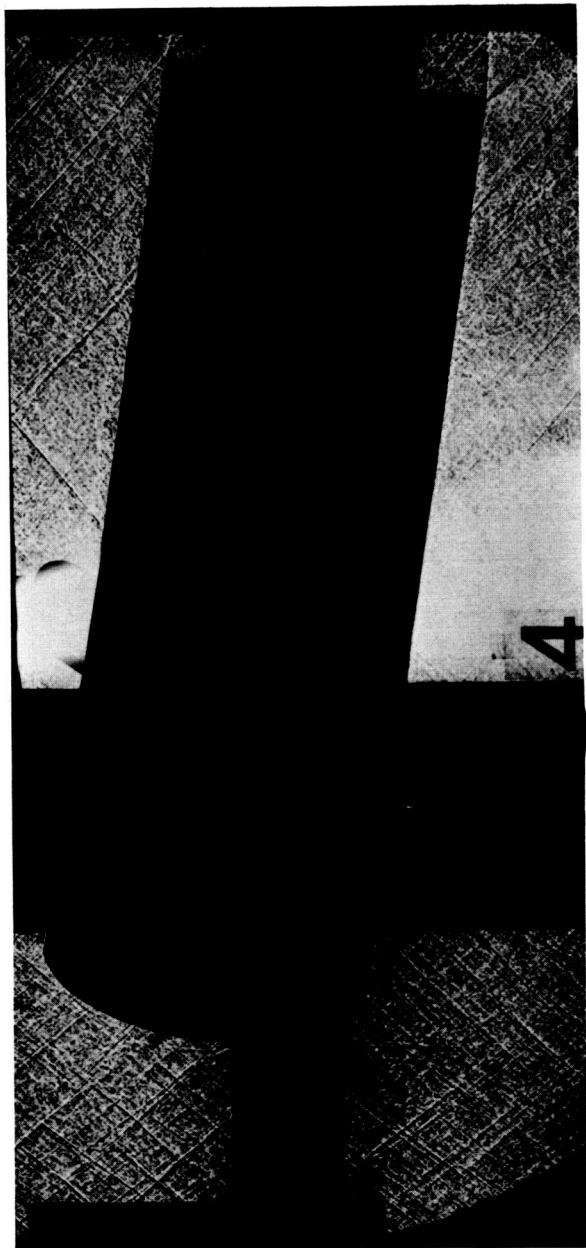
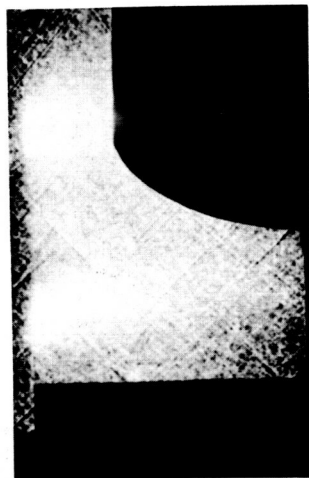
A
2
9
6

~~CONFIDENTIAL~~



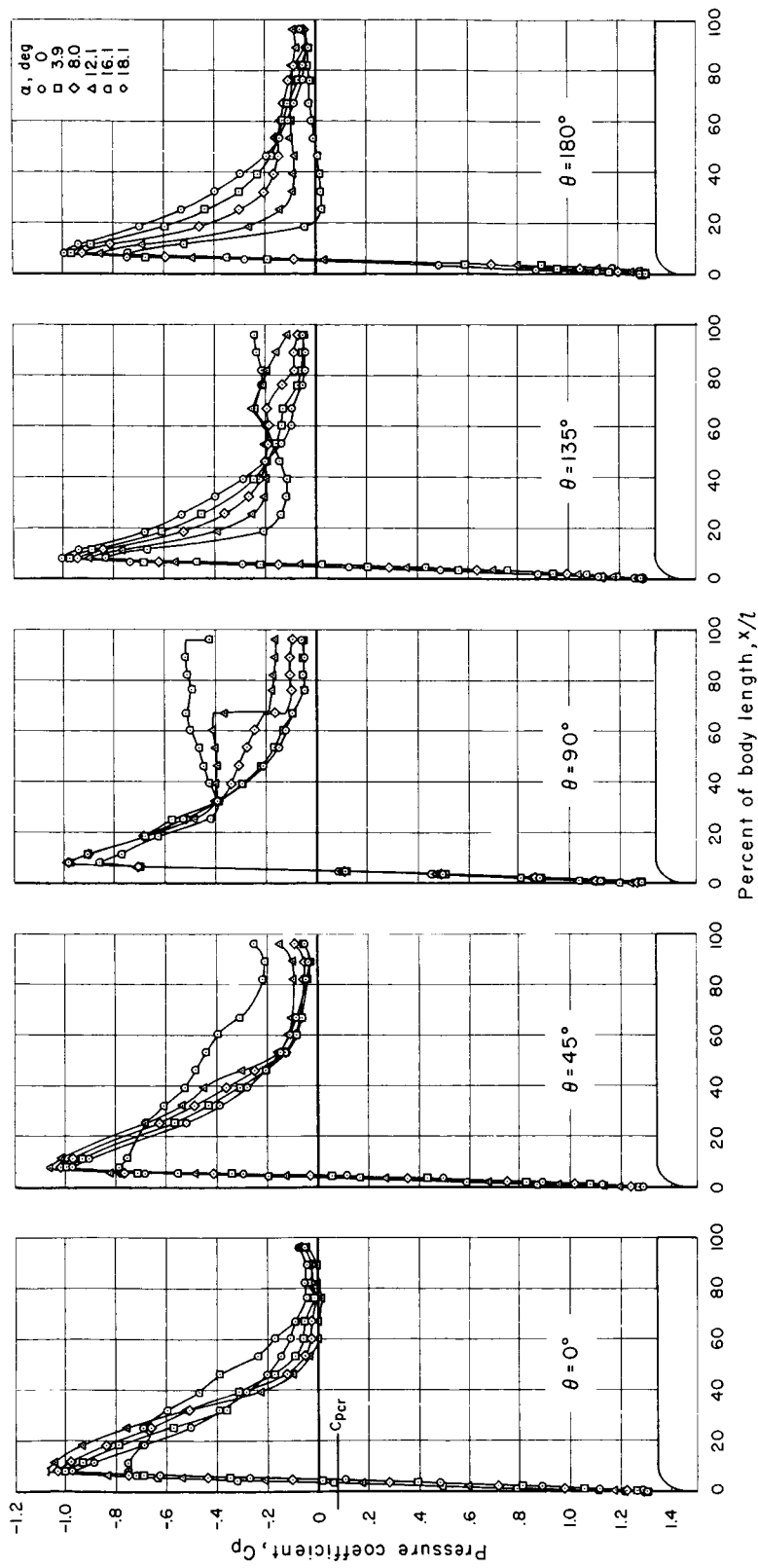
(d) Pressure distribution, $M = 0.80$.

Figure 19.- Continued.


 $\alpha = 80^\circ$

 $\alpha = 0^\circ$

(e) Shadowgraph, $M = 1.05$.

Figure 19.- Continued.



(f) Pressure distribution, $M = 1.05$.

Figure 19.- Continued.

~~CONFIDENTIAL~~

A
2
9
6

~~CONFIDENTIAL~~

CONFIDENTIAL

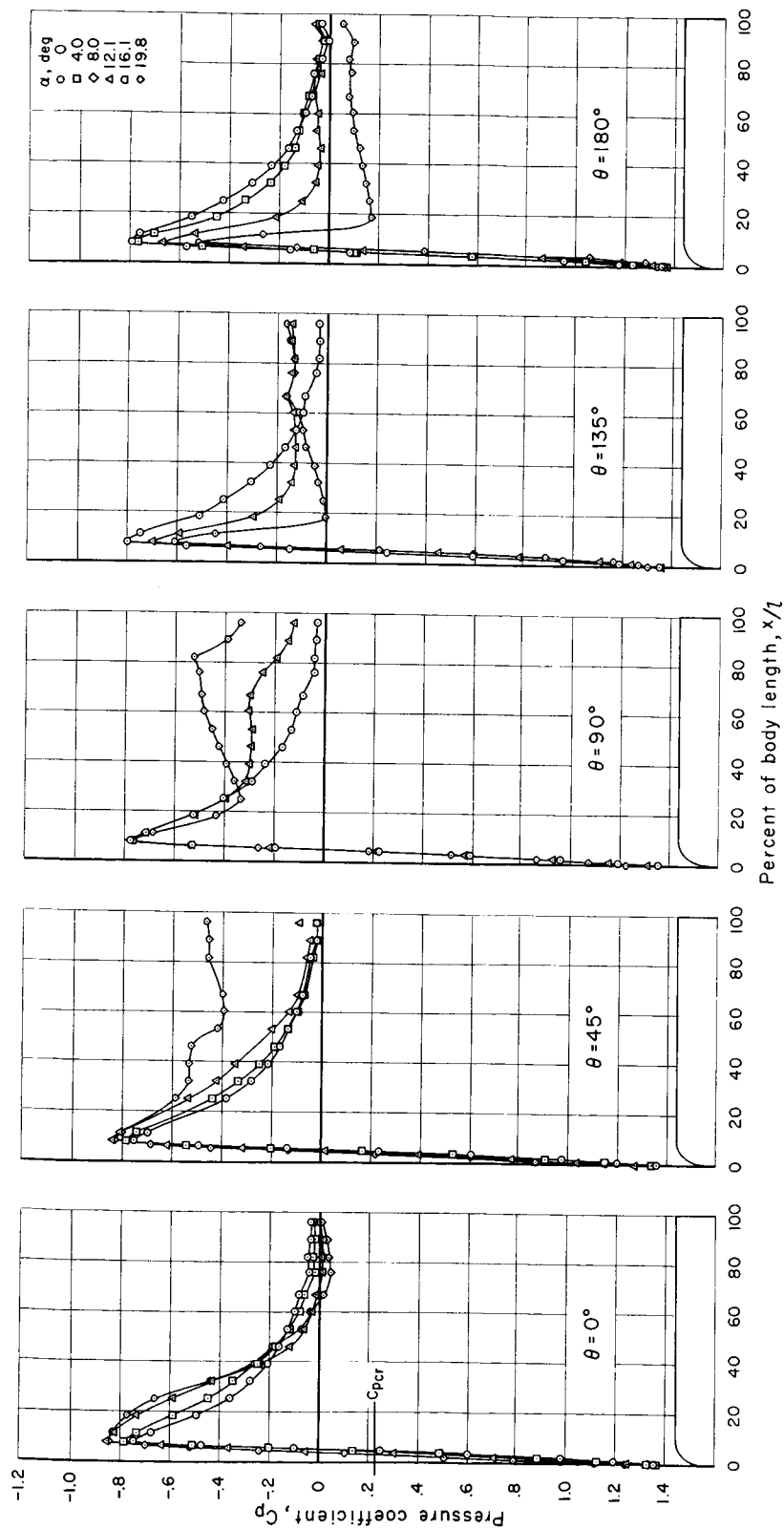
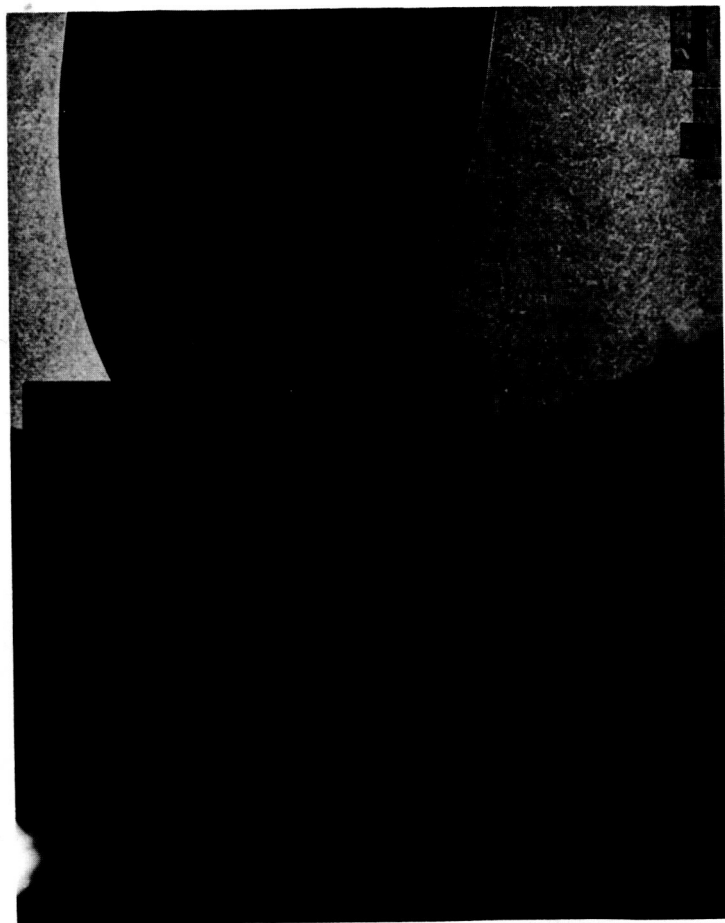
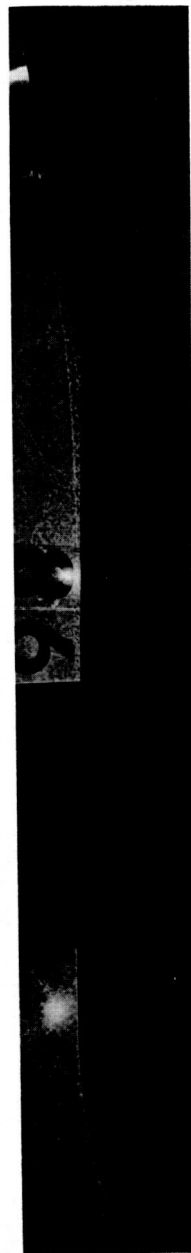
(g) Pressure distribution, $M = 1.16$.

Figure 19.- Concluded.

CONFIDENTIAL



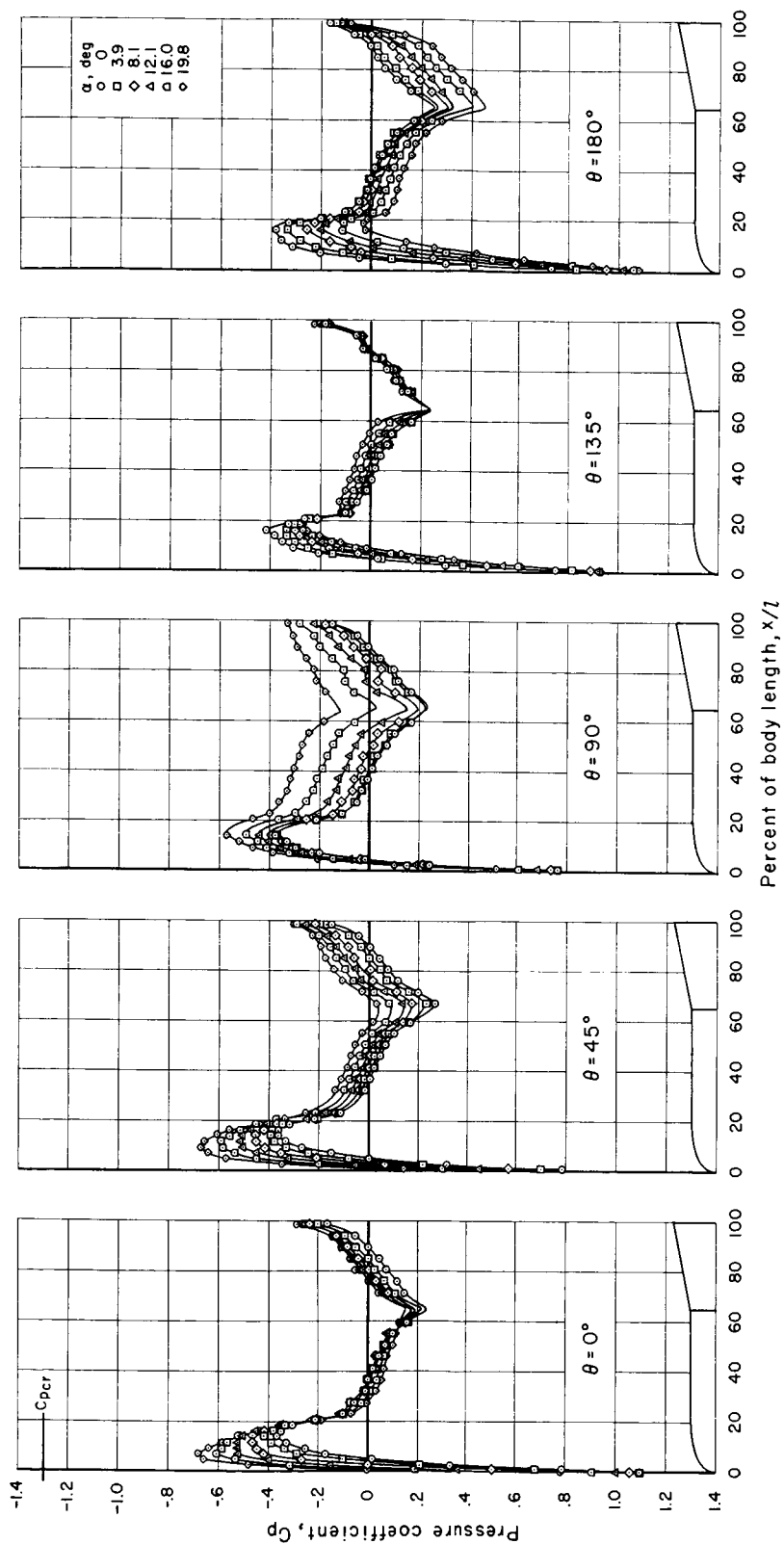
$\alpha = 8^\circ$



$\alpha = 0^\circ$

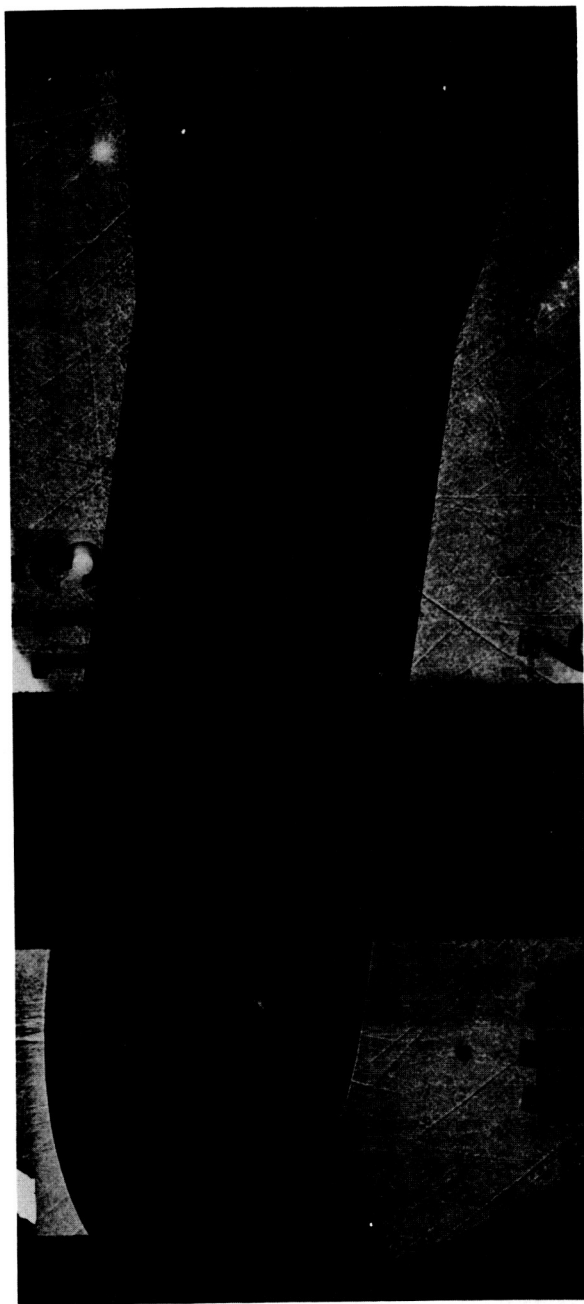
(a) Shadowgraph, $M = 0.60$.

Figure 20.- Pressure distribution and shadowgraph of the flow of the prolate-nosed model with the extended flare.



(b) Pressure distribution, $M = 0.60$.

Figure 20.- Continued.

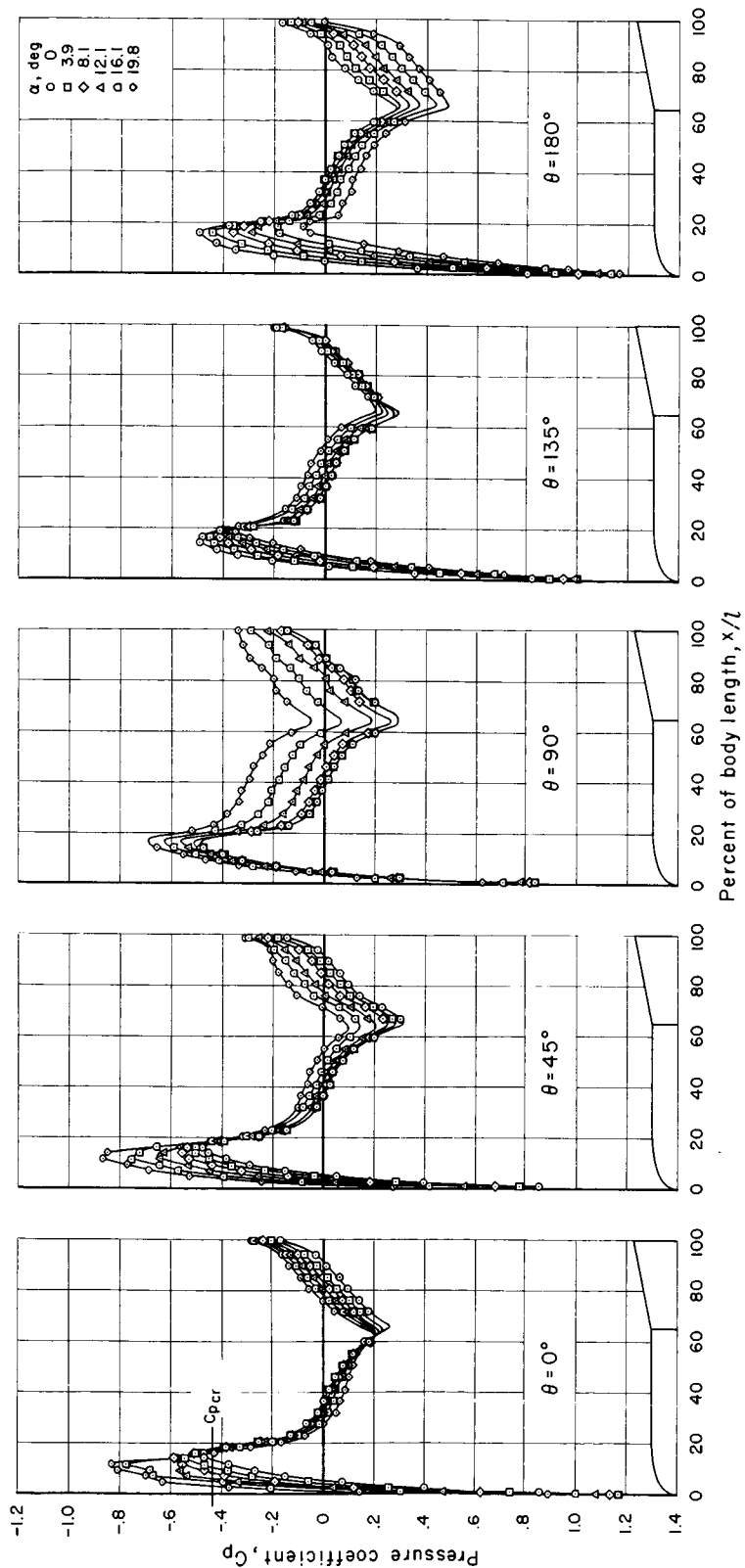


$\alpha = 8^{\circ}$



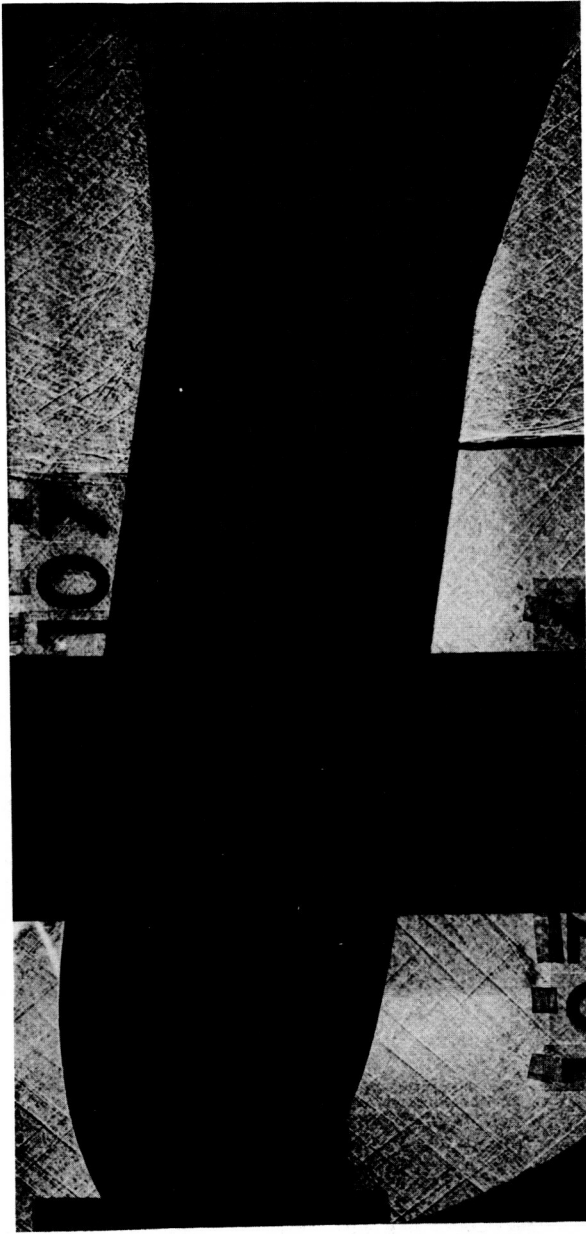
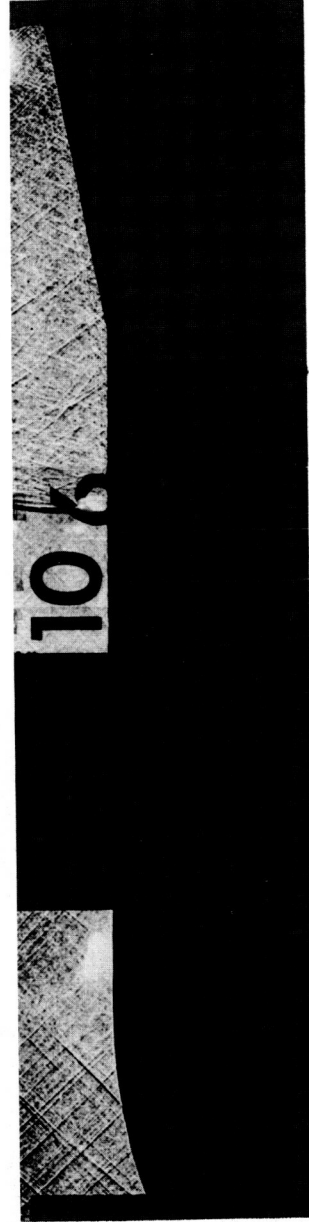
$\alpha = 0^{\circ}$
(c) Shadowgraph, $M = 0.80$.

Figure 20.- Continued.



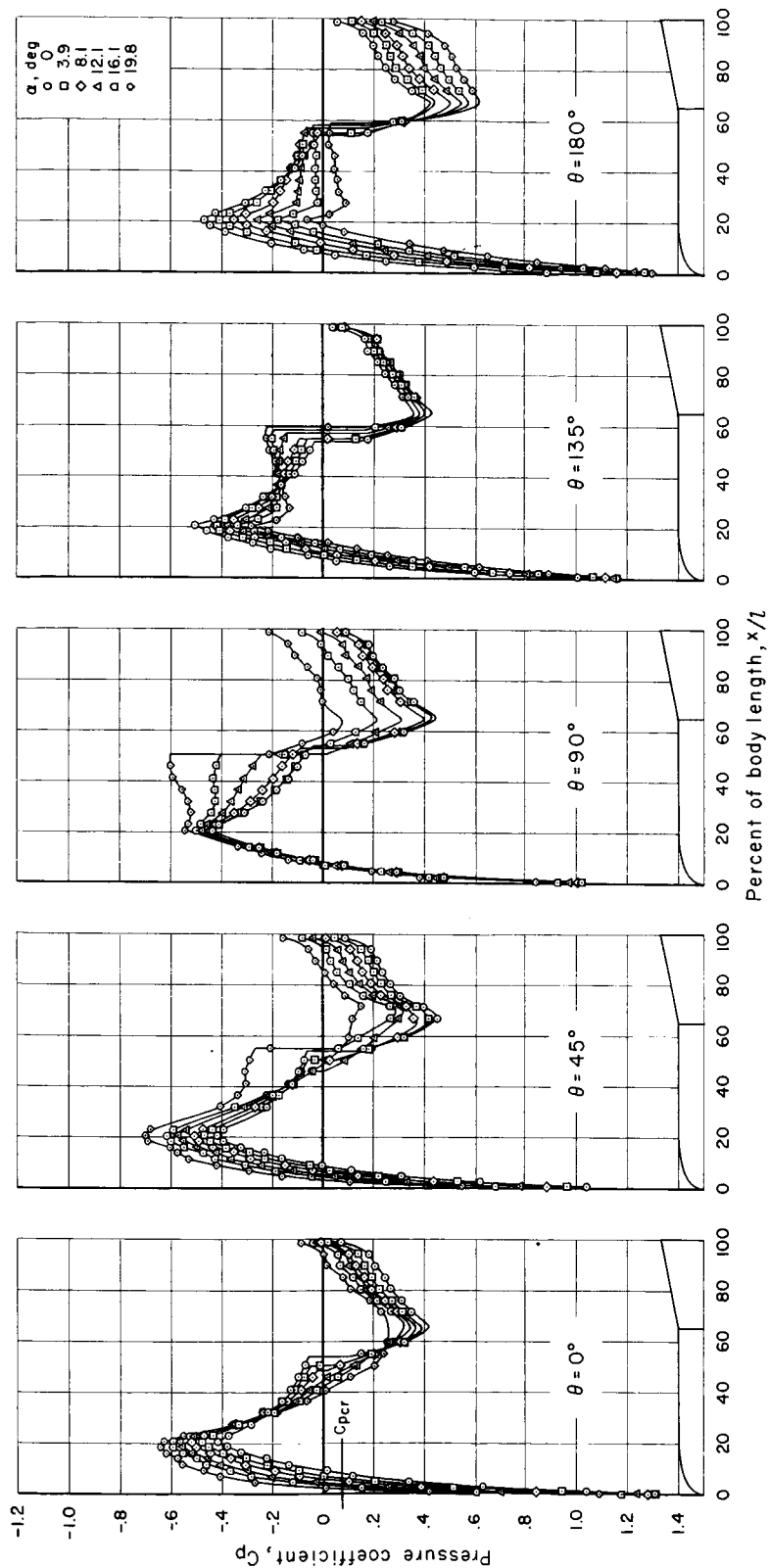
(d) Pressure distribution, $M = 0.80$.

Figure 20.- Continued.

 $\alpha = 8^\circ$  $\alpha = 0^\circ$

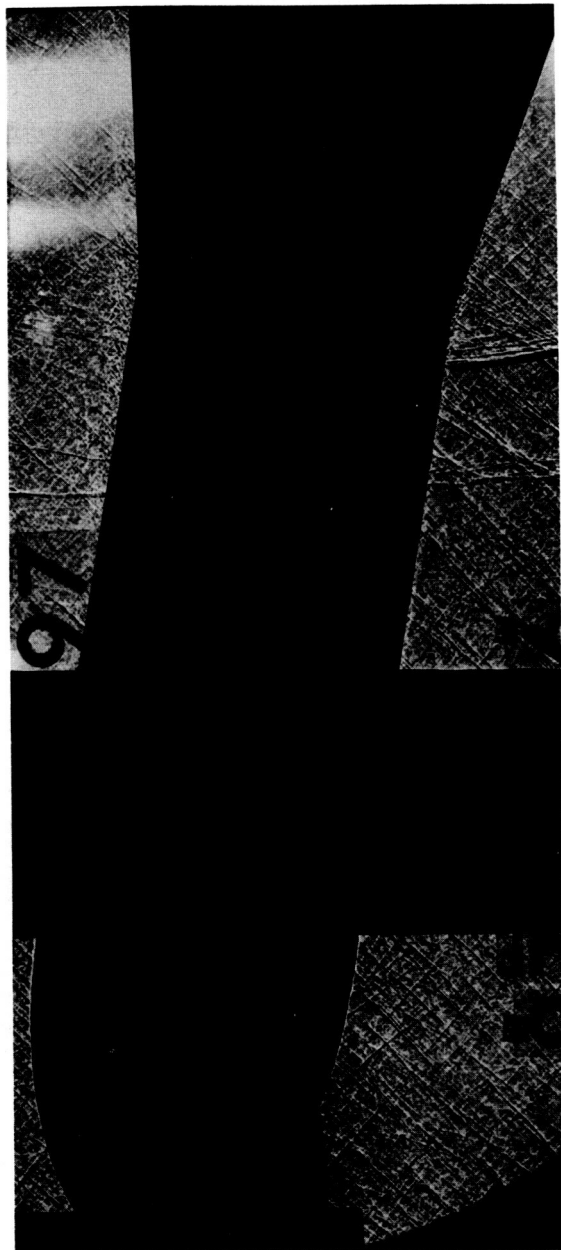
(e) Shadowgraph, $M = 1.05$.

Figure 20.- Continued.



(f) Pressure distribution, $M = 1.05$.

Figure 20.- Continued.

 $\alpha = 8^{\circ}$  $\alpha = 0^{\circ}$

(g) Shadowgraph, $M = 1.15$.

Figure 20.- Continued.

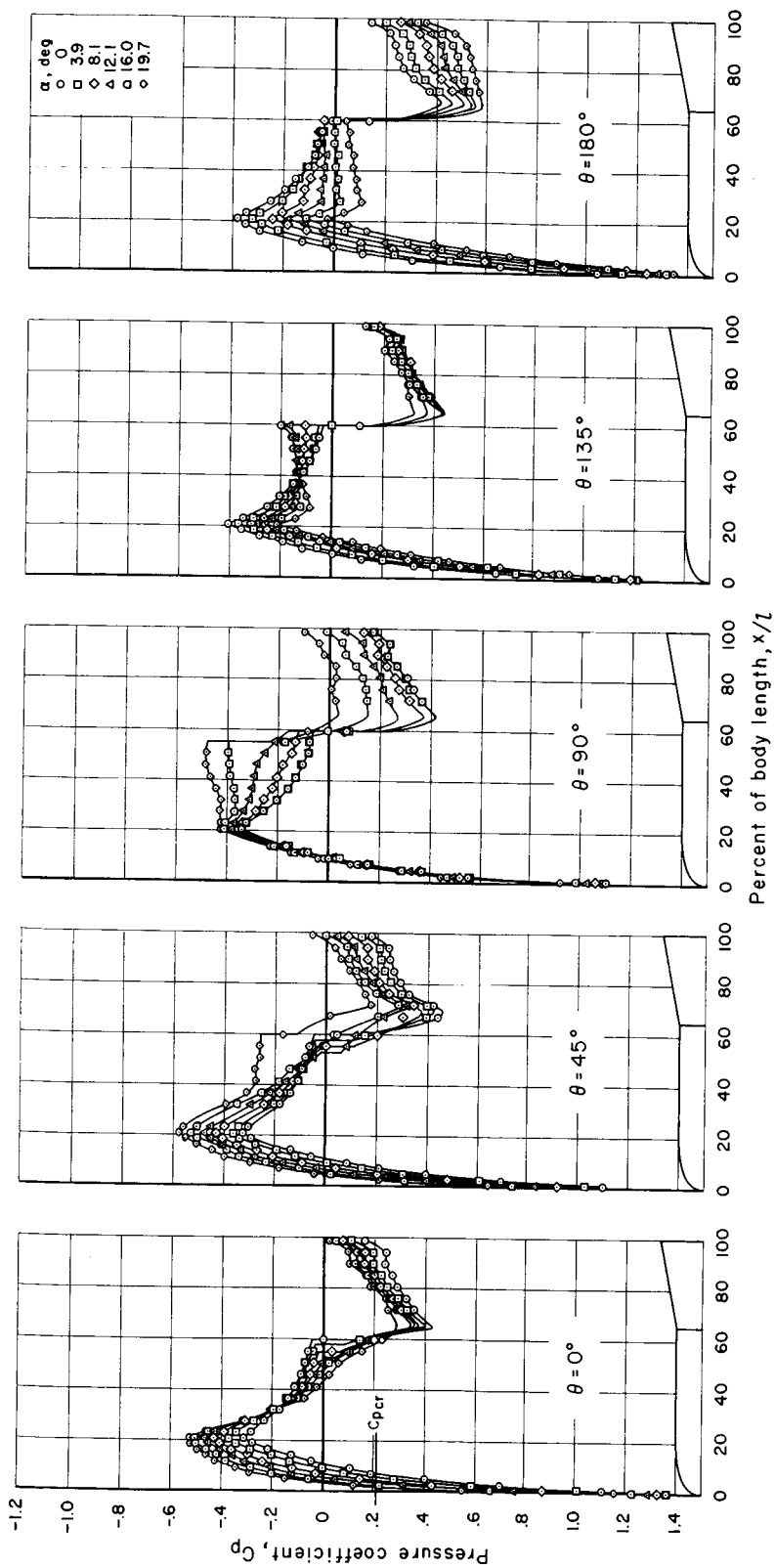
(h) Pressure distribution, $M = 1.15$.

Figure 20.- Concluded.

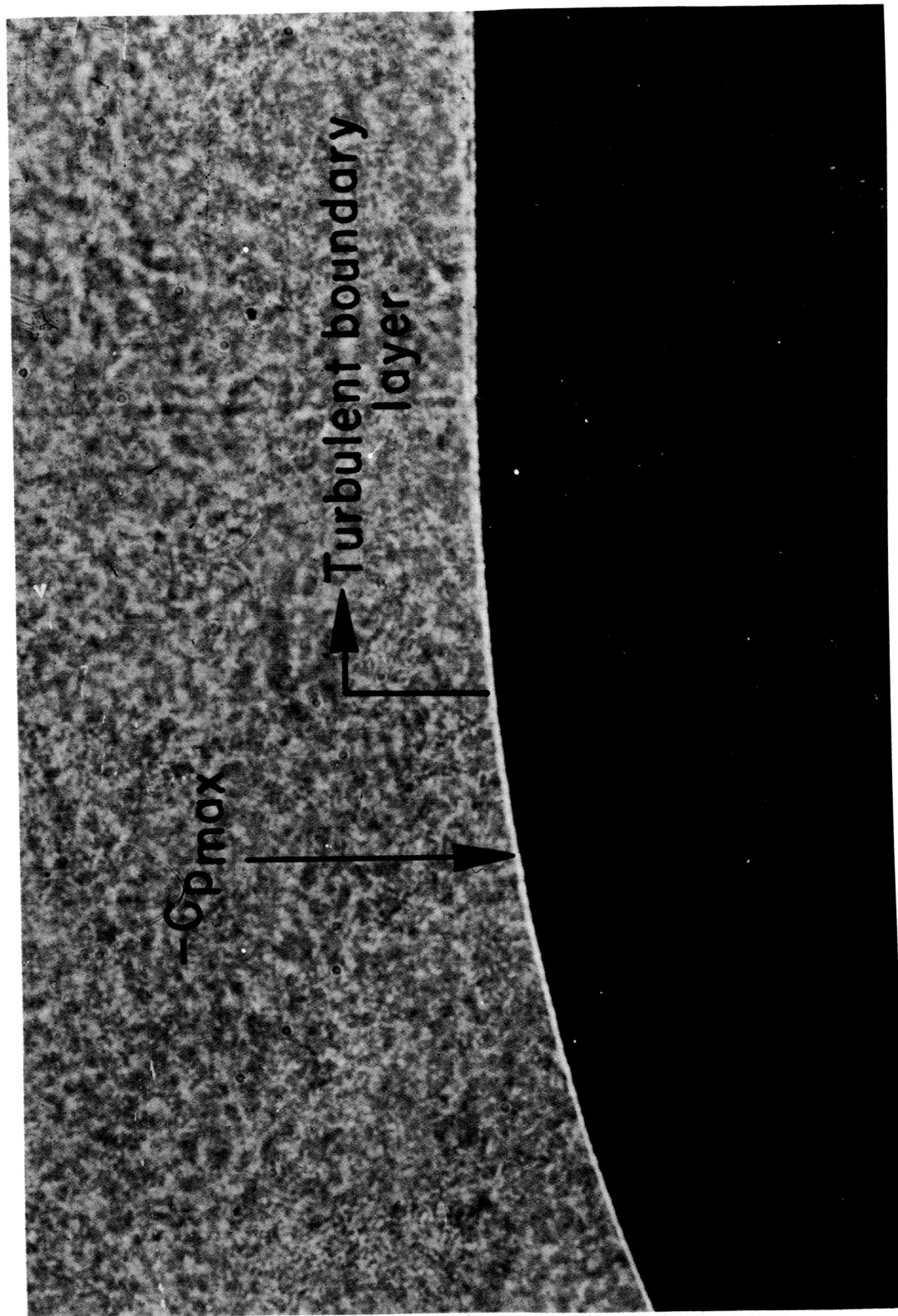


Figure 21.- Boundary-layer transition of the prolate-nosed model for an angle of attack of 0° at 0.60 Mach number.

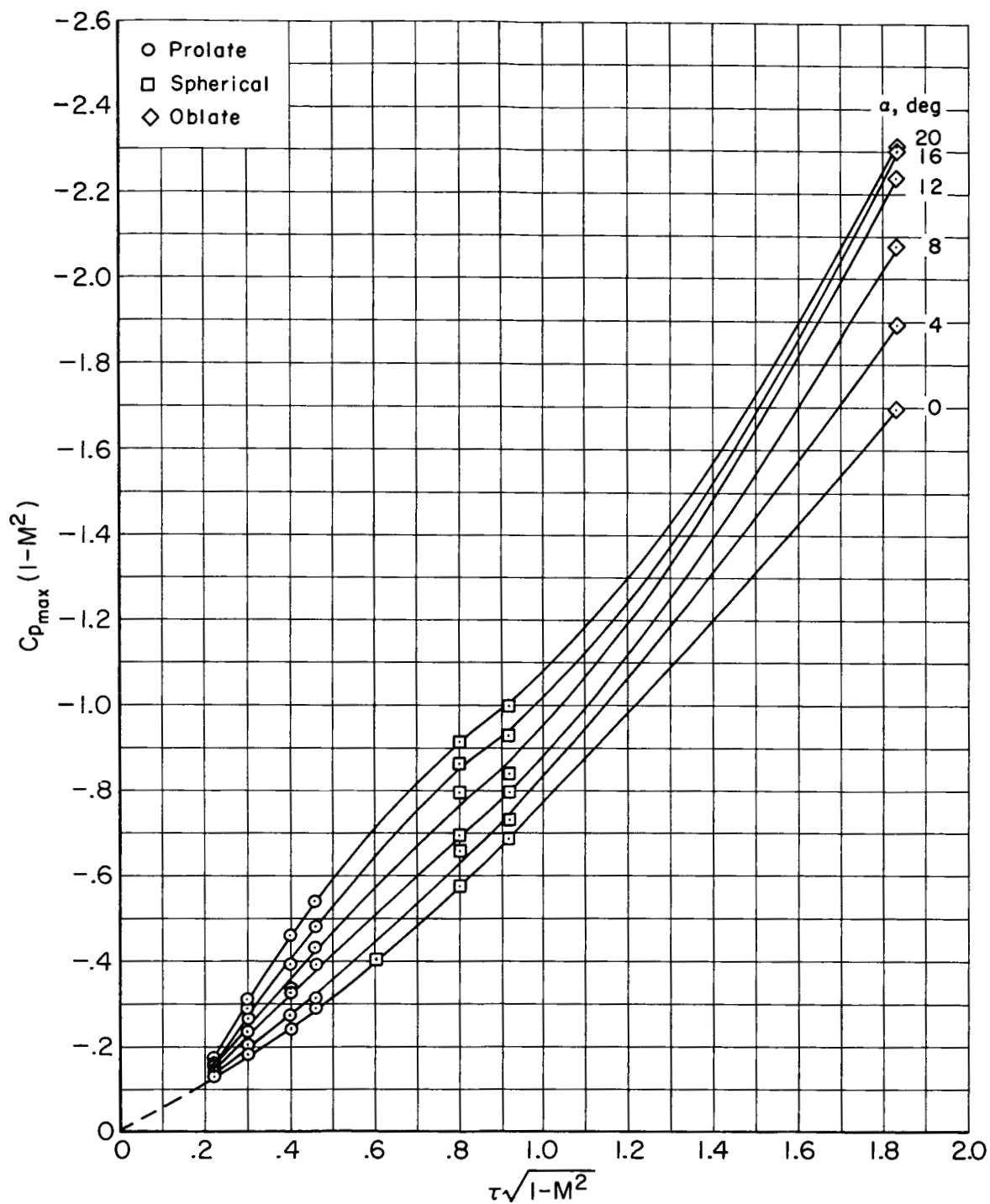


Figure 22.- Correlation of maximum negative pressure coefficient of the various nose shapes by the variables of Gothert's rule.

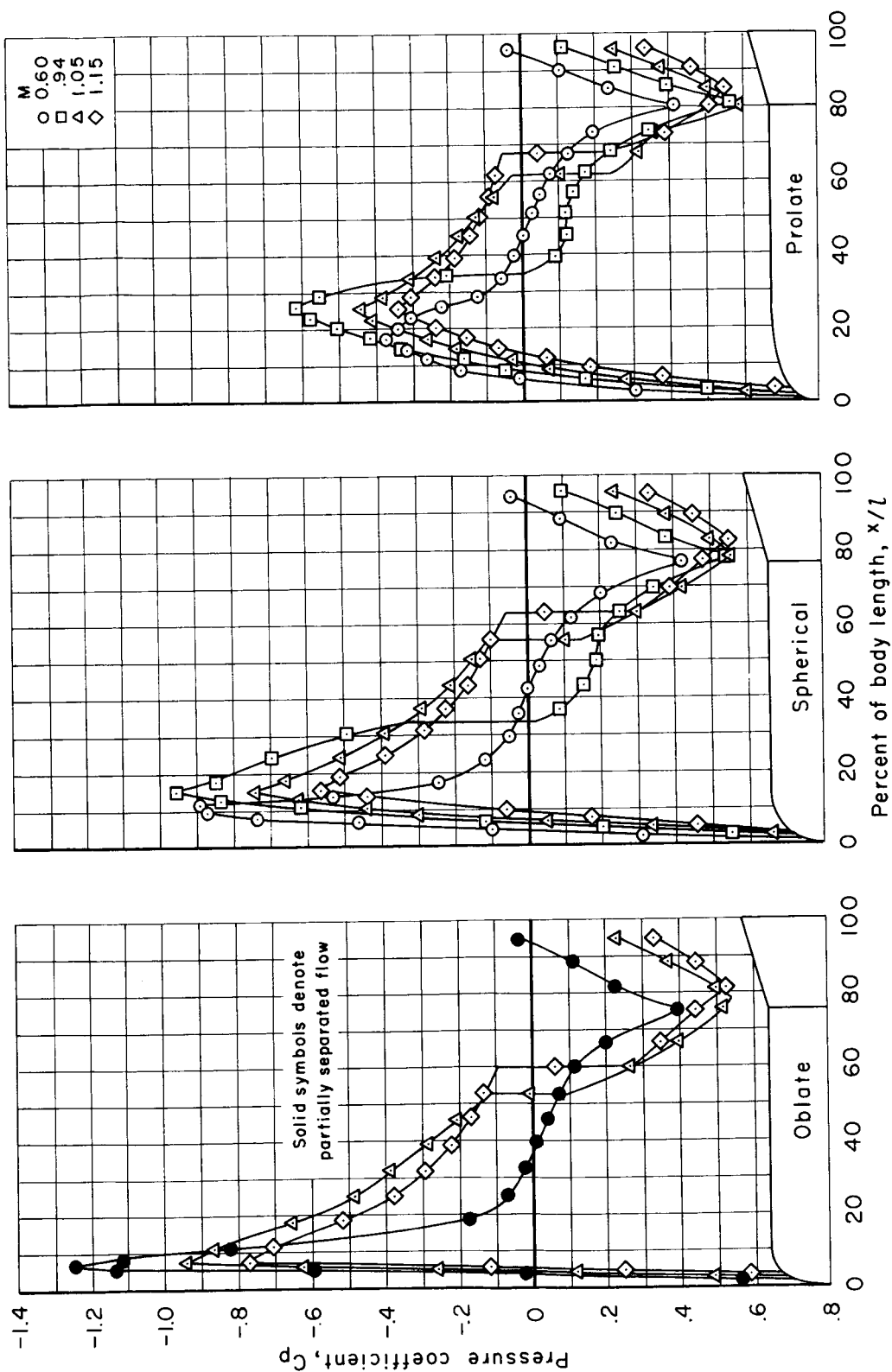


Figure 23.- Effect of Mach number on the attached-flow pressure distribution of the models with the standard flare.

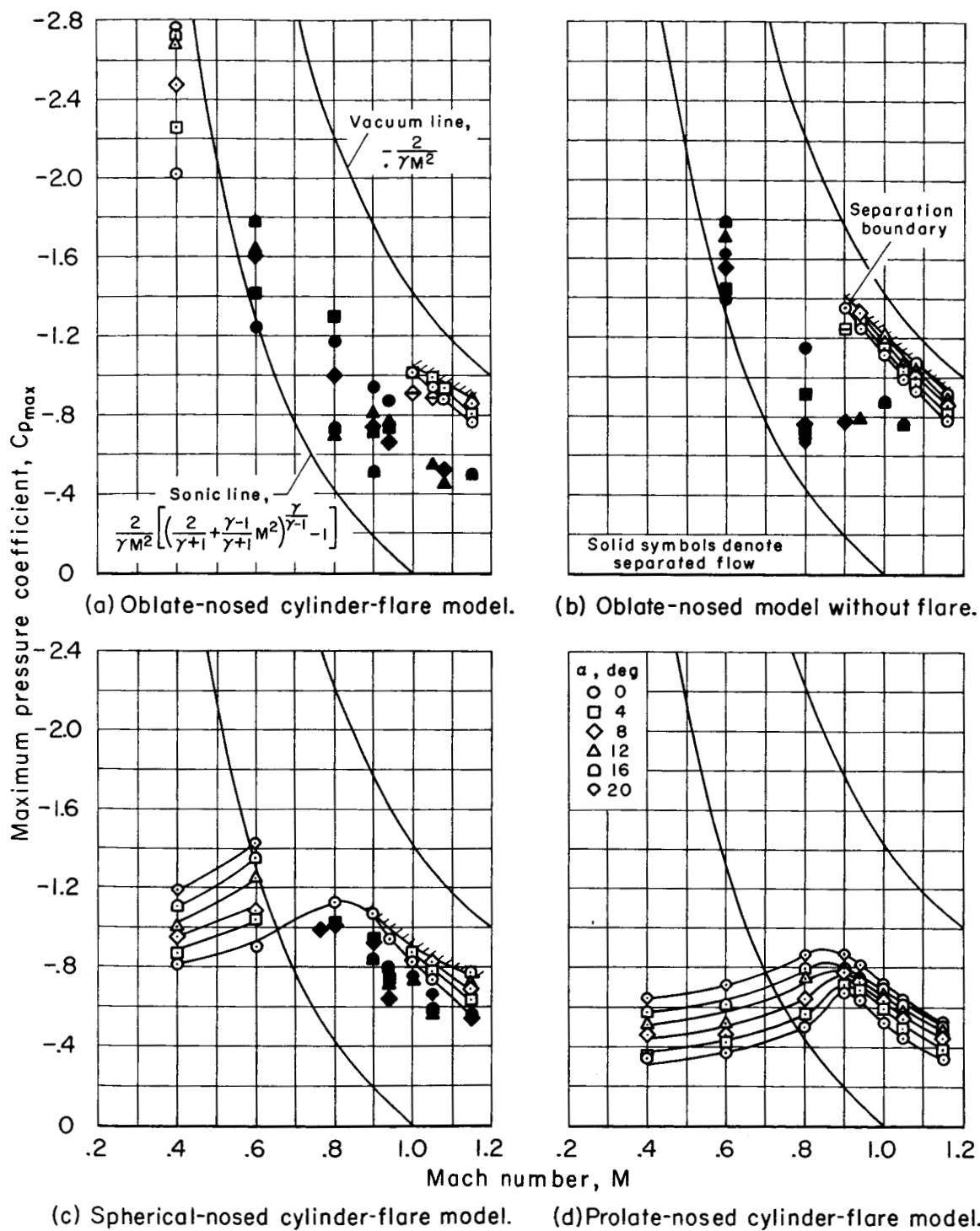


Figure 24.- Maximum negative pressure coefficient of cylinder-flare models; $\theta = 0^\circ$.

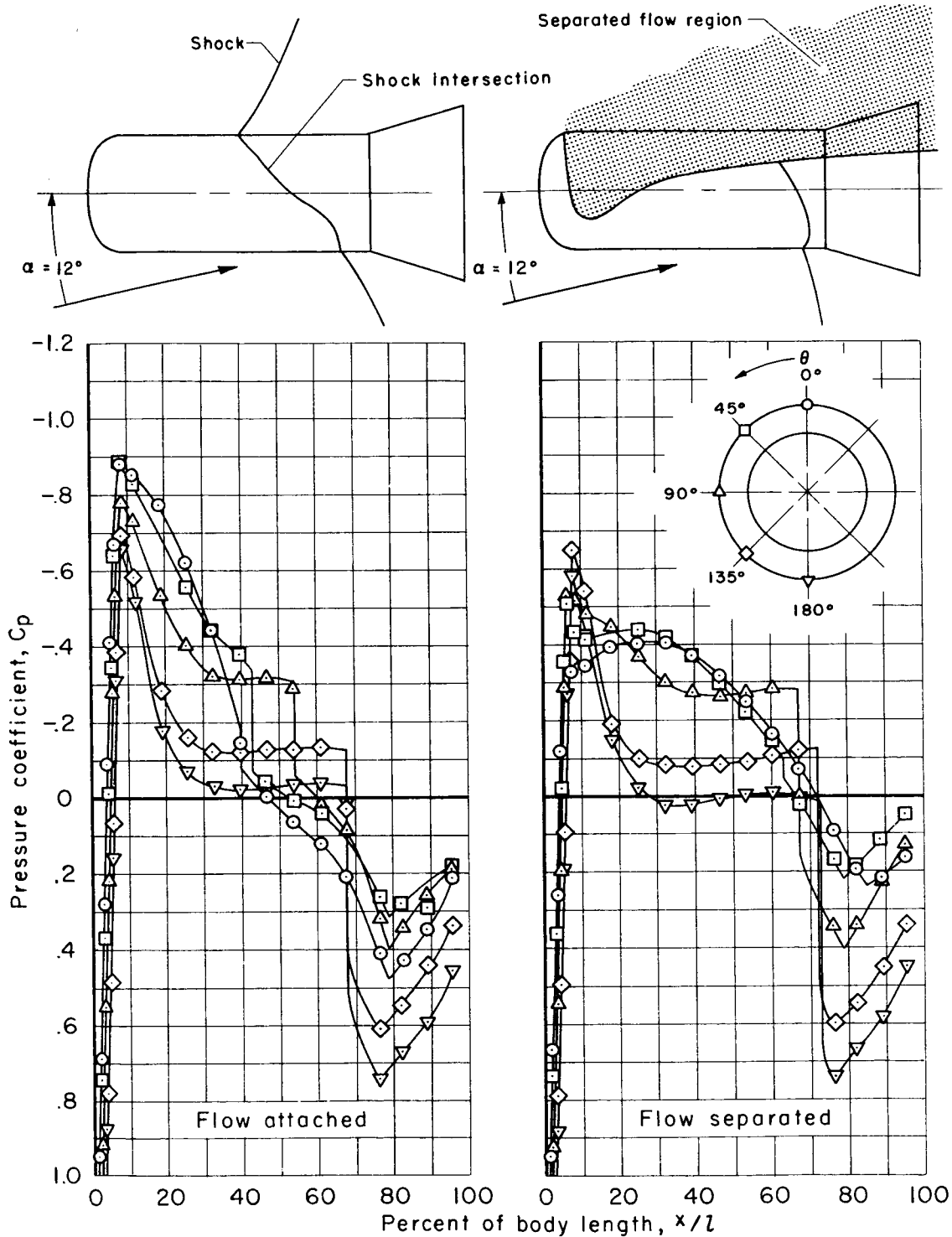


Figure 25.- Pressure distribution of stable flows at an angle of attack within the hysteresis loop, $M = 1.15$.

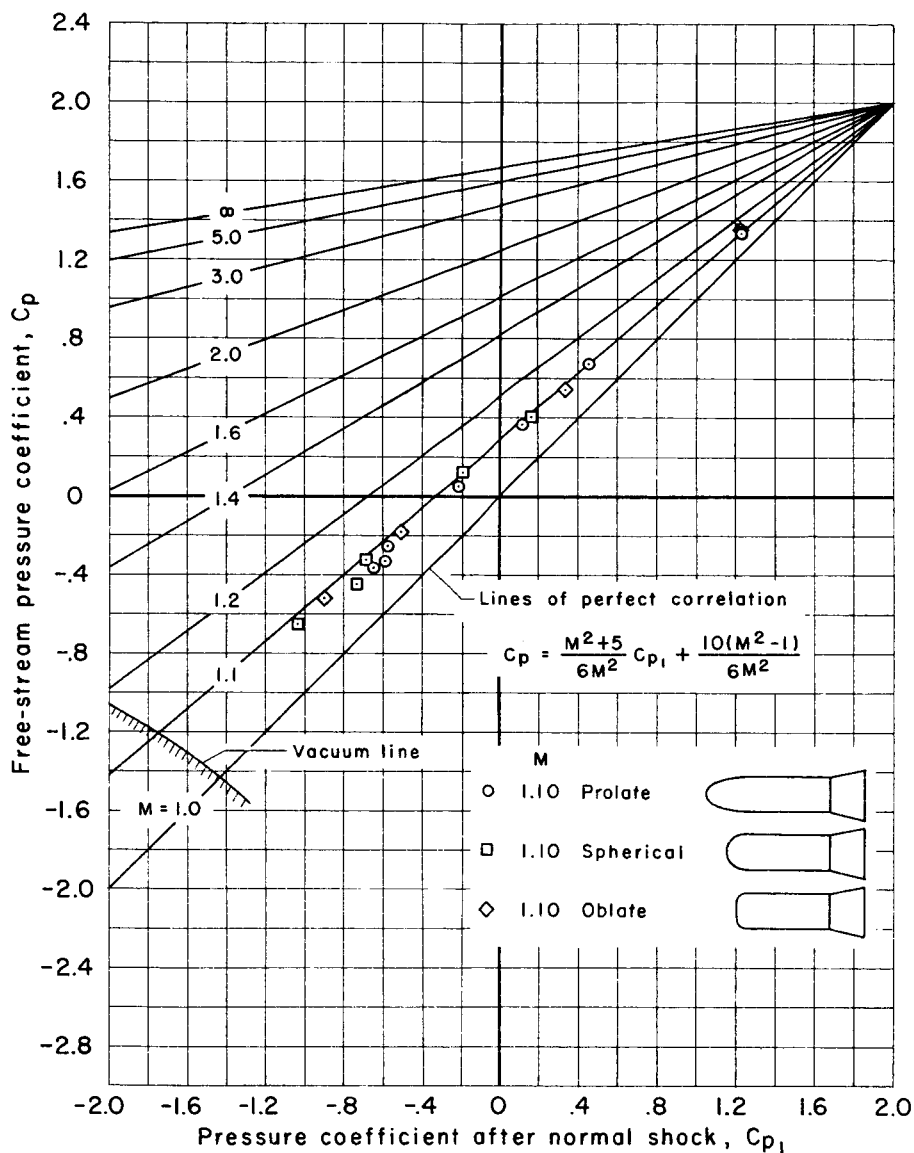


Figure 26.- Correlation of pressure coefficient of the various nose shapes at transonic Mach numbers.